ENGINEERING ACOUSTIC WAVE ON SOLID STATE QUANTUM MATERIAL

by

Boyang Jiang

A Dissertation

Submitted to the Faculty of Purdue University

In Partial Fulfillment of the Requirements for the degree of

Doctor of Philosophy

School of Electrical and Computer Engineering

West Lafayette, Indiana

May 2022

THE PURDUE UNIVERSITY GRADUATE SCHOOL
STATEMENT OF COMMITTEE APPROVAL

Dr. Sunil A. Bhave, Chair

School of Electrical and Computer Engineering

Dr. Tongcang Li

Department of Physics and Astronomy

Dr. Dana Weinstein

School of Electrical and Computer Engineering

Dr. Zubin Jacob

School of Electrical and Computer Engineering

Approved by:

Dr. Dimitrios Peroulis

ACKNOWLEDGMENTS

Thank you, Sunil, for being a resourceful supervisor. Without your full funding support and management, we would never have been able to focus on our research and get the job done. It amazes me that our collaborators are always the top researchers in their fields.

Thank you, Ben, Noah and Mert. You are the ones who helped out when I was a complete noob to MEMS after a physics undergrad. I cannot count the times we spent together both in the cleanroom and out. Your patience and understanding of MEMS have really taught me a lot over these years.

Thank you, Hao, Yanbo and Ozan. My senior labmates are the ones who have given me the most support. Each of your backgrounds gave me a completely fresh view on the problems I was solving. You also helped me a lot in adapting to life at Purdue, as a young dude who came to the US at the age of 18.

A big shoutout to all of the Birck Nanotechnology Center (BNC) staff and Nanotechnology Student Advisory Council (NSAC) board, as well as the Notre Dame Nanofabrication Facility (NDNF) staff. Running a cleanroom is never easy, but your efforts have made it much more convenient for users to learn and work on the equipment.

Thank you, Huiyao, Gary and Jonathan. Your knowledge and help on the physics side has really brought new meaning to my research. Working with the top people in the field always reminds me of how much I hope to improve.

Oh, how can I forget the awesome people I met at Skyworks during my internship. Dave, Mihir, Jiansong—the top people in MEMS filters today—you were the ones who led me into the bigger world of the MEMS industry. The short time I spent with you in Irvine helped me recover from my darkest hours during my PhD. There are so many great people who helped me in my PhD years, without whom I would never have become who I am today. I would like to express my gratitude to every one of them. I truly hope that we will cross paths again in the future.

PREFACE

The first question I got from Sunil when I started my Ph.D. was, "Are you really 18?"

"Yes," I said.

Life as a young fella is never easy. Since I was admitted to the University of Science and Technology of China (USTC) at the age of 15, I had been expected to become some sort of "genius" and solve the world's most difficult problems—while playing with fidget spinners. Yet without much of a story to tell, I got my B.Sc. degree in physics and started my journey as a PhD student at Purdue.

The move from a Chinese metropolis to a rural American town has brought so many unforgettable memories into the heart of this young man: first car, first publication, first time skydiving, first road trip from coast to coast, first internship ... and, of course, first time writing a Ph.D. thesis. As a new writer, I hope you will find something interesting when you dive into my thesis.

TABLE OF CONTENTS

LIST OF TABLES

LIST OF FIGURES

ABSTRACT

Solid state spin is a rapidly developing system for quantum sensors and computers. With the development of fabrication technology, since 2013, microelectromechanical systems (MEMS) technology began to be integrated with mechanical strain coupled to the spin system, instead of a traditional microwave antenna. Subsequently, the ability of quantum control in this system was greatly extended. In one example, strain has been demonstrated to be useful in dynamical decoupling, which increases the T_2^* of a diamond NV center.

Since the first work on strain-spin coupling in diamond, research has been greatly broadened to include SiC, graphene, transition metal dichalcogenide (TMD) monolayers and other quantum systems. Mechanical transducers, cantilevers, surface acoustic wave (SAW) resonators and bulk acoustic wave (BAW) resonators have been proposed and fabricated to induce mechanical strain. Consequently, an urgent problem to be solved is how to design the mechanical system that works best for a given spin application? That is, how do we place the maximum strain on a specific atom position in a material? Traditional MEMS figures of merit might not apply, because mechanical resonance functions in a much larger volume, whereas spin functions at the atomic level.

To solve this problem, this thesis explores different branches of MEMS technology and compares them for spin-phonon coupling applications. First, cantilever and clamped-clamped beam devices on SiC and diamond are demonstrated, according to the fabrication technique that we developed at Purdue. The SiC lateral overtone bulk acoustic wave resonator (LOBAR) with decreased anchor loss is then introduced. Using the knowledge gained in this process, I propose a wafer level phononic crystal structure that can limit the mechanical frequency on a device wafer and thus reduce the noise. Finally, because a resonator is not the only MEMS technology that can induce strain, I explore MEMS actuators with an acoustic Fresnel zone plate device based on diamond, which can focus an acoustic wave onto the spin location.

1. INTRODUCTION

1.1 MEMS Device Overview

1.1.1 MEMS Actuator and Resonator

MEMS was first developed in the 1960s, when researchers began to use integrated circuit (IC) technology to fabricate mechanical devices. The main advantage of using mechanical structure instead of electrical circuits is the low loss and the small size of the devices [1], thus enabling them to accommodate high current and withstand environmental noise. Whereas applications of MEMS involve switches, transmission lines, resonators and so on, they typically include a part called an actuator, which converts an electrical signal to the mechanical domain. Depending on the field in which a MEMS device is applied, various types of actuation force are used, including electrostatic, magnetic, piezoelectric, thermal and optical sources. Fig. 5.1 shows MEMS devices based on various actuation principles.

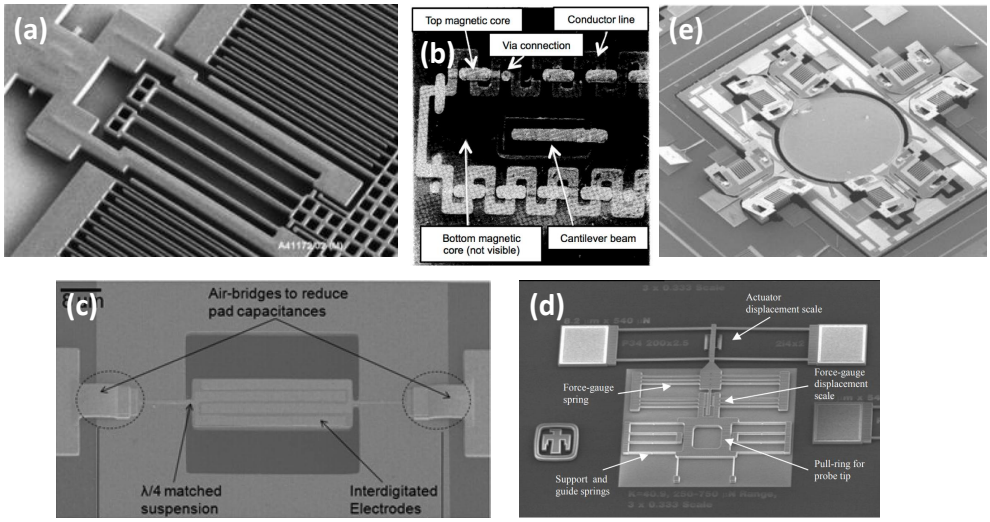

Figure 1.1. (a) An electrostatic actuator in [2]. (b) A magnetic microactuator from [3]. (c) A silicon PZT piezoelectric bulk acoustic wave resonator from [4]. (d) A thermal actuated MEMS sensor from [5]. (e) A MEMS optical sensor from [6].

After mechanical signals are induced in the system by the actuator, they are often coupled to a MEMS resonator, which is a small structure vibrating at high frequency. MEMS resonators are extremely useful in signal processing, and have been used as sensors, filters,

oscillators and other components. This thesis focuses on a resonator working at radio frequency (RF), which is from 20 kHz to 300 GHz. Resonators can be categorized into bending mode resonators, SAW resonators, BAW resonators and so on, according to the acoustic modes used. Fig. 5.2 shows examples of these resonators.

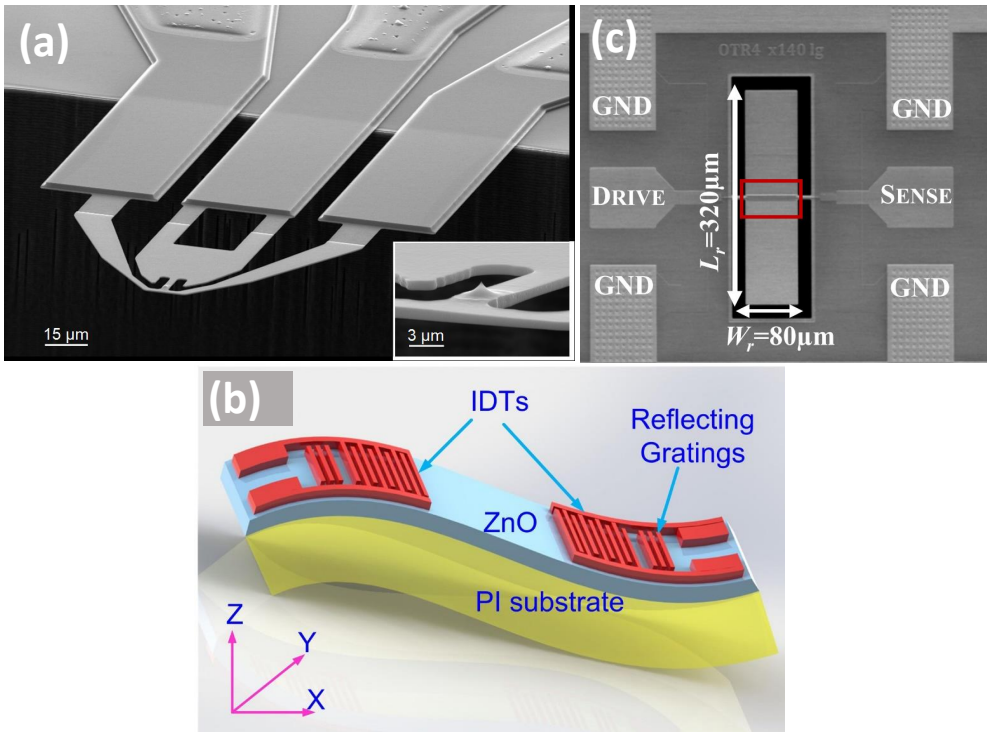

Figure 1.2. (a) The tip of a silicon cantilever device from [7]. (b) A SAW resonator from [8]. (c) A lateral overtone bulk acoustic wave resonator from [9].

According to the design of the resonator, at some frequency points, called the resonance frequencies, the loss of the energy is minimal. MEMS designers pay substantial attention to these resonance points and tune them to optimize the performance of MEMS products. To understand the resonator physically, when such resonators are driven under an external signal, the system can be treated as a forced vibration with damping in Fig. 5.3, governed by equation:

$$M\ddot{x} + C\dot{x} + Kx = F_{input} \tag{1.1}$$

Here M is the effective mass, C is the effective loss, while K is the effective stiffness of the resonator.

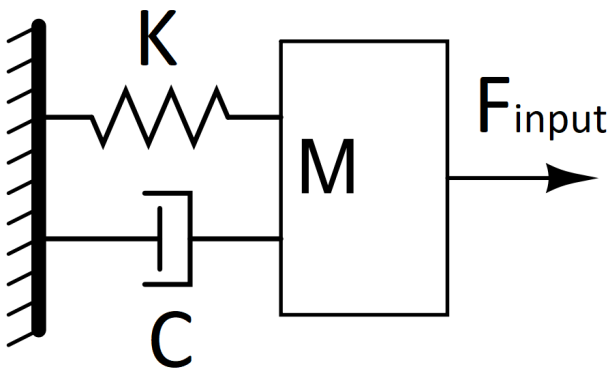

Figure 1.3. Forced damping model of a MEMS resonator.

To characterize the performance of the resonance, the quality factor (Q) is defined as:

$$Q \equiv 2\pi \cdot \frac{E_{\text{stored}}}{E_{\text{dissipated}}} \tag{1.2}$$

which is the ratio of average energy stored vs dissipation. Also, the intrinsic resonance frequency can be calculated from the driving equation, which is $\omega_0 = \sqrt{\frac{K}{M}}$. Using these 2 definition, we can write down the transfer function (the relation between the physical force and the corresponding displacement) of our resonator [10]:

$$H(s) = \frac{X(s)}{F_{input}(s)} = \frac{1}{M^2 + Cs + K} = \frac{1}{K}\left(\frac{\omega_0^2}{s^2 + \frac{\omega_0}{Q}s + \omega_0^2}\right) \tag{1.3}$$

$s = \mathrm{j}\omega$ is the complex frequency. The damped resonance frequency can also be solved as [11]:

$$\omega_{\mathrm{r}} = \omega_0\sqrt{1 - \frac{1}{2Q^2}} \tag{1.4}$$

Experimentally, Q is often measured by 3dB bandwidth from a frequency sweep across the spectrum:

$$Q = \frac{\omega_0}{2}\frac{\mathrm{dH}(\omega)}{\mathrm{d}\omega} = \frac{f_0}{\Delta f_{-3dB}} \tag{1.5}$$

As it is seen in Fig. 5.4, the higher Q is , the narrower the 3dB bandwidth will be.

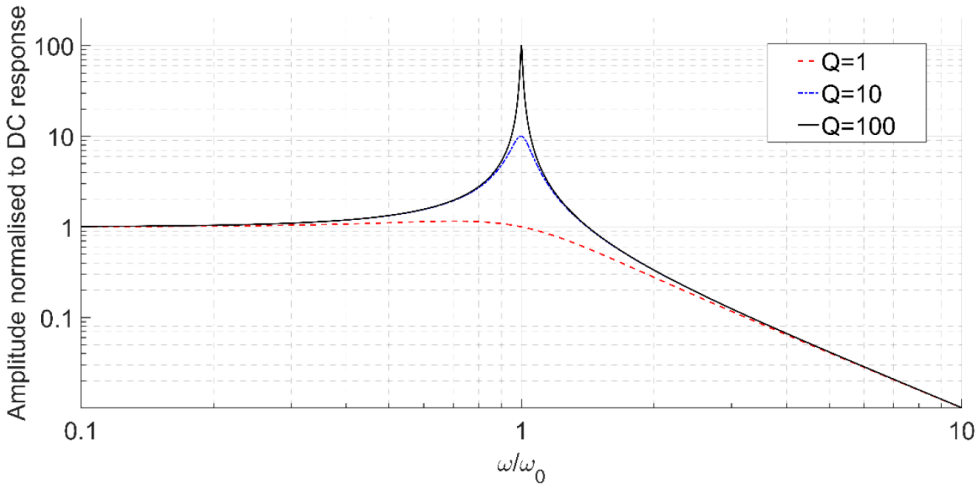

Figure 1.4. Frequency response of an ideal resonant system. Image from [10].

This work focuses on a piezoelectrically driven MEMS resonator based on silicon carbide and diamond substrate. As introduced in the following sections, the main goal of building the devices is to induce high stress in the mechanical body. To date, piezoelectric actuation has shown the highest electrical-mechanical energy transfer efficiency among all actuation principles. In addition, recent technologic developments in SiC and diamond micro-machining have enabled fabrication of devices with designs that were previously limited to only silicon substrate.

1.1.2 Piezoelectric Resonator

Piezoelectricity is a phenomenon in which electric charge can be induced by application of mechanical stress in certain materials. Because this process is reversible, an electrical signal can be used to generate mechanical stress, called the inverse piezoelectric effect. Typical piezoelectric materials include certain crystals, ceramics and organic materials. The commonly used crystal piezoelectric materials in MEMS are Lead Zirconate Titanate (PZT), Aluminum Nitride (AlN), Zinc Oxide (ZnO) and Lithium Niobate ($LiNbO_3$). The effect can be expressed as the following [12]:

$$\begin{aligned} T &= ES - \mathrm{e}\mathcal{E} \\ D &= \epsilon\mathcal{E} + \mathrm{e}S \end{aligned} \tag{1.6}$$

Here, T is the local stress, E is Young's modulus of the material, S is the local strain, E is the material's permittivity, e is the material's piezoelectric coefficient, E is the local electric field, and D is the electric displacement. These symbols are summarized in Table 2.1.

Table 1.1. Summary of piezoelectric equation symbols

Symbol	Meaning	Unit
T	Stress	N/m^2
E	Young's modulus	Pa
S	Strain	1
ϵ	Permittivity	F/m
e	Piezoelectric Coefficient	C/m^2
$\mathcal{E}$	Electric Field	V/m
D	Electric Displacement	C/m^2

While the parameters in the equations are determined by the material, to characterize the piezo-to-electric energy conversion strength in a real resonator, the electromechanical coupling coefficient, k_t, is defined as:

$$k_t^2 = \frac{E_{converted}}{E_{input}} \tag{1.7}$$

which is the ratio of the converted mechanical/electric energy vs the total input electric/mechanical energy, depending on whether we are using the inverse or original piezoelectricity. This coefficient depends on the resonant mode, the piezoelectric and the substrate material, electric circuit design and others. MEMS designers usually try to maximize this factor in design, in order to induce a large mechanical strain while minimizing the power consumption of the device.

By using the piezoelectric material in a resonator, we can use an electric signal to cause the a mechanical device to resonate, making a piezoelectric resonator. Such devices are commonly used in civilian and defense fields. For example, RF filters based on piezoelectric resonators are used in every mobile phone, and the demand will only be higher based on the new requirement from 5G network [13]. In particular, the Butterworth Van-Dyke (BVD) Model was developed to use to describe the frequency response of such resonators. Shown in Fig. 5.5

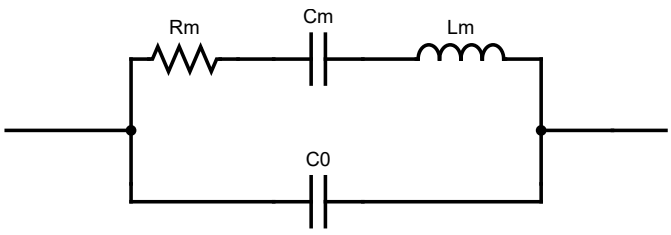

Figure 1.5. BVD model for a piezoelectric resonator.

The parameters:

$$
\begin{aligned}
C_0 &= \frac{\epsilon\epsilon_r A}{t} \\
C_m &= C_0 \frac{8k_t^2}{\pi^2} \\
L_m &= \frac{1}{\omega_s^2 C_m} \\
R_m &= \frac{\pi^2 \eta}{8k_t^2 \rho v_{aw}^2 C_0} \\
Q &= \frac{\omega_s L_m}{R_m}
\end{aligned}
\tag{1.8}
$$

C_0 is the static capacitance, while C_m, L_m and R_m are the motion components. ω_s is the resonant angular frequency, η is the acoustic viscosity, ρ is the density, v_{aw} is the acoustic velocity. The effective quality factor can be calculated from the above equation. Note that this Q is the equivalent circuit Q. Since the BVD model is only an approximation of the real resonator, the Q might not be exactly the same as the measured Q. Nonetheless, we can use the BVD model as a guidance for designing high performance piezoelectric resonators.

1.2 Solid State Spin Platform

1.2.1 Silicon Carbide and Defect Centers

Silicon carbide (SiC) is a semiconductor material composed of Silicon and Carbon atoms. While different phases of SiC exist, the most commercially available SiC polytypes are 3C, 4H and 6H. They are typically grown using chemical vapor deposition (CVD) based on SiH_4, H_2 plus N_2 [14]. 3C-SiC is a diamond like cubic crystal, while 4H and 6H are of hexagonal lattices, shown in Fig. 5.6

In the SiC material, owing to natural formation or ion implantation, atomic defects can form in the crystal lattice where the original Si or C atoms are missing. Researchers have extensively studied two of the vacancies - silicon vacancy (V_{Si}) and divacancy ($V_{Si}V_C$ due to their spintronic properties. These vacancies have been demonstrated to provide a promising platform for quantum sensing, computation and information [15]. Because silicon vacancy has only been recently demonstrated and studied in quantum application, we will start by introducing the divacancies in 4H-SiC in Fig. 5.9.

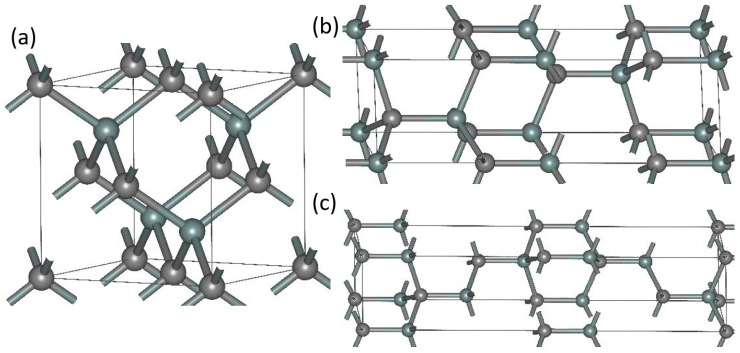

Figure 1.6. Crystal structure of (a) 3C (b) 4H (c) 6H SiC.

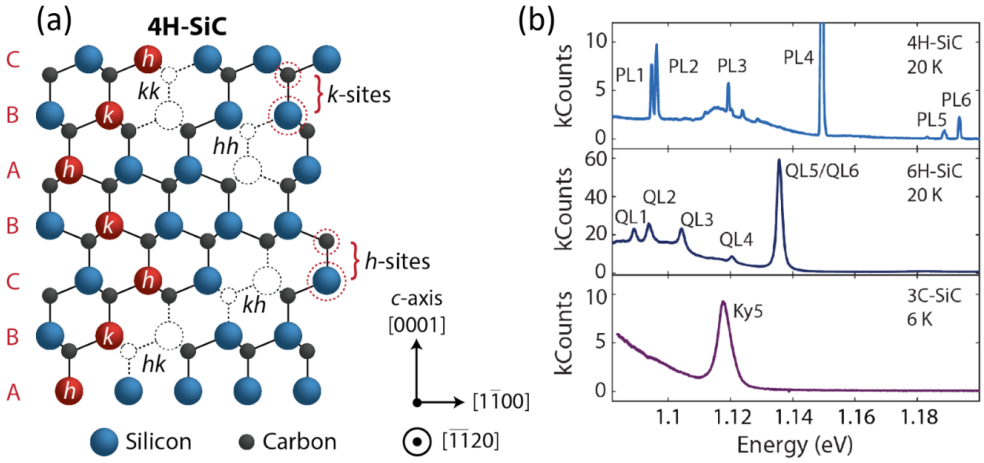

Figure 1.7. (a) 4H-SiC with 4 different types of divacancies. (b) Photoluminescense (PL) spectrum of 4H, 6H and 3C-SiC. The PL1-4 correspond to hh, kk, hk and kh divacancy setup. The figure is taken from [16].

From the electronic charge of the defects, the divacancy can be treated as a spin=1 triplet system. The energy level is shown in Fig. 3.9 (a). In this level structure, a near infrared laser can be used to excite the spin. During the relaxation back to ground state, the spin can undergo either a radiative process, wherein the emitted photon can be detected in experiment, or a non-radiative process. Because the $|\pm 1\rangle$ and $|0\rangle$ spin states' photon emission rates are different, the spin state can be determined according to the photoluminescence (PL) count.

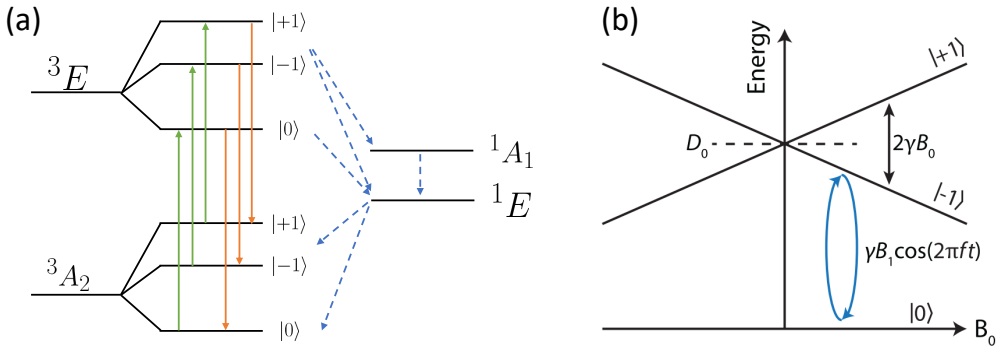

Figure 1.8. (a) Energy level of the divacancy. Sold lines and dash lines represent radiative and non-radiative process accordingly. (b) Principle of ODMR from [16].

The Hamiltonian of the divacancy can be expressed as [17]:

$$\begin{aligned} H &= hD\sigma_z^2 + g\mu_B \sigma \cdot \mathbf{B} - E_x\left(\sigma_x^2 - \sigma_y^2\right) + E_y\left(\sigma_x\sigma_y + \sigma_y\sigma_x\right) \\ D &= D^0 + d_{\parallel}F_z + \mathrm{e}_{\parallel}\varepsilon_z \\ E_{x,y} &= E^0_{x,y} + d_{\perp}F_{x,y} + \mathrm{e}_{\perp}\varepsilon_{x,y} \end{aligned} \tag{1.9}$$

Here the defect axis is set to be on z direction. h is the Planck constant, g=2 for electrons, δ is the vector of Pauli matrices when spin=1, μ_B is the Bohr magneton, $\mathbf{B}$ is the magnetic field. D, E_x, E_y are the zero-field splitting factor. In their expressions, $d_{\parallel}, d_{\perp}$ are Stark coefficient under an electric field F, while $\mathrm{e}_{\parallel}, \mathrm{e}_{\perp}$ are the strain coupling coefficient when applying a mechanical strain ε.

Based on the Hamiltonian, one common experiment conducted on the spin is optically detected magnetic resonance (ODMR), shown in Fig. 3.9 (b). When placed near a static

magnetic field B_0, the $|\pm 1\rangle$ degeneracy is lifted by Zeeman splitting $h\nu = g\mu_B B_0$. Using this splitting, we can sweep the microwave field with a external field B_1. By finding the resonant frequency f, we will be able to back-calculate the strength of B_0, achieving the detection of the unknown field.

While the ODMR technology is already well-studied on SiC divacancy as well as other solid state spins, researchers recently have been extending similar concepts to the mechanical field [18, 19]. The strain-spin coupling can be used both ways: a strain-involved resonance can be used for detecting small strain field previously difficult to observe [20], and we can use the introduce a strain field manually to manipulate the spin state [21]. In particular, the latter application has seen use in dynamical decoupling of the strain field [22], which increased the electron spins' resistance to dephasing due to the influence of neighboring environment noise. Such application will allow the defects to become a more rigid quantum platform.

To induce strain in SiC, piezoelectric materials become the best option, for the low power consumption, and the fact that they can be integrated onto spintronic material using semiconductor fabrication techniques. I work on designing, fabricating and testing piezoelectric resonators based on these platforms and inducing large strain waves in the device for strong phonon-spin coupling. Also, SiC has shown great potential in MEMS application, as it has extremely low loss [23], high mechanical hardness and elasticity at high temperatures, a high thermal conductivity and is chemically inert [24] compared with traditional Silicon based resonator. This makes it a potential candidate for the next generation commercial MEMS material. By working on the system, we may combine the advantages of the two. In our case, 4H-SiC wafers are bought from Cree Inc., and then sent to OEM Group for deposition of Aluminum Nitride and the electrode metal.

1.2.2 Diamond and NV Center

Besides SiC, the Nitrogen-Vacancy (NV) center in diamond is formed by a nitrogen atom replacing a carbon while a neighbor location is vacant, in Fig. 3.10 (a). When the system is negative charged, the defect energy level of NV^- (commonly written as NV) shows a spin=1 triple similar to that of the divacancy in SiC (Fig. 3.10 (b)). Because of this, the previous

discussion on SiC divacancy also applies to diamond NV, with the coupling coefficient in Hamiltonian different by material.

While due to cost, diamonds are usually provided in mm scale, making it much more difficult on fabrication compared with wafer level SiC (Fig. 3.11), certain advantages exist in the system. First and the most importantly, diamond NV's PL has strong signal under room temperature, while the divacancy has to be cooled down to cryogenic condition for the PL to be observed. This makes diamond NV an ideal sensor for temperature sensitive and non invasive applications like biological sensing. Also, the simpler crystal structure of NV eliminates the need to distinguish 4 different PL peaks of divacancies, which can be difficult to control during the ion implantation process. Thus, various efforts has been made to accommodate diamond with piezoelectric material [25, 26]. In our collaboration with Prof. Greg Fuchs group at Cornell University, we are working on in-house CVD growth of ZnO and AlN on diamond, and making piezoelectric resonators based on that.

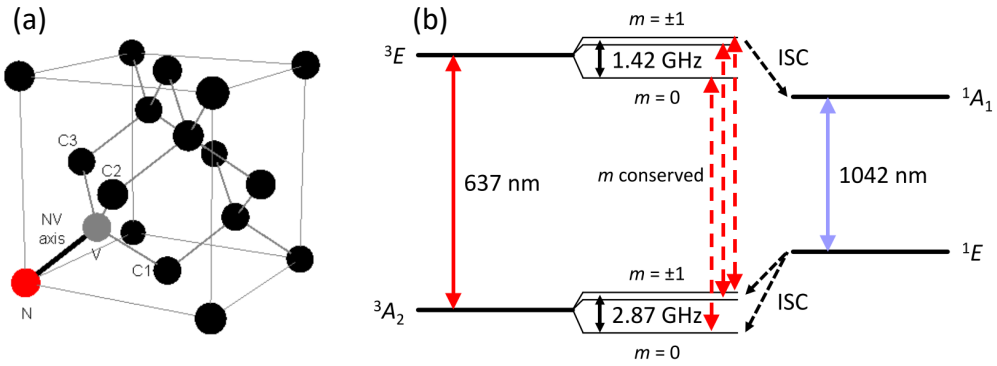

Figure 1.9. (a) Crystal structure of an NV center in diamond lattice. (b) NV energy level. Figure from [27].

1.2.3 Review of Resonances in a Spin System

In order to fully understand the Hamiltonian and its effect on our spin system, it is necessary to review the magnetic and mechanical resonance in a spin system.

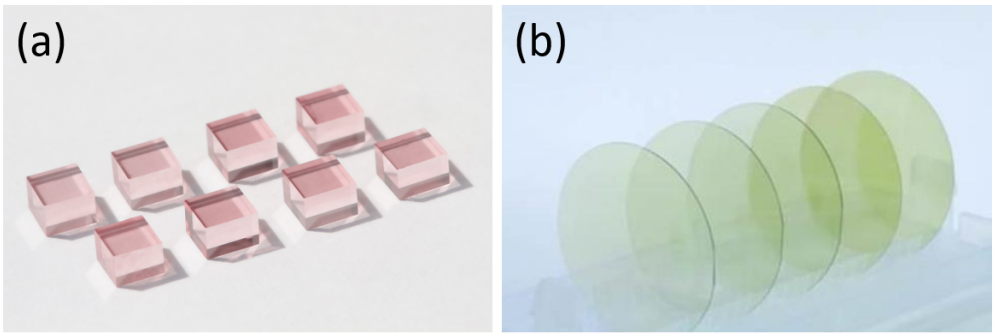

Figure 1.10. (a) Commercial diamond slabs are at mm scale. (b) SiC wafers are widely available at various radius, allowing easy implementation of Si wafer fabrication techniques.

Two-state System

For a two state quantum system, we can use the Dirac notation to write the superposition state as:

$$|\psi\rangle = \cos(\theta/2)\,|\downarrow\rangle + \sin(\theta/2)\mathrm{e}^{\mathrm{i}\phi}\,|\uparrow\rangle \tag{1.10}$$

Here θ and ϕ are the angles in a Bloch sphere shown in Fig. 3.8.

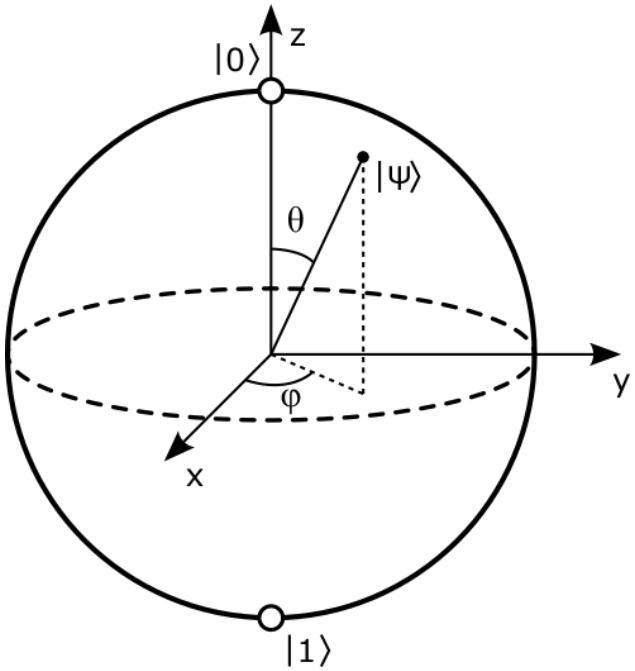

Figure 1.11. Bloch sphere. Figure from [28].

Also, the conventional Pauli matrices for 2 energy levels are:

$$\mathbf{I} = \begin{pmatrix} 1 & 0 \\ 0 & 1 \end{pmatrix}; S_x = \frac{\hbar}{2}\begin{pmatrix} 0 & 1 \\ 1 & 0 \end{pmatrix}; S_y = \frac{\hbar}{2}\begin{pmatrix} 0 & -\mathrm{i} \\ \mathrm{i} & 0 \end{pmatrix}; S_z = \frac{\hbar}{2}\begin{pmatrix} 1 & 0 \\ 0 & -1 \end{pmatrix} \tag{1.11}$$

Now for the magnetic resonance, we have:

$$H = \hbar g \mu_B B \cdot S \tag{1.12}$$

where B is the magnetic field, and $S = \{S_x, S_y, S_z\}$ is the Pauli matrices. If we apply first a static field along z axis: $H_0 = \gamma B_0 S_z$ and apply the propagator $U = \mathrm{e}^{-\mathrm{i}\gamma B_0 S_z/t}$ to the state, with $\omega_0 = \gamma B_0$, we can have:

$$U|\psi\rangle = c_\downarrow \mathrm{e}^{\mathrm{i}\omega_0 t/2}|\downarrow\rangle + c_\uparrow \mathrm{e}^{-\mathrm{i}\omega_0 t/2}|\uparrow\rangle \tag{1.13}$$

This is the so-called spin precession, and ω_0 is the Larmor Frequency. It can be understood by on the Bloch sphere the spin is rotation around z-axis at the frequency.

Now, we apply a time-dependent field $B_1 \cos(\omega t + \varphi)\hat{x}$ along the x-y plane for coherent control of the states. Let the sum Hamiltonian $H_{total} = H_0 + H_1$:

$$H_{\mathrm{lab}} = \hbar \begin{pmatrix} \omega_0/2 & \gamma B_1 \cos(\omega t + \varphi) \\ \gamma B_1 \cos(\omega t + \varphi) & -\omega_0/2 \end{pmatrix} \tag{1.14}$$

To remove the time varying term in it, we need to change our observation frame. Let $P = \mathrm{e}^{-\mathrm{i}\omega t H_0/\hbar}$, and the resulting state is:

$$P^\dagger \mathrm{e}^{-\mathrm{i}H_0 t/\hbar}\,|\psi\rangle = |\psi(t)\rangle_{\mathrm{rf}} = c_\downarrow \mathrm{e}^{+\mathrm{i}(\omega_0-\omega)t/2}\,|\downarrow\rangle + c_\uparrow \mathrm{e}^{-\mathrm{i}(\omega_0-\omega)t/2}\,|\uparrow\rangle \tag{1.15}$$

Note that the phase is not time dependent when $\omega = \omega_0$, which means we are now in a reference frame rotation around z axis at frequency ω_0. 'rf' means 'rotation frame'. For the Hamiltonian, we can write the Schrödinger equation:

$$\begin{aligned} \mathrm{i}\hbar \frac{\partial \left(PP^\dagger\,|\psi(t)\rangle\right)}{\partial t} &= P\left(P^\dagger H P\right)\left(P^\dagger\,|\psi(t)\rangle\right) \\ \mathrm{i}\hbar \frac{\partial\,|\psi(t)\rangle_{\mathrm{rf}}}{\partial t} &= \left(P^\dagger H P - \mathrm{i}\hbar P^\dagger \frac{\partial P}{\partial t}\right)|\psi(t)\rangle_{\mathrm{rf}} \end{aligned} \tag{1.16}$$

so in this frame, $H_{\mathrm{rf}} = P^\dagger H P - \mathrm{i}\hbar P^\dagger \frac{\partial P}{\partial t}$, and:

$$H_{\mathrm{rf}} = \hbar \begin{pmatrix} (\omega_0 - \omega)/2 & \frac{\gamma B_1}{2}\mathrm{e}^{-\mathrm{i}\varphi}\left(1 + \mathrm{e}^{2\mathrm{i}(\varphi+2\omega t)}\right) \\ \frac{\gamma B_1}{2}\mathrm{e}^{\mathrm{i}\varphi}\left(1 + \mathrm{e}^{-2\mathrm{i}(\varphi+2\omega t)}\right) & -(\omega_0 - \omega)/2 \end{pmatrix} \tag{1.17}$$

When $B_1 \ll B_0$, we can use the so-called rotational wave approximation and ignore the 2ω terms, since it is rotating much faster than the driving frequency and get time-averaged to 0. Define $\Delta = \omega_0 - \omega$ as the frequency detuning, and $\Omega = \Gamma B_1$ as the magnetic driving field magnitude, we can rewrite:

$$H_{\mathrm{rf}} \approx \hbar \begin{pmatrix} \Delta/2 & \frac{\Omega}{2}\mathrm{e}^{-\mathrm{i}\varphi} \\ \frac{\Omega}{2}\mathrm{e}^{\mathrm{i}\varphi} & -\Delta/2 \end{pmatrix} \tag{1.18}$$

this equation serves as the principle for the ODMR experiment mentioned in the previous section.

Three-state System

Similar to the 2 state system, we now can extend our treatment to the 3 states, which is the case for NV or divacancies when the $|\pm 1\rangle$ degeneracy is broken, and the basis is now $\{|+1\rangle, |0\rangle, |-1\rangle$. The Pauli matrices are now:

$$\S_x = \frac{1}{\sqrt{2}} \begin{pmatrix} 0 & 1 & 0 \\ 1 & 0 & 1 \\ 0 & 1 & 0 \end{pmatrix}; \S_y = \frac{1}{\sqrt{2}} \begin{pmatrix} 0 & -\mathrm{i} & 0 \\ \mathrm{i} & 0 & -\mathrm{i} \\ 0 & \mathrm{i} & 0 \end{pmatrix}; \S_z = \frac{1}{\sqrt{2}} \begin{pmatrix} 1 & 0 & 0 \\ 0 & 0 & 0 \\ 0 & 0 & -1 \end{pmatrix} \tag{1.19}$$

the Hamiltonian can be written in as:

$$\begin{aligned} H &= H_{\mathrm{Zeeman}} + H_{SS} \\ &= \gamma \mathbf{B} \cdot \mathbf{S} + \mathbf{S} \cdot \mathbf{D} \cdot \mathbf{S} \end{aligned} \tag{1.20}$$

$\mathbf{S} = \{S_x, S_y, S_z\}$, $\mathbf{D}$ is the zero field splitting. When there is no external field like electric or strain affecting, the $H_{SS} = \hbar D_0 S_z^2$, when we choose the divacancy axis as the z axis. The

strain field interferes with the system through this term. Under a fixed-frequency strain field driving, using the rotation frame, we can write the H_{SS} as:

$$H_{SS}/h = \frac{1}{2}\begin{pmatrix} \Delta D_0' & \Omega_1 & \Omega_2 \\ \Omega_1^\dagger & -2\Delta D_0' & \Omega_3 \\ \Omega_2^\dagger & \Omega_3^\dagger & \Delta D_0' \end{pmatrix} \tag{1.21}$$

shown in Fig. 3.7, here $\Omega_{1,3}$ are the single spin transition for $\Delta m_s = \pm 1$, while the interesting part is Ω_2, where $\Delta m_s = \pm 2$, effectively $|+1\rangle \Longleftrightarrow |-1\rangle$. This transition is forbidden by selection rules in Zeeman effect. Detailed derivation is not focused in this thesis, which can be found in [16]. Recent researches have proven the possibility of both transitions, and the strain-spin coupling coefficients have been measured [29, 18].

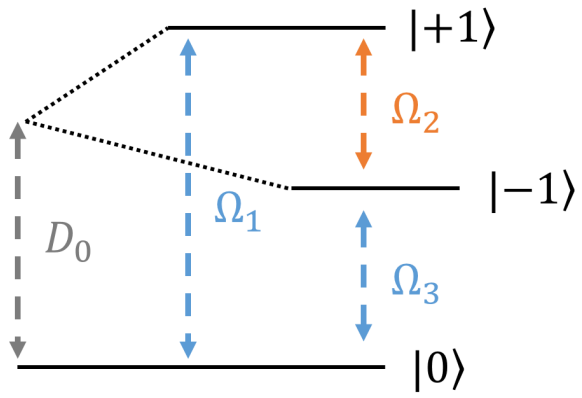

Figure 1.12. Three state oscillation under mechanical driving.

1.2.4 Comparison Between Acoustic and Microwave Control of Solid State Spins

In recent years, acoustic quantum control has shown capabilities similar conventional microwave control. Here, I list recent works in this area and compare their achievements. The main figures of merit are the Rabi frequency at certain power output and the spin coherence time T_2^* (or so-called inhomogeneous spin-dephasing time). Because of insufficient research in SiC, we investigate diamond works for example. Table 1.2, 1.3, 1.4 refer to publications on spin control in SiV in diamond, ^{13}C nuclear spin in diamond (readout through SiV) and

NV in diamond. The SAW devices for SiV exhibit Q of 1000-10000, and the HBAR for NVs are of Q around 500. Although the numbers cannot be compared exactly, since the measurement conditions are different for each work, it is clear that mechanical control is of the same speed and power consumption as the traditional microwave control. In the SiV case, acoustic control even has an edge in power consumption, due to the energy conservation from an acoustic resonator. Interestingly, in [30], the authors use specifically designed microwave antennae to focus more emission onto the sample area, thus enhancing the Rabi frequency under the same driving power. In the future hybrid control quantum system, the acoustic resonator can be combined with microwave antenna in design optimization, to bring the figure of merit even higher.

Table 1.2. Quantum Control of SiV in Diamond

Method	Acoustic (SAW) [31]	Microwave[32]
Spin Coherence Time (T_2^*)	33 ns (5.8K)	115 ns (3.6K)
Power Consumption vs Rabi frequency	25 MHz at 1 mW	10 MHz at 1 mW

Table 1.3. Quantum Control of ^{13}C Nuclear Spin in Diamond

Method	Acoustic (SAW) [33]	Microwave [34]
Spin Coherence Time (T_2^*)	2 ms (200 mK)	6.8 ms (2 K)
Power Consumption vs Rabi frequency	9.8 kHz (0.63 mW)	15 kHz (0.15 V)

Table 1.4. Quantum Control of NV in Diamond

Method	Acoustic (HBAR) [35]	Microwave [30]
Spin Coherence Time (T2*)	∼1 us (RT)	∼1 us (RT)
Power Consumption vs Rabi frequency	3.8 MHz (33 dBm)	22 MHz (33 dBm)

1.2.5 Loss Mechanism in Piezoelectric-Spin Resonators

To build an optimal piezoelectric resonator for spin application, the energy loss mechanism must be understood. Fig. 3.12 shows the hybrid system with the piezoelectric material, mechanical resonator and the spin.

First, to induce resonance in the system, an electric signal must be applied to the piezoelectric material. This step involves the loss from the electrode material due to heating and damping. A lightweight yet low resistance material is needed. In addition, the electric circuit on top must be designed such that the path is not too thin to cause high resistance yet not too large to introduce a large static capacitance C_0 in the BVD model.

Second, the electromechanical coupling coefficient kt determines how much energy can be transferred from the piezoelectric material into the substrate SiC/diamond. This process involves the material and resonance mode selection [36, 37]. In the experiments herein, AlN is used for exploring the resonance modes in various resonator designs because of its outstanding performance up to high frequencies (GHz).

Third, the quality factor can indicate how much energy can be preserved in the resonator after induction. Because the resonator cannot be completely isolated from its environment, the impact of the resonator must be minimized. In this case, SiC and diamond have much higher intrinsic Q than conventional silicon as a substrate material, but they remain prone to loss from the surface, anchor, air and so on. To solve this challenge, specifically shaped tethers, phononic crystals and substrate structures have been developed.

Finally, we are also interested in the phonon-spin interaction at the atomic level. Although the resonator Q and k_t can indicate the maximal energy that the system contains, the mechanical wave is distributed across the entire device body. Meanwhile, in terms of quantum control, single spin measurements are much more accurate and thus more desirable than ensembles, because only a small volume in the resonator is required. In addition, the spin's location affects its stability and sensitivity, because of the influence of coupling of the neighboring environmental spins. Thus, achieving precise control of the generated strain and reaching a local maximum in terms of strain-spin coupling are crucial. For this purpose, we must explore the resonance mode volume and spin direction associated with the strain.

Whereas a traditional MEMS application typically requires only one or two figures of merit, in our spin coupling design, all these parameters must be considered. The work in this thesis was aimed at implementing designs to address these issues from various perspectives.

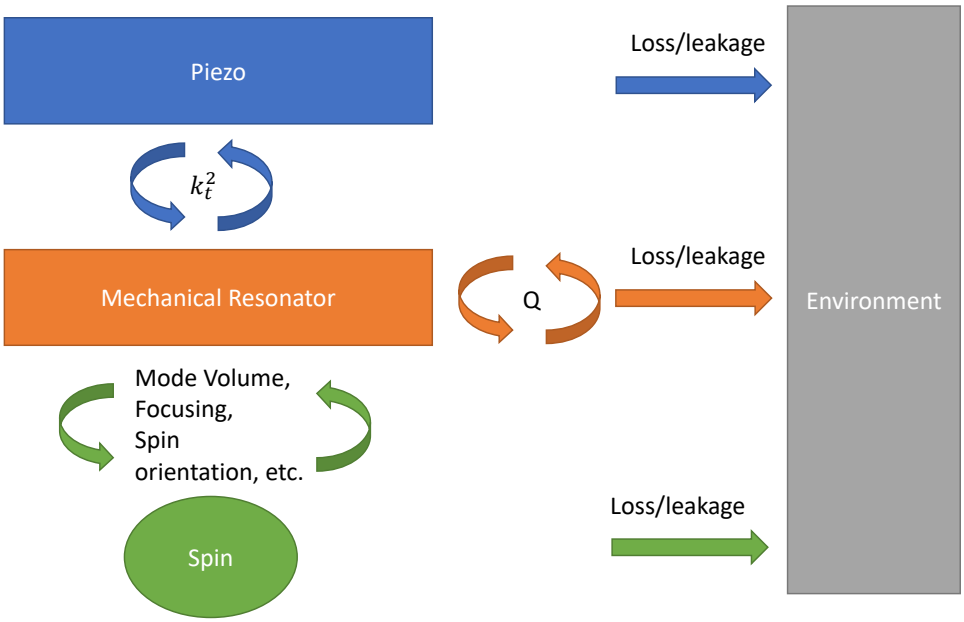

Figure 1.13. Energy pathway from piezoelectric material to solid state spins. Multiple loss mechanisms are involved in this system.

1.3 Thesis Outline

Chapter 1 of this thesis provides the background of my research and an introduction to the platform that we are working on. Chapter 2 describes the cantilever and clamped-clamped beam devices on SiC and diamond. Chapter 3 focuses on the lateral overtone bulk acoustic wave resonators made on AlN-SiC system. Chapter 4 introduces the spin-strain coupling measurement based on our SiC LOBAR platform. Chapter 5 demonstrates using Fresnel acoustics in diamond/SiC Zone Plate resonator. The appendices include the SiC fabrication techniques and the python codes in my Ph.D. work.

2. SIC CANTILEVERS FOR GENERATING UNIAXIAL STRESS

2.1 Introduction

Single crystal Silicon Carbide, especially the 4H polytype, has been a leading material to build ultra-high-Q MEMS resonators [38, 9, 39]. Simultaneously 4H Carbide is touted as a wafer-scale manufacturable "quantum material" due to its large coherence divacancies (structural defects in the crystal that act as isolated spins) [40]. Previously high overtone bulk acoustic resonators (HBAR) [39] and surface acoustic wave devices (SAW) [41] have been fabricated on 4H-SiC, where the later was used to generate $\Delta m_s = \pm 2$ spin transition on the divacancies acoustically, which is forbidden using magnetic field.

However, there is a significant impedance (and size) mismatch between an acoustic phonon mode and a divacancy defect. This inefficiency is overcome by driving the SAW resonator at high RF drive power and achieving large force coupling between the acoustic and spin domains [41]. In order to measure the back-action effect of spin-flips on mechanical vibration modes, we need low-mass, soft resonators which can generate high uniaxial in-plane mechanical stress. A Z-direction bending mode achieves the necessary high X-axis stress on the top surface of the resonator base.

Recently membranes [42], perforated disks [43] and solid disks [44] have been demonstrated using DRIE of 4H silicon carbide. The center-anchored solid disks have outstanding $Q > 10^6$, but the back-side-only etched membranes have low Q (<500). The membrane Q did not improve when cooled to 10K, proving that having an anchor along the entire diaphragm perimeter was the dominant source of energy loss. Therefore, we adapted the dual-side etching technique pioneered in Silicon micromirrors [45, 46] to define front-side patterned and lithographically defined tethers and achieve high-Q bending mode 4H silicon carbide resonators.

2.2 Device Fabrication

Silicon Carbide mesas [47], beams [43], disks [44] and high-aspect ratio gaps [48] have been demonstrated in 4H-SiC on Insulator (SiCOI) using oxide-oxide wafer bonding and

DRIE etching using SF_6/O_2 and SF_6/Ar chemistries. Doped SiCOI technology is ideal for defining and isolating resonators and electrostatic actuators. In contrast, we need HPSI carbide because the divacancies need to be in neutral charge state for quantum control experiments. This is only possible in semi-insulating materials because the defect states lie near the middle of the band-gap [49]. But semi-insulating property makes it challenging to implement electrostatic transduction [50]. Furthermore, a Silicon substrate would lead to thermal mismatch delamination issues during low-temperature testing, while using a SiC substrate would make it difficult to isolate defects in resonator layer from defects in the substrate.

The dual-side process flow for resonator fabrication eliminates the substrate thereby bypassing the challenging SiCOI wafer manufacturing steps. The HPSI 4H-SiC wafers are purchased from CREE with an orientation of <0001> and resistivity 109 Ohm-cm and wafer thickness of 500 microns. The wafer is first thinned by NovaSiC to 200 microns by mechanical grinding and polishing. Standard solvent and Nanostrip cleaning protocols are done followed electron beam evaporation of a thin layer of Ti/Au to serve as a seed layer for nickel etch mask electroplating on both sides of the wafer. The backside of the wafer is spin-coated with photoresist AZ 9260, baked, and UV exposed on Karl Suss MA6 Mask Aligner to define the backside trench. This is followed by 9 um thick nickel electroplating using nickel sulfamate solution while the front-side is protected by photoresist.

After backside plating, the wafer is soaked in PRS 2000 and solvent cleaned to dissolve and clean the photoresist residues. The front side is then spin coated with AZ 9260 and patterned for nickel plating using backside alignment features of the mask aligner. The backside is protected with adhesive clear tape while plating the front side. A minimum of 4 um of nickel is deposited. After electroplating, the photoresist is dissolved, and the wafer solvent cleaned for deep trench etching. The backside etch is carried out first using Panasonic E620 ICP/RIE etcher. The sample is attached to a 6-inch carrier wafer using crystal bond. 4H-SiC is etched in SF6 and Ar chemistry using RF power of 1000 W, a bias power of 40 W, and pressure of 1 Pa. The etch rate is measured to be 100 nm/min. The backside is etched to a depth of 190 um and then the front side is etched to 10 um to release the cantilevers

(Fig. 5.1). After dissolving and stripping the nickel mask, further blanket etching can be performed to fine-tune and achieve the desired resonator thickness.

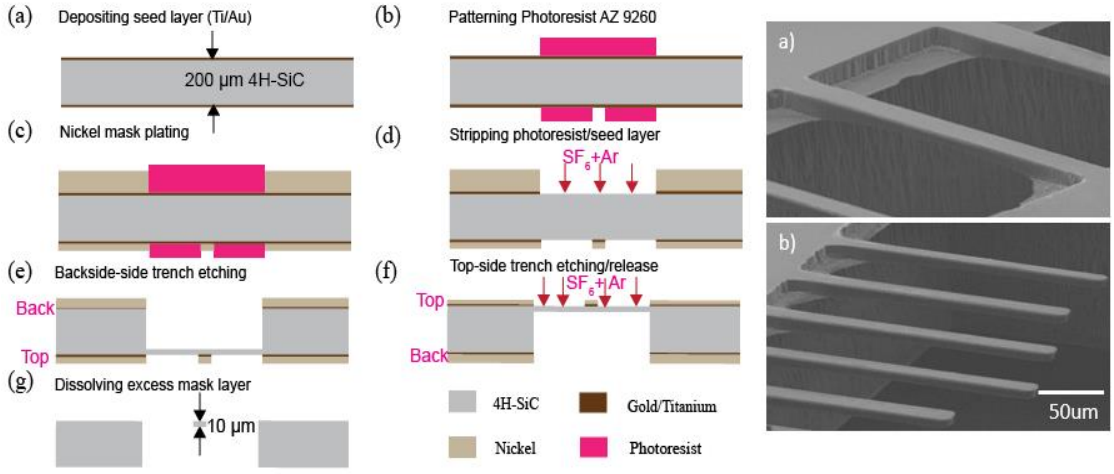

Figure 2.1. (Left) Dual-side multi-level fabrication process to manufacture SiC resonators. Nickel masks are defined on both sides prior to etching. The slow etch rates ensures no footing effect at the base during the 190 um backside etch. After release Nickel and seed layer are stripped leaving behind pristine SiC resonators; (Right) SEMs of clamped-clamped beams (a) and cantilevers (b). The sidewalls are smooth no micro-masking because we reduced the etch-rate compared to [47]. Small diaphragms are left at the anchor after front-side release, potentially undermining the Q.

2.3 Experimental Results

The Silicon Carbide chip is mounted on an axial PZT actuator using copper tape. The same is positioned inside a Karl Suss vacuum probe station (10^{-3} Torr) and the motion of the cantilevers is detected by LDV while the PZT substrate is ultrasonically driven by a signal generator built within the LDV (Fig. 5.2). We use the LDV together with a Zurich lock-in amplifier to obtain wide frequency response of the SiC cantilevers. We map the measurements to COMSOL simulations to identify different harmonics and mode families. Fig. 5.3 shows the cantilevers fundamental and higher harmonic modes of vibration. Horizontally moving vibration modes are not seen here because the PZT only generates stress waves in the vertical direction. Fig. 5.4 shows the ring-down response of the cantilever's fundamental bending mode at 312.5 kHz, demonstrating a measured Q of 12576 on a Keysight oscilloscope.

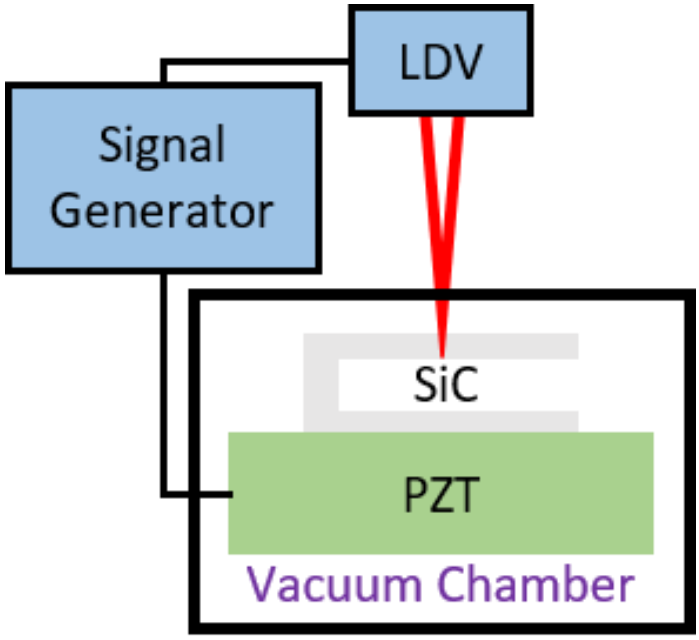

Figure 2.2. LDV setup to characterize resonators in vacuum. The drive stimulus is provided by a bulk PZT actuator to the resonator chip.

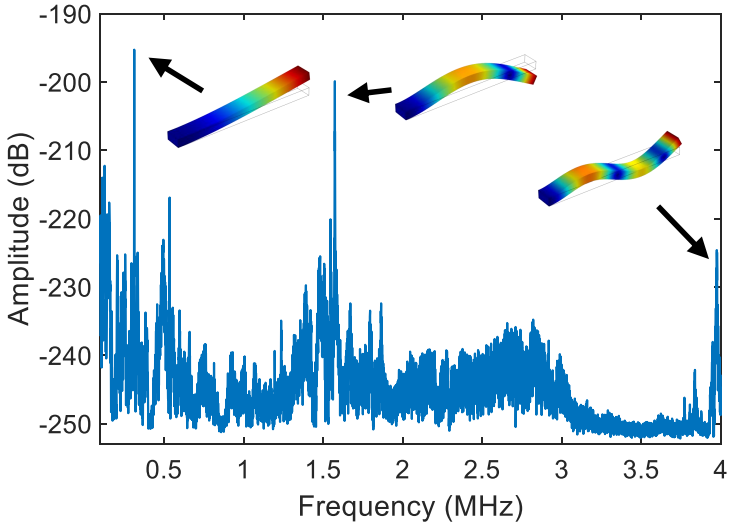

Figure 2.3. Broad band spectrum response of a 300 um long cantilever to a random number driven stimulus showing the fundamental and harmonic bending modes.

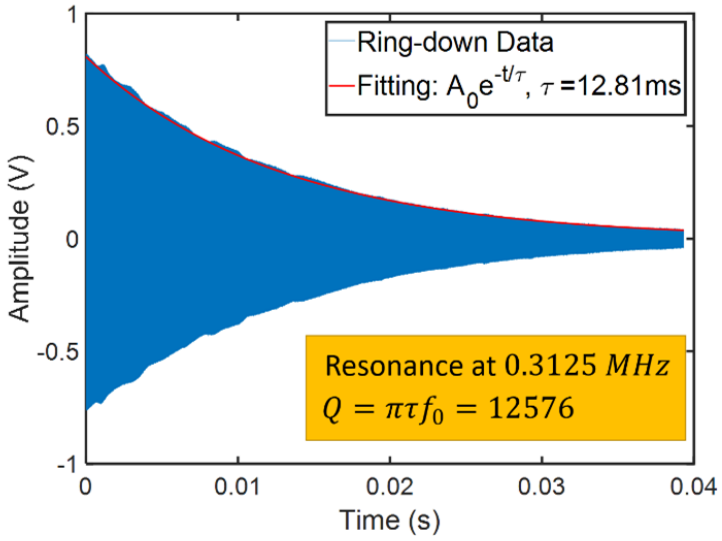

Figure 2.4. Cantilever ring down measurement in vacuum, achieving a mechanical Q of 12,576 at 312 kHz in spite of the non-ideal anchor seen in Fig. 5.1.

According to Euler–Bernoulli beam theory, the maximum stress in a cantilever's fundamental bending mode is located at the anchor point on the beam's both surfaces, which can be written as:

$$|\mathrm{T_{max}}| = \frac{3\mathrm{Eb}}{2\mathrm{L}^2} z \tag{2.1}$$

Here E is the Young's modulus of 4H SiC, b is the thickness of the cantilever, L is the length, and z is the tip displacement of the cantilever.

The divacancies in silicon carbide demonstrate outstanding coherence at low temperatures [49]. At this temperature, there is an upper voltage limit of how hard we can drive the PZT. It is important to reduce the mechanical stiffness and increase mechanical motion by increasing mechanical Q in order to achieve the largest displacement for a given fixed drive amplitude.

We actuated the PZT using a 3V sine wave near the mechanical resonance and measured the tip-displacement of one cantilever of 52.3 nm. This beam is 140 um long and 10 um thick. The mechanical stress at the base of the resonator is calculated to be 20 MPa from equation (1) despite having a mechanical Q of just 2578. We further thinned the resonators all the way down to 5 microns thick and thinner. However as shown in Table 2.1, the PZT ultrasonic device does not couple strongly to the thin resonators. Even though we measured 10X higher mechanical Q, the absolute displacement was 10X smaller.

While other stress generators like tuning-fork resonators have higher Q, they do so by canceling stress moments at the anchor, an undesirable property since we need the high stress to couple to divacancy spins. The cantilever base top-surface has in-plane X-axis stress, making them ideal resonant actuators to study phonon-spin interactions with divacancies.

Table 2.1. Summary of measured quality factor, Z displacement and calculated anchor stress for cantilever resonators of different dimensions.

Resonator			Freq (MHz)	Q	Z Motion (nm)	Stress at Anchor (MPa)
Length (um)	Width (um)	Height (um)				
140	20	10	1.848	2578	52.3	20.01
300	25	5	0.382	10273	7.9	0.33
350	15	5	0.448	6587	9.2	0.28
300	15	5	0.287	10975	8.1	0.34
300	10	5	0.299	6560	7.6	0.32
234	20	3	0.083	34963	4.4	0.18

2.4 Conclusion

We have successfully demonstrated the use of HPSI 4H-SiC in the fabrication of cantilever resonators by using a dual-side ICP-DRIE etch process. The cantilevers have quality factors $> 34{,}000$ in vacuum, however, consistently achieving anchor stress > 10MPa is still elusive. Work is currently underway to characterize resonator surfaces after etching and improving the efficiency of PZT ultrasonic driving of thin resonators. Most importantly the divacancies on the top-surface of the resonators are preserved by the dual-side fabrication process (Fig. 5.5).

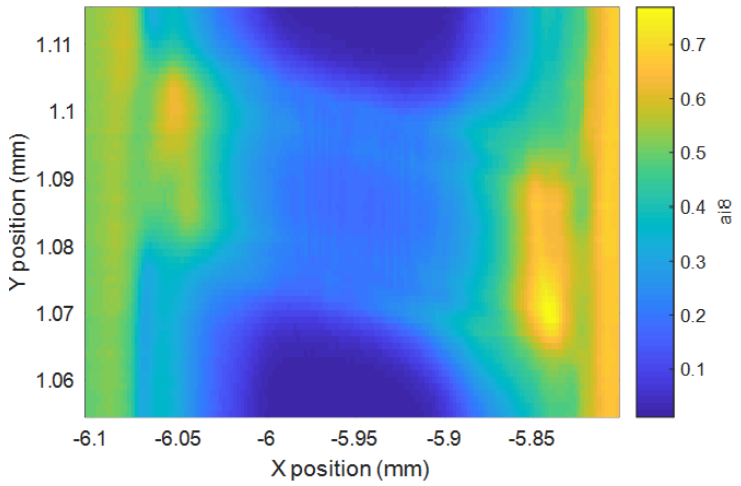

Figure 2.5. Photoluminescence of divacancies of a clamped-clamped resonator from Fig. 5.1. The divacancies are excited with a 976-nm pump laser before PL is collected at cryogenic temperature. The bright yellow areas on both sides of the beam indicate a larger quantity of color centers near the anchor and on the chip base, which increases with the bulk SiC thickness.

3. SUBSTRATE-LESS SILICON CARBIDE LATERAL BULK ACOUSTIC WAVE RESONATOR WITH REDUCED DISSIPATION

3.1 Introduction

Silicon Carbide (SiC) has been a promising candidate for the next generation MEMS material as a replacement for silicon. SiC retains its high hardness and elasticity at high temperatures, has a high thermal conductivity and is chemically inert, making it suitable for use in unconventional MEMS applications, such as aerospace, military, as well as quantum computation and sensing, where we urgently need MEMS devices to be able to operate at extremely high temperature (above 300°C [51]) or cryogenic (below 4 K [41]).

To utilize these properties of the material, MEMS researchers have applied SiC in a wide range of platforms, including SiC cantilever with PZT actuation [52], High overtone Bulk Acoustic Wave Resonator with semi-confocal lens (SCHBAR) [53], capacitively driven disk resonator [44]. Yet various material processing and device fabrication challenges continue to persist. For instance, low yield of SCHBAR devices made on mm size slabs makes it difficult to realize wafer size production. In the cantilevers made by Boyang, et al. and the disk resonators on phononic crystal (PnC) substrate by Ayazi, et al., the actuator for the MEMS resonator is not directly integrated into the design, but involves wire bonding to outer source, which miss the chance of utilizing the latest development in MEMS piezoelectric materials.

The Lateral Overtone Bulk Acoustic Wave Resonator (LOBAR) devices made by Songbin, et al.[54] has so far shown great resonance performance and are easy to fabricate on a wafer scale. Yet limitations exist in the work and need further development. The fabrication is based on 3C-SiC, as it is the only SiC polytype that can be epitaxially grown on a silicon substrate. This limits the device's ability to be integrated with other applications such as MOSFET, MESFET and quantum computation, where 4H and 6H SiC shine [55]. In a SiC-Oxide-Silicon stack, the SiO_2 and Si also exhibit higher intrinsic damping than SiC, becoming a source of substrate loss.

In terms of characterizing these devices' performance, quality factor (Q) reflects how much energy is stored in resonance versus the part lost to the system. A higher Q indicates

less energy dissipated. Whether MEMS resonators are used as filters, oscillators or sensors, Q often determines the overall efficiency. A concise summary of loss sources affecting the mechanical system's Q can be written as Equation 3.1

$$\begin{aligned}\frac{1}{Q} &= \frac{1}{Q_{material}} + \frac{1}{Q_{external}} \\ \frac{1}{Q_{material}} &= \frac{1}{Q_{AKE}} + \frac{1}{Q_{TED}} + \frac{1}{Q_{dielectric}} \\ \frac{1}{Q_{external}} &= \frac{1}{Q_{surface}} + \frac{1}{Q_{gas}} + \frac{1}{Q_{anchor}} + \frac{1}{Q_{extra}}\end{aligned} \tag{3.1}$$

Here these factors can be categories into material-related and external resonator design related. Q_{AKE} represents the phonon-phonon scattering in a material, decided by the intrinsic material property and temperature only. SiC is one of the best performing material known, giving a frequency-Q ($f \cdot Q$) product of 6.4×10^{14} [23] in Akhiezer (AKE) regime. Thus it is not the main problem we are facing in SiC platform. Q_{TED} represents the thermo-elastic dissipation, which also involves material constants plus the strain distribution in the resonance modes, again SiC has been proved to be a outstanding candidate here [44]. The dielectric loss ($Q_{dielectric}$) can be reduced by carefully selecting the micromachining process and stacked layers [56]. As for the design related loss, surface loss ($Q_{surface}$) can be reduced by post-process like annealing [57], gas damping (Q_{gas}) will be eliminated by vacuum package. Yet the anchor loss (Q_{gas}), by which the mechanical energy leaks into the resonator substrate, remains an active design challenge, especially when we migrate from silicon to novel materials, traditional solutions need to be revised or replaced with new fabrication techniques.

At a closer examination on the issue, the Q_{anchor} is determined by 2 parts corresponding to the structure: the tether, and the supporting substrate which the tether is directly connected to. As we can see in Fig.5.1(a), typical MEMS resonators are built on Si on insulator (SOI) structure. In this way, mechanical dissipation is radiated into the tether and further into both the wafer layers outside and the substrate layer right under the device.

The tether design has been widely studied. Besides conventional $\lambda/4$ length requirement, people have integrated phononic crystal [58] into it so that the energy cannot leak through the forbidden band. Notably, Reza, et al invented an acoustic reflector which can reflect part

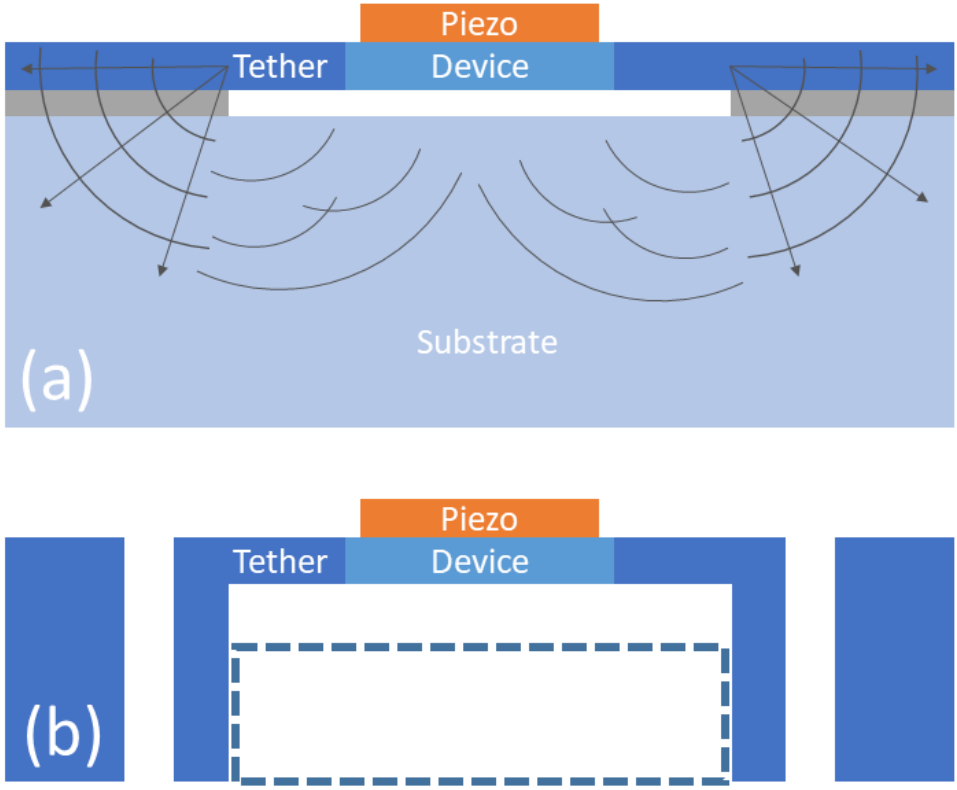

Figure 3.1. (a) Traditional MEMS resonator design cross-section with SOI technology. The mechanical wave leaks through the tether to both the outer region and the substrate mass right under the device area. (b) Our design where the damping mass under the device is etched away, and Mesa Reflector cuts off radiation outwards

of the escaping wave back into the resonator. For the surrounding substrate volume, there are multiple papers looking into this matter too, such as placing the device sitting on top of a phononic crystal substrate [44], and building Mesa isolating trenches [59]. However, as the device layer and substrate layer consist of different materials which require specific fabrication technology, these promising tether and substrate designs are difficult to be integrated together to achieve the maximized Q boost.

Here, we are reporting a new MEMS isolation technology based on a new fabrication process we developed shown in Fig. 5.1(b). We used the process to make substrate-less LOBARs based on a single 4H SiC wafer, with no additional substrate material needed. As a result, we eliminate the damping mass under the resonator area, and further extended the acoustic reflector into the thickness of the whole wafer. This type of new design achieves a similar effect of the Mesa isolation at depth while also performs the traditional reflector rule on the surface wave on the device height, thus we call it Mesa Reflector. To test the effect of the isolation, we choose LOBAR as the platform, for its extremely high Q nature at high frequency, so that any change on it can be observed clearly. However, this technique shall be able to apply on any MEMS resonators with similar anchors.

In the work, first, the design principles and simulation will be introduced, followed by detailed fabrication process. Then electrical transmission measurement shall be presented. We will analyze how the Mesa Reflector improved the overall performance on the LOBAR devices. Finally, we will discuss the limitation as well as possible improvements of this design.

3.2 Design and Simulation

An 3D illustration for the device we made is shown in Fig. 5.2. Here we shall split the explanation into the resonator (LOBAR) part and the anchor (Mesa Reflector) part.

3.2.1 LOBAR

The detailed design parameters for LOBAR are well studied in [60]. In this work, we mainly use the following as they are shown in Fig. 5.2: (1) W_{LOBAR}, width of the LOBAR; (2) L_{LOBAR}, length of the LOBAR; (3) t_{LOBAR}, thickness of the SiC layer in LOBAR device;

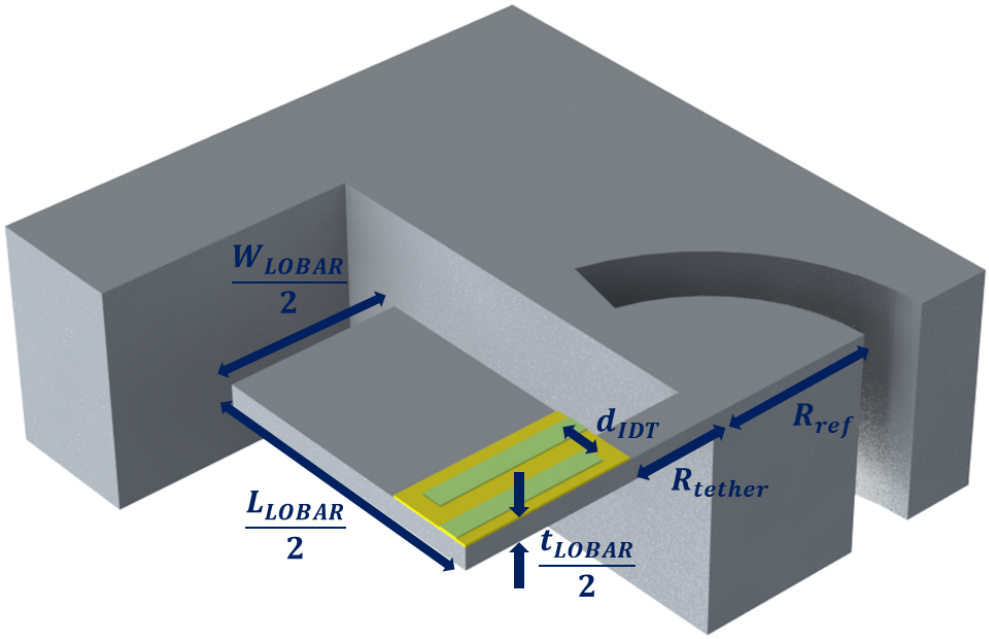

Figure 3.2. 1/4 of the LOBAR resonator connected to the anchor area.

(4) d_{IDT}, gap between the center of the interdigital transducers (IDT); (5) N, IDT finger numbers. The tether design will be discussed in the next section. For simplicity of the experiment and fabrication, we fix $W_{LOBAR} = 300$ um, and IDT finger number as 4. Among the rest of the parameters, d_{IDT} determines the central resonance frequency of the LOBAR, while L_{LOBAR} decides the distance between neighboring overtone modes in frequency. t_{LOBAR} affects the coupling strength of the piezoelectric material and SiC layer. In order to find out an optimal design, we run COMSOL simulation in 2D for the LOBAR modes.

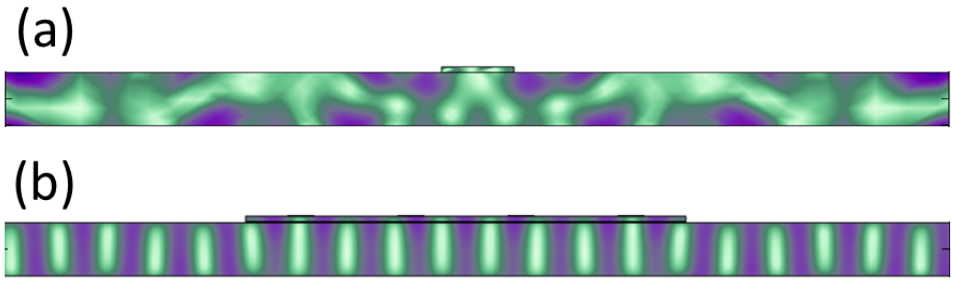

Figure 3.3. COMSOL simulation of the LOBAR device eigenmodes displacement (a) a 10um thick LOBAR operating at 450 MHz, the acoustic wave failed to penetrate the whole SiC layer. (b) a 10um thick LOBAR at 300 MHz, the mode is working as intended throughout the SiC depth.

The simulation result shows that, the thicker the SiC is and the higher the frequency is, the more difficulty LOBAR mode will have to penetrate the whole thickness. As it is shown in Fig. 5.3, when the target frequency for the IDT goes too high at given a SiC thickness, the resonance cannot form a complete standing wave across thickness and become diffracted around the volume. Given this result and consider the fabrication yield of our process which will be introduced later, we decide to target the SiC thickness around or slightly below 10 um, and working frequency at 300 MHz. These correspond to $d_{IDT} = 20.8$ um at half of the wavelength, and we fix L_{LOBAR} at 2 values: 1665 um for 40 overtones, and 83 um, when it becomes a simple lateral bulk acoustic wave resonator without overtone. To distinguish the two, we will call the former LOBAR, and the latter LBAR (Lateral Bulk Acoustic Wave

Resonator) in the chapter. Given a 12,500 m/s longitudinal acoustic velocity in 4H-SiC [61], we shall expect the frequency distance between two overtone modes to be

$$\Delta f = \frac{v}{L_{LOBAR}} = 7.5 \text{ MHz} \tag{3.2}$$

3.2.2 Mesa Reflector

A typical mesa in semiconductors is a region where the device stands above the substrate around it. This structure can be formed using chemical etching or reactive ion etching (RIE) [62]. In our case however, there is no individual substrate layer, so our trench for the mesa goes as deep as the wafer itself. As such, the design serves dual purposes:

(1) For the acoustic wave travelling on the top surface level of the wafer, the reflector can turn around the wave 180° back into the resonator volume, which is already well understood by researchers like in [63]. In this application, if we treat the leaking wave from LOBAR as a spherical wave travelling into the wafer, from wave interference we can see that:

$$\begin{aligned} R_{max} &= N \cdot \tfrac{\lambda}{2}, N = 1, 2, \cdots \\ R_{min} &= N \cdot \tfrac{\lambda}{2} + \tfrac{\lambda}{4}, N = 1, 2, \cdots \end{aligned} \tag{3.3}$$

Here R_{max} is when the standing wave in the LOBAR and the reflected wave add up to improve the Q, and R_{min} causes them to cancel each other, resulting in a lower Q.

One question remains unclear from the previous research however, is where the wave radiating from the resonator body centers at. Because we have a tether supporting the resonator, the length of it is non-negligible . As Fig. 5.4 suggests, in order to study this, we have designed arc reflectors centering either at the outer or the inner edge of the tether. R_{ref} is also varied by a $\lambda/4$ step on each design so that we can confirm the enhancing or canceling by the reflected wave.

Another design point of interest is the bottom electrode in the LOBAR. Previous study [64] suggests that a floating bottom electrode in the lamb mode resonator might be beneficial to Q and improves the overall device performance. So far all of the LOBAR resonator studies

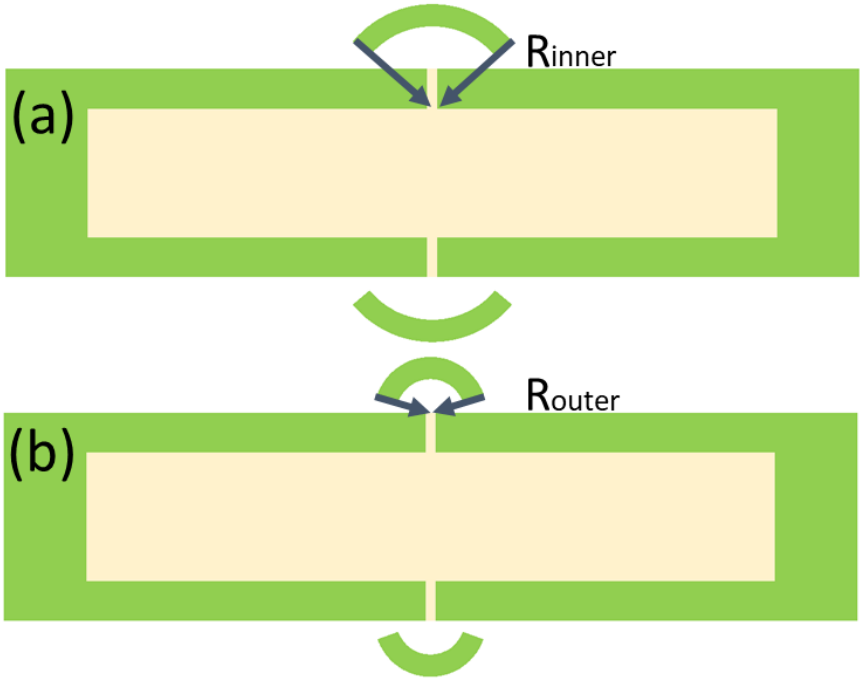

Figure 3.4. Reflector's center can be varied between (a) inner side of the tether and (b) outer side of the tether

were done on a grounded bottom electrode. Here we add a set of floating bottom electrodes, in order to observe their effect on LOBARs.

(2) Because of the depth of the trench in the Mesa and our fabrication techniques, besides the wave travelling horizontally out of the device, we can eliminate the acoustic wave leaked to the damping mass under the device and those who can diffract at and thus bypass a shallow reflector just on the device height. To fully capture the effect of such design, we use COMSOL Multiphysics® software on a 2D simulation.

In the simulation, we set a total wafer thickness of 200 um, and build the resonator according to the parameters discussed in the previous section. For the simplicity of damping factors, we do not use silicon dioxide layer and silicon substrate in the model, but a whole wafer based on SiC, AlN and metal electrode layers. As Fig. 5.5 suggests, our Mesa Reflector setup not only avoids leakage into the wafer horizontally, but also removes the standing wave traditionally formed in the substrate under the resonator.

Based on this, from the definition of Q:

$$Q \equiv 2\pi \cdot \frac{E_{\text{stored}}}{E_{\text{dissipated}}} \tag{3.4}$$

Since the Mesa reflector can confine more energy inside the resonator body instead of dissipate it, we shall expect a Q improvement in the RF measurement.

3.3 Fabrication

We fabricate the SiC LOBAR devices starting from a 500 um thick Semi Insulating 4H-SiC wafer purchased from Cree Inc. The wafer is then thinned down to 200 um thick by chemical mechanical polishing (CMP). The detailed process is shown in Fig. 5.9(a): (1) a Mo-AlN-Mo stack is deposited by OEM Group Inc. on the whole wafer, where each Mo layer thickness is 100 nm and AlN is 1 um. After that, we perform optical lithography with a MLA150 Maskless Aligner made by Heidelberg Instruments, which enables sub um level precision without the tedious electron beam lithography process. (2) The Mo-AlN-Mo stack is etched by inductively coupled plasma reactive-ion etching (ICP-RIE) with a mixture of $BCl_3/Cl_2/O_2$ gas. The etching can be controlled accurately to stop on the SiC surface,

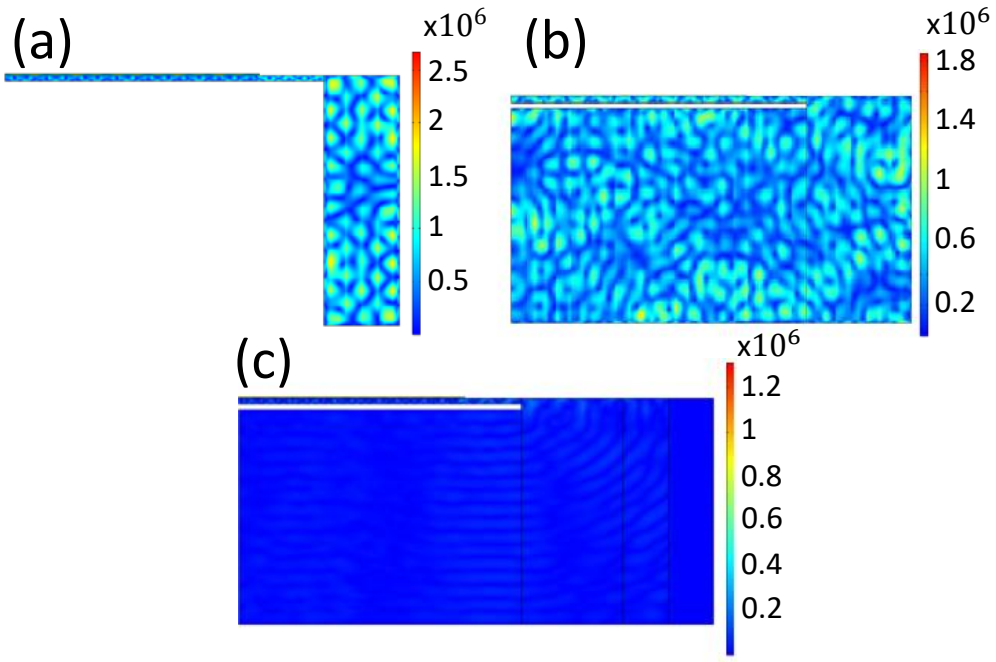

Figure 3.5. Total stress (N/m^2) in symmetric cross-sections along the tether's direction of different resonator setup : (a) Mesa Reflector. The mechanical wave only stay in the Mesa island near the resonator; (b) Mesa Reflector but with the damping mass underlying the LOBAR. The mechanical wave forms a standing wave under in the damping mass region, which lowers the energy concentrated in the resonator part; (c) With no reflector. A perfectly matched layer (PML) is added to the right side to simulate substrate loss. Acoustic energy is leaking both to the right side and downwards into the wafer.

because SiC is resistant to chlorine-based chemistry and have a low etch rate compared with Mo or AlN. (3) The top electrode is defined by Cl_2 and O_2 based ICP-RIE. AlN does not react actively with these two gases but BCl_3, so this etching can be stopped on AlN easily. (4) For the hardmask of the following SiC etching, we deposit a 4 um thick Nickel (Ni) hardmask with electroplating technique developed in our previous work [52] on the back side, while we use evaporation to form a Indium Tin Oxide (ITO) thin layer (600 nm) as the etching mask from the front side of SiC. (5) The ITO layer is patterned by photoresist as a soft mask, then etched by Cl_2 based ICP-RIE, in order to define the releasing window for LOBAR. (6) From the back side, the SiC is etched with SF_6 and Ar gas in STS AOE Deep Reactive Ion Etch (DRIE) system. The etch rate is about 15 um/hour. We run the etching at timely interval and actively measure the etched depth during the process. The etching is stopped when it reaches 190 um, leaving a 10 um thick SiC membrane to be released. This step effectively removes the damping mass under the resonator. (7) Turning over the wafer, we perform another DRIE on the front side of the wafer for 10 um until the LOBAR device is released. (8) Finally, we dissolve the ITO with 1:5=HCl:H_{20} diluted hydrochloric acid and leave the backside Ni mask on as it does not affect our measurement.

For the Mesa Reflector, the front 10 um and back 190 um etching process is applied at the same time when the LOBAR is being released. In this way we can etch through the whole 200 um thick wafer to make trenches for the Mesa Reflector.

It is worth noting that, because of AlN deposition difficulties on the bulk 4H-SiC wafer, we do not have a patterned bottom electrode to maximize the design benefit from study like [65]. Furthermore, it causes a problem that the signal pad in our GSG (ground-signal-ground) probe pads has a full Mo-AlN-Mo stack. Together with the 200 um thick SiC sitting under it, they formed a high overtone bulk acoustic wave resonator (HBAR) as it is shown in Fig. 5.9(b) left. These series of modes can become a major noise source in the LOBAR measurement. To counter this, we create a SiC etching trench right under the signal pad during our backside DRIE, shown in Fig. 5.9(b) right. The window serves dual purpose. First, since the SiC is much thinner than the bulk wave, the HBAR resonance frequecy is shifted to much higher value, thus the direct overlapping with LOBAR modes is avoided. Also, when the etching window is so small (the signal pad is 100 by 100 um), the DRIE will

create a domed surface due to etch rate difference from the center to the edge, which becomes a convex mirror for the incoming vertical acoustic wave from the piezoelectric layer, reflecting it out of the HBAR mode volume. In this way, we can lower the energy concentration of HBAR modes and in turn improve the Q of the LOBAR modes.

The final devices are inspected by Hitachi S-4800 Field Emission SEM. The images are shown in Fig. 3.7. The SiC LOBAR is successfully released using our front-back side etching. One difficulty in fabrication is that the main LOBAR release window are much larger than the Mesa Reflector in area, resulting a different DRIE etch rate in these two regions. Since back side etching has to define the thickness of LOBAR, we overcome the issue by extending the front side etching with ITO hardmask. Even with a thin layer of 600 nm, the ITO shows a selectivity of 1:50 over SiC, allowing a farther etching to 20 um. However, there are limitations in the currently fabrication. In the enlarged part of Fig. 3.7 (a), even though the ICP-RIE on AlN with BCl_3 can stop on SiC, it still leaves a rough surface due to heavy Cl atom bombardment. Also, in Fig. 3.7(c), a rather significant lateral etch during the DRIE can be seen, leaving a thin membrane on the edge of the releasing windows. These issues will need to be addressed in our future development.

3.4 Characterization

The RF measurement is conducted on a Cascade Microtech 11971B Probe Station with a Keysight N5230A PNA-L Network Analyzer and 2 Cascade Microtech ACP40 GSG probes. To begin with, the LOBAR devices' transmission plot with the best measured Q are presented in Fig. 3.8(a) and (b). We realize a 22% improvement on Q in the reflected LOBAR mode. In (c), the reflected LOBAR is measured to have increased Q around 300 MHz, but the modes quickly decline and even vanish below the measurement noise floor outside a 100 MHz wide range. Meanwhile, the normal LOBAR displays a lower Q at the central frequency, but overall more stable response across the whole measurement spectrum. This phenomenon will be further explored in the last part of the chapter. The $(f \cdot Q)$ product of the device is 1×10^{12}, which is lower than previous devices made in [66]. This is mainly due to our device thickness being much thicker, and the DRIE micromasking formed during our etching increasing the surface loss. Nonetheless, this Q performance is high enough for us to explore

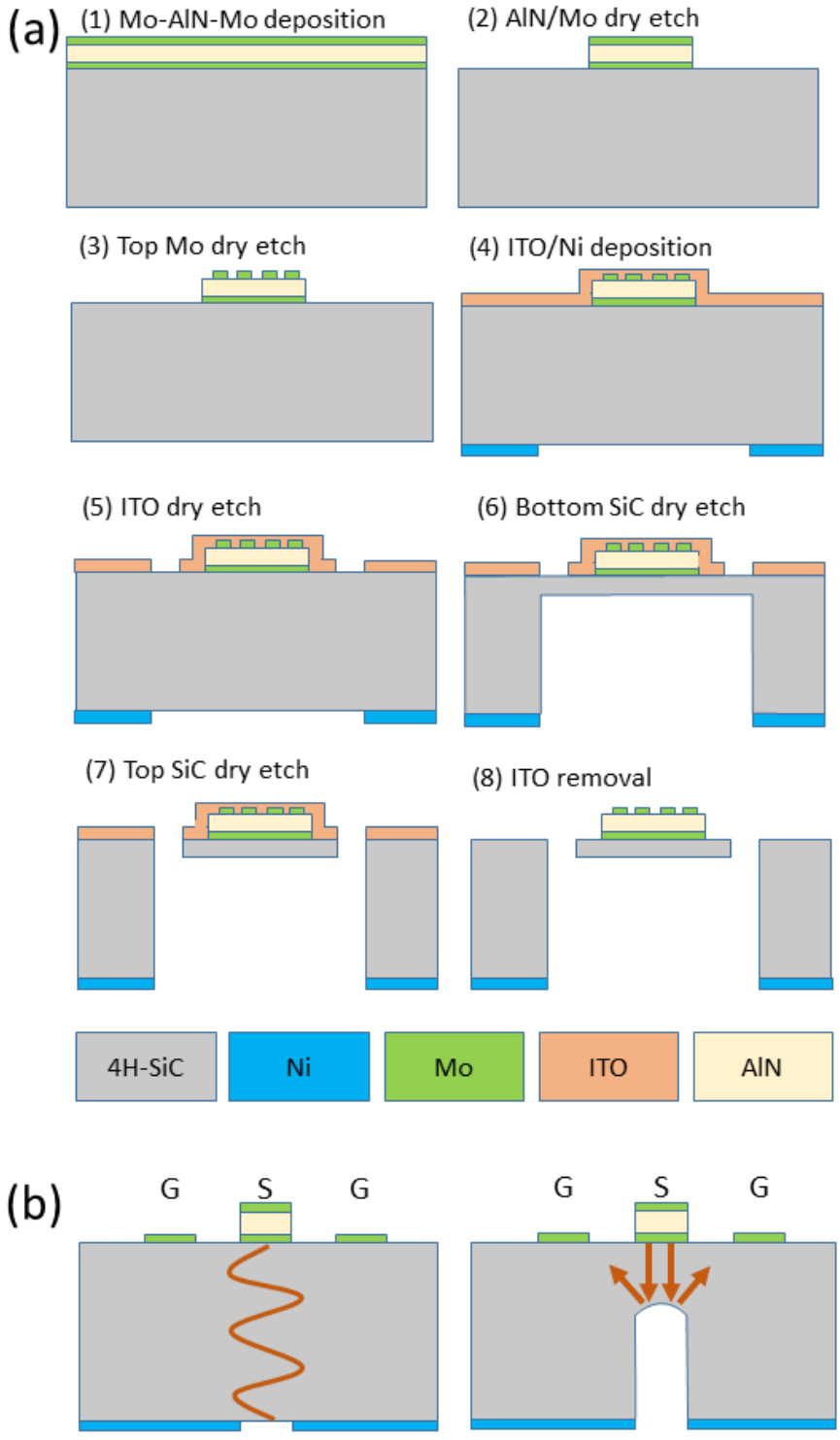

Figure 3.6. (a) Fabrication process for the SiC LOBAR resonator. (b) HBAR modes under the signal pad and their removal.

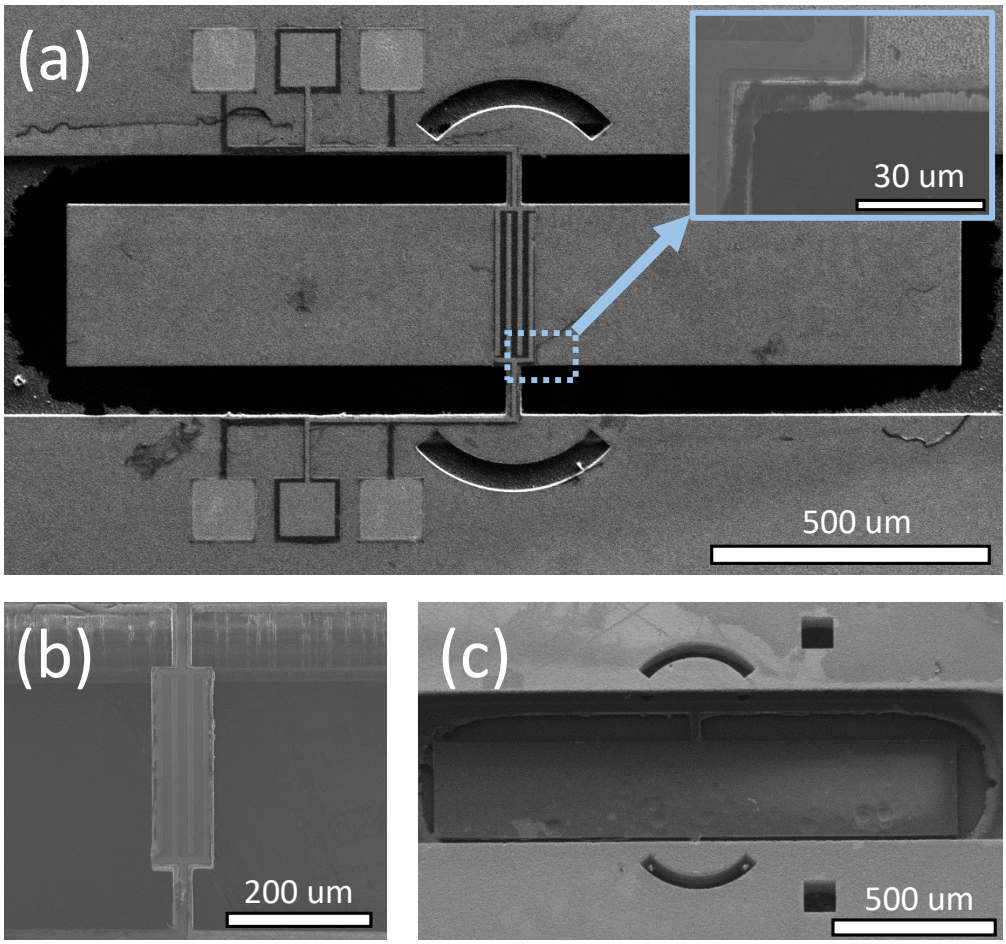

Figure 3.7. (a) Front side of a released LOBAR. The enlarged picture shows SiC surface damage during the AlN etching. (b) Front side of the released LBAR. From the top we can see clear smooth etching trenches of the 200 um SiC wafer. (c) Back side of the LOBAR. The Mesa Reflector goes through the whole wafer and has opening on both side of the wafer. The bulk SiC under the signal pad is also etched with the small square trenches shown.

multiple design parameters provided in this work below We will divide this section into measurement results featuring each of the innovations in detail.

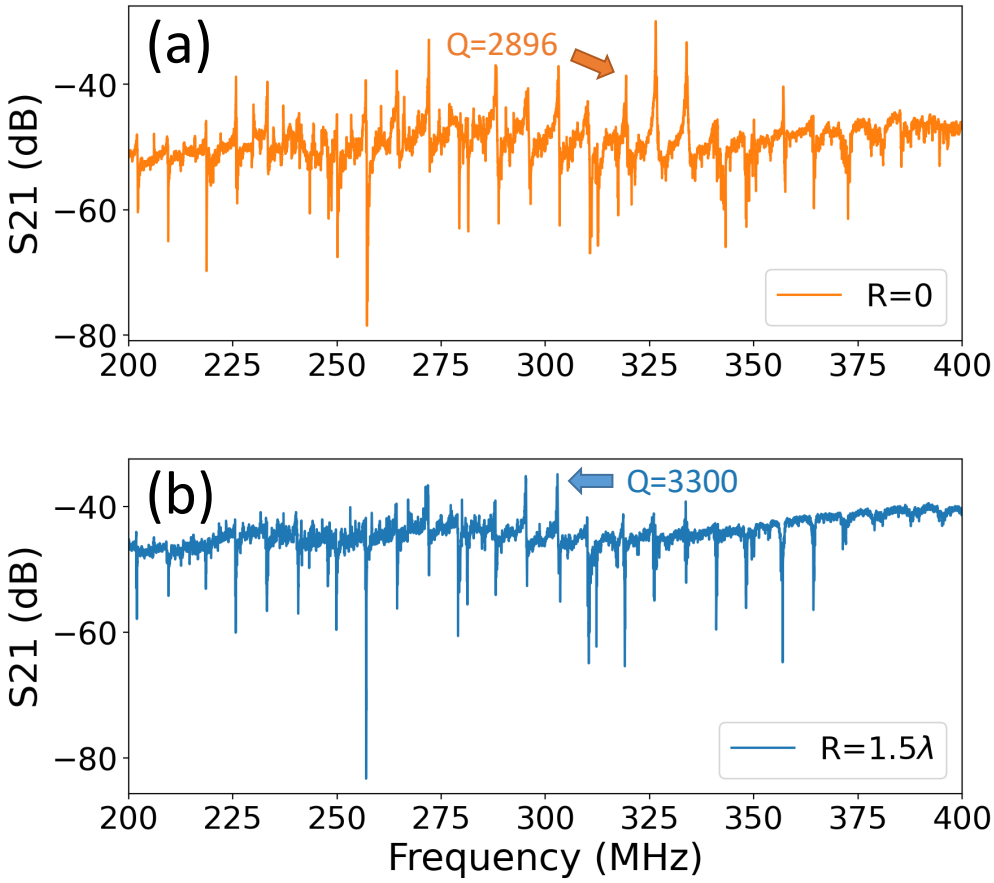

Figure 3.8. (a) LOBAR without Mesa Reflector. (b) LOBAR with Mesa Reflector, $R_{ref} = 1.5\lambda$. The reflector is frequency-sensitive. It suppresses the Q of modes away from 300 MHz. (c) Q measured in the overtone modes on both devices.

3.4.1 Signal Pad HBAR Mode Removal

First we compare two LBAR devices with the signal pad underlying etching described in the Fabrication section. The RF measurement is displayed in Fig. Here we use Lorentz peak fitting [67] to determine the Q value. 3.9. The etching trench improves the Q of the device.

Looking closer in detail, From (c) S_{11}, we measure the gap between HBAR overtones to be around 30 MHz, which agrees with the theoretical calculation:

$$f = \frac{v_{SiC}}{\lambda} = \frac{V_{SiC}}{2t_{SiC}} = \frac{12500\text{m/s}}{2 \times 200 \times 10^{-6}\text{m}} = 31.25\,\text{MHz} \tag{3.5}$$

This confirms the modes to be HBAR modes under the signal pad, while in (b) they are suppressed by the principle explained in Fig. 5.9 (b). With this result in mind, we are confident that the following LOBAR characterization will not suffer from this noise.

3.4.2 Floating vs Grounded Bottom Electrode

As it is mentioned in the design section, we fabricated resonators with bottom electrode cut open from the ground pad for GSG probes, so it can be left floating. The measurement is presented in Fig. 3.10. Different from the result in Lamb wave resonators [64], here both LBAR and LOBAR show that a grounded bottom electrode works better in terms of Q and power transmission than its floating counterpart. In particular, the LOBAR transmission suffers extremely high loss from the floating electrode, suggesting that it is not enough to drive the much larger and heavier bulk SiC layer to resonance, compared with the LBAR or Lamb Wave Resonators where the AlN and SiC are of equal size. Using this knowledge, the rest of our devices are all made on a grounded bottom electrode to enable higher Q in studying other design parameters.

3.4.3 Reflector Center and Radius

To study the effect of the reflector design, we fabricated the the trenches with variable radius as well as different centers mentioned in Fig. 5.4. In order to minimize the fabrication error in the experiment, we fabricated each of the comparing group of objects sitting close to each other on the wafer, so during the DRIE they are under a similar environment.

First, we use LBAR to study the effect of Mesa Reflector on a single mode resonator, because the close overtone modes in LOBAR makes it difficult to perform accurate measurement on the Q. In Fig. 3.11, we measure the average Q of the series of devices based grouped by their reflector radius. Note that we cannot start with R_{ref} closer than 1.5λ due

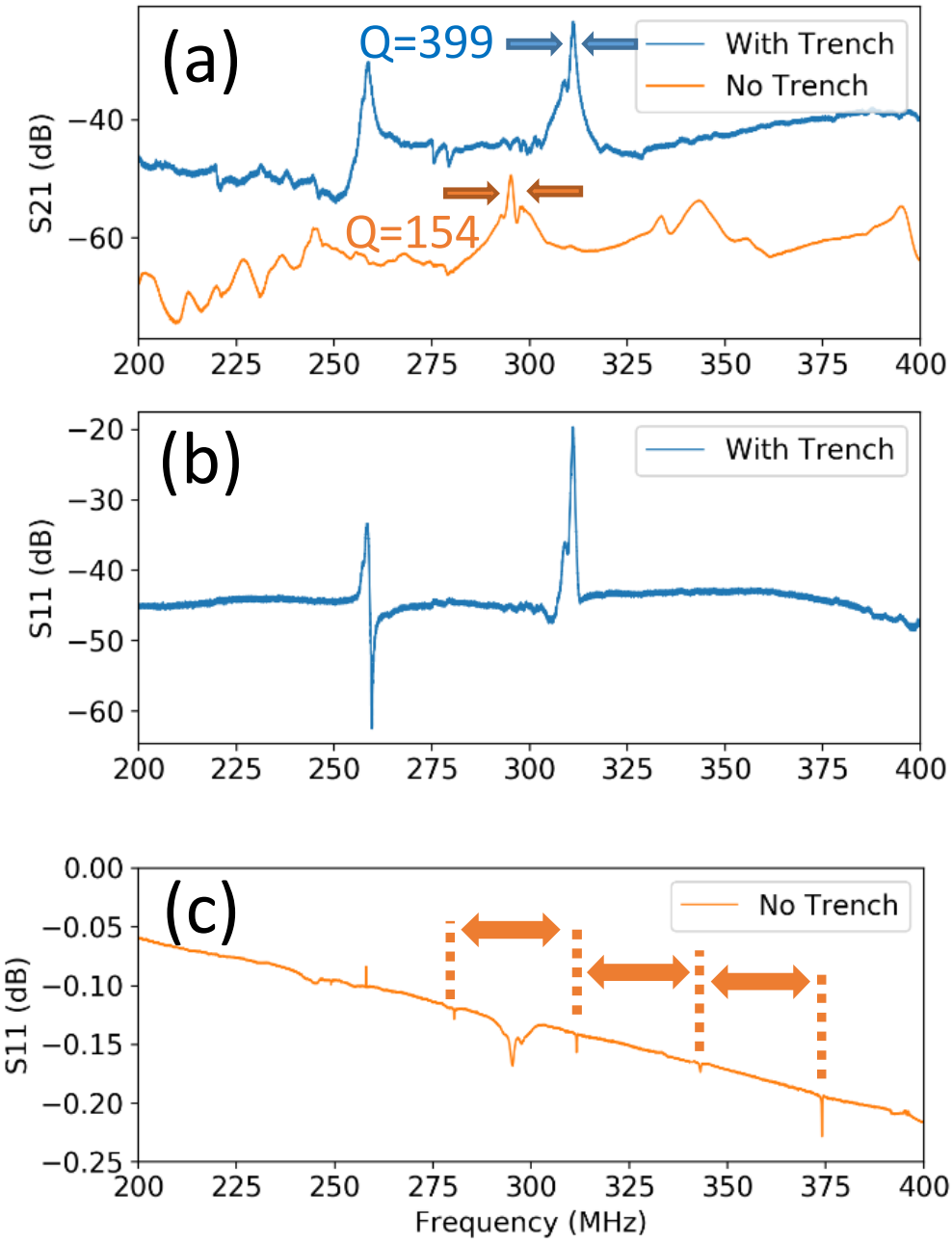

Figure 3.9. (a) S_{21} of the LBAR with and without the etching trench under signal pads. (b) S_{11} of the device with the trench. No HBAR mode can be observed. (c) S_{11} of the device without the trench. HBAR modes can be seen from the figure, and the gap is about 31 MHz, which agrees to the wafer thickness of 200 um

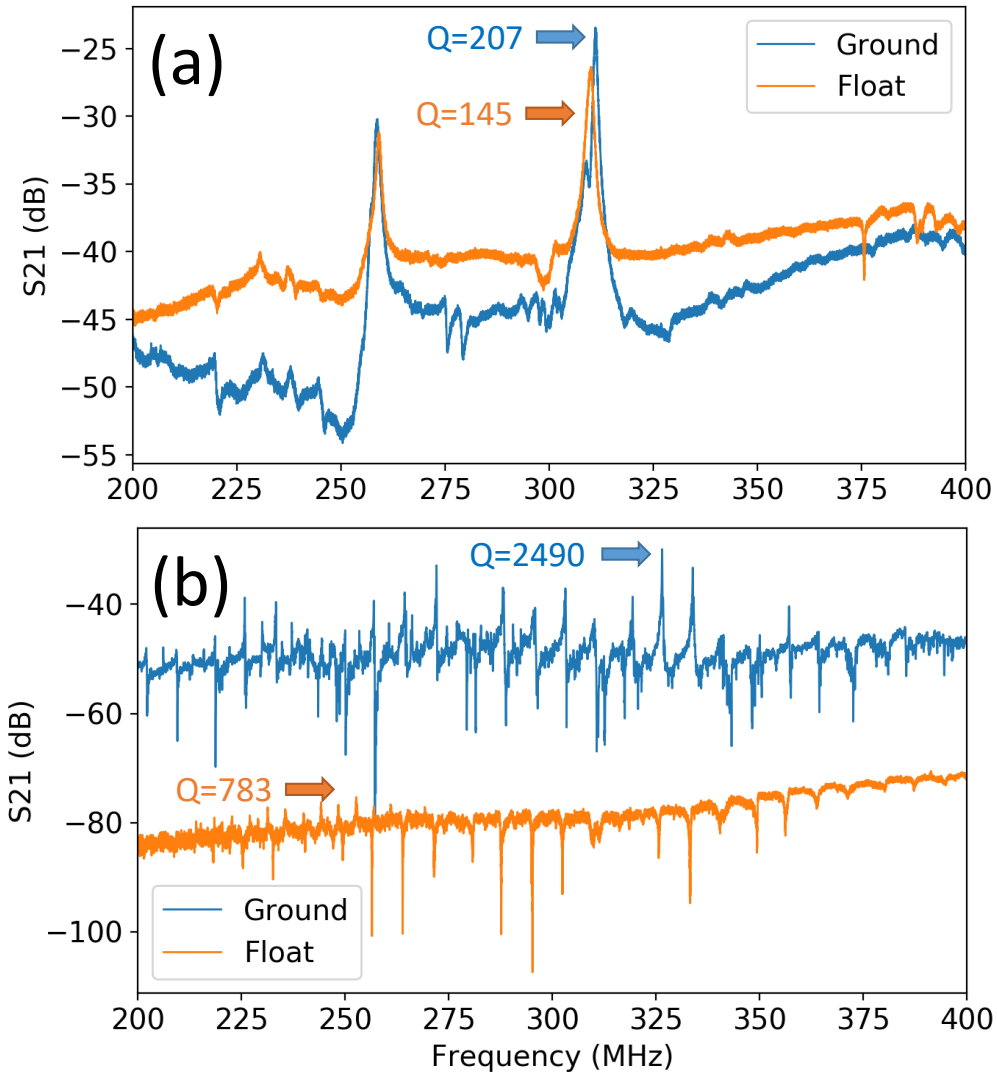

Figure 3.10. (a) S_{21} of the LBAR devices with grounded vs floating bottom electrodes. (b) S_{21} of the LOBAR devices with grounded vs floating bottom electrodes. The mode with highest Q in each device is marked.

to electrode routing. Periodical oscillation of the Q is found when the radial center is at the outer side on the tether, as Fig. 5.4(b) shows. When the center is on the inner side, we do not observe such change, but only a general decline of Q when R_{ref} increases. This can be explained by an increasing energy leakage into the wafer as the Mesa Reflector moves away from the device. Having this knowledge, we apply the outer reflector design to our LOBAR devices in the next step.

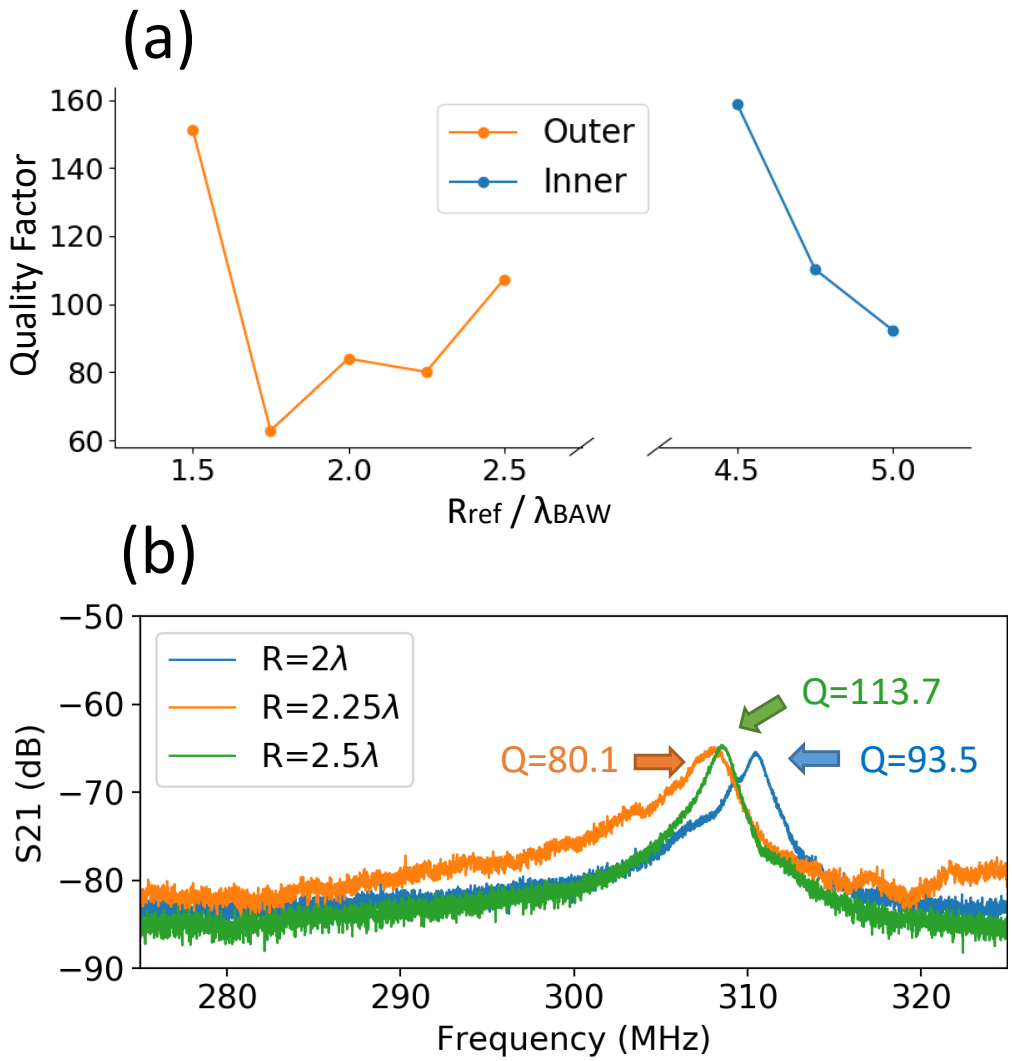

Figure 3.11. (a) The measured average Q shows periodic variation when the reflector is centered at the outer edge of the tether, but it has no such trend when the the radial center is in the inner tether edge. (b) S_{21} of a series of LBAR devices. Green and blue devices are at the optimal radius, while the yellow one is at the quarter wavelength causing signal canceling.

Meanwhile, we also measured the LOBAR devices with Mesa Reflector. Because there are overtone modes across the whole 200-400 MHz spectrum, the measurement effectively becomes a Fourier analysis of the reflector. The modulation can be expressed as:

$$\begin{aligned} y &= A\cos\left(2\pi\frac{R_{ref}}{\lambda/2}\right) \\ &= A\cos\left(\frac{4\pi R_{ref}}{\lambda}\right) \\ &= A\cos\left(\frac{4\pi\,\mathrm{R}_{ref}}{v}f\right) \end{aligned} \tag{3.6}$$

In addition, because the LOBAR has a center frequency $f_c = 300$ MHz defined by IDT gap, the closer a resonance is to the center, the stronger it tends to be. We can add a secondary exponential decay to the function so that in total:

$$y = A\cos\left(\frac{4\pi R_{ref}}{v}f\right)\cdot \mathrm{e}^{-k(f-f_c)^2} \tag{3.7}$$

Here, A is the modulation strength, v is the acoustic velocity in SiC, f is frequency, k is a normalized constant. In the previous LBAR analysis, we treat R_{ref} as the variable at a given mode, however, in LOBARs, given a fixed device's R_{ref}, we now treat frequency as the variable. Using this equation, we plot the S_{21} of the LOBARs with various reflector radius in Fig. 3.12. Although the modulation function may contain error from inaccuracy of the acoustic velocity, from the plots, we can still observe a strong modulation effect based on the frequency-radius relation. The LOBAR overtone modes will get enhanced or suppressed based on phase of the modulation function in the corresponding range. In the enhanced region, the transmission is stronger and tends to have higher Q modes. This discovery can solve a fundamental problem with LOBAR devices: Traditionally, a LOBAR has so many high Q modes sitting close to each other in the frequecy domain, that they tend to coupling to each other and thus decrease the energy efficiency in signal processing. While it is possible to design an electrical circuit to attach to it [68], a mechanical modulator with zero power consumption is certainly favorable. Similar to the reason why researchers moved from HBAR to thin-film bulk acoustic resonator (FBAR) for fewer but higher Q modes, using this idea,

we can potentially select several extremely high Q LOBAR modes across a wide frequency range and use them as the fundamental mode for filter design.

3.5 Discussion and Conclusion

We have successfully developed a new fabrication technology on 4H-SiC/AlN platform that allows bulk acoustic resonators to be made without additional substrate material. HBAR mode caused by the signal pad on the wafer is removed by DRIE undercut of the SiC under the pad. Using this innovation, we design, simulate and fabricate a 3D Mesa Reflector which combines the benefit from both mesa isolation and device layer level reflectors. Q improvement is observed on both LOBAR and LBAR resonators we make. We also investigate the real radial center of the reflector as well as the effect of a floating bottom electrode for LOBAR, which was previously unclear.

Future improvement of the work can be done on the SiC etching. Protecting the etched profile from micromasking and thinning the device further will be the keep to achieve higher Q. Further, novel piezoelectric material like Lithium Niobate [69] and Scandium-doped AlN will enable a greater future for SiC based acoustic resonators.

Furthermore, we realize a mechanical modulation of the LOBAR overtone modes based on the reflection. A math model is used to fit the modulation effect. With this discovery, we can selectively excite few modes of a resonator while suppressing the rest. This enables a future improvement on overmoded acoustic resonators not limited to LOBARs. Also, our fabrication technology allows us to expand our ability beyond reflectors. In the work done by Hailin, et al.[70], a diamond Lamb wave resonator was soaked in the bath of PnC structures. However, diamond's high cost make it hard to use in MEMS industry. With our etching technique, a wafer level phononic crystal will be achievable for the first time on SiC material, and it will bring us one step closer to eliminating anchor loss in MEMS resonators.

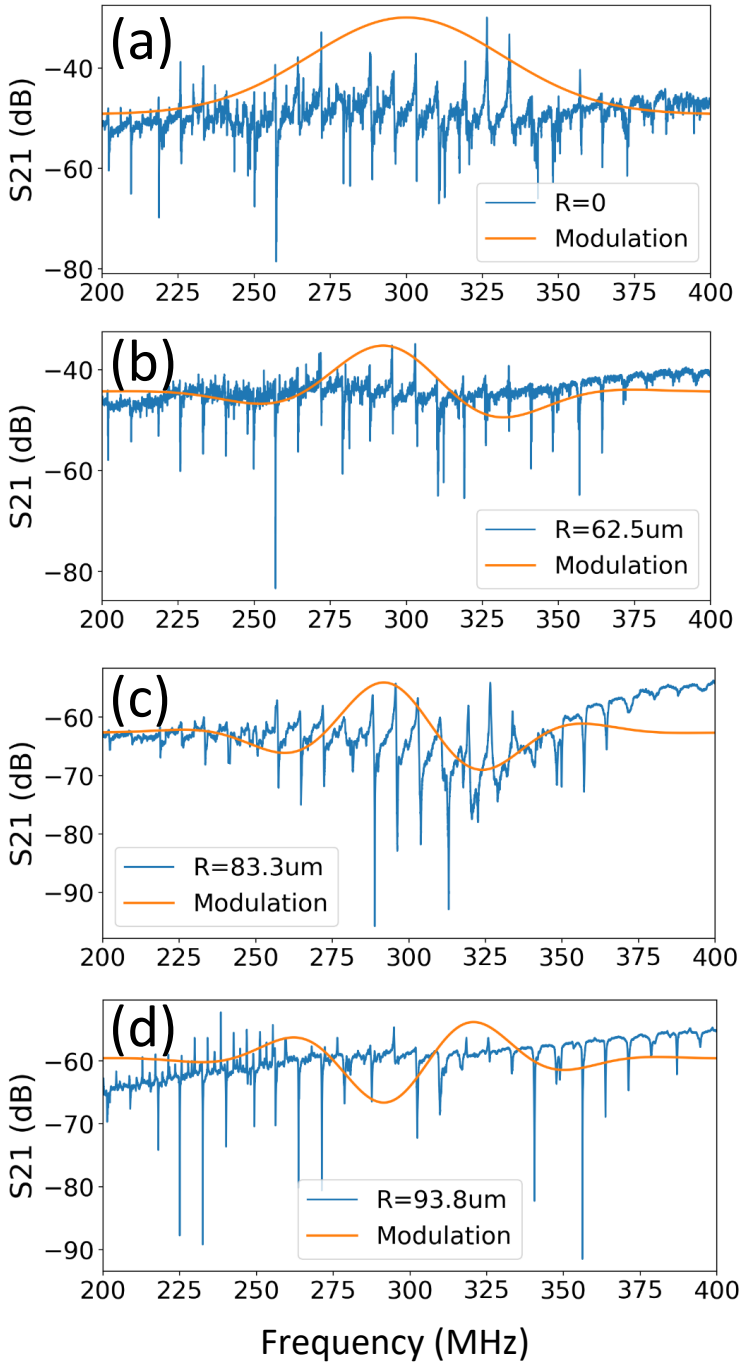

Figure 3.12. (a) LOBAR without Mesa Reflector. The resonance modes are distributed rather evenly across the range. (b)-(d) LOBAR with radius-varying Mesa Reflectors. The modulation effect changes based on the selected radius. In the enhanced region there are more high Q modes than outside.

4. STRAIN MAPPING ON FLEXURAL MODE SILICON CARBIDE MECHANICAL RESONATOR WITH PHOTOLUMINESCENCE

4.1 Introduction

Lamb wave in solid materials was first discovered by British mathematician Horace Lamb. The wave is propagating along an infinite solid plate in x-y direction, and a thickness of d in z direction. When we assuming sinusoidal solutions to the wave function, we can write x and z displacement as:

$$\begin{aligned} \epsilon &= A_x f_x(z) \mathrm{e}^{\mathrm{i}(\omega t - kx)} \\ \zeta &= A_z f_z(z) \mathrm{e}^{\mathrm{i}(\omega t - kx)} \end{aligned} \tag{4.1}$$

When we consider the z direction stress on the top and bottom surface of the plate is 0, when $z = \pm d/2$, we can find characteristic equation as such:

$$\begin{aligned} \frac{\tanh(\beta d/2)}{\tanh(\alpha d/2)} &= \frac{4\alpha\beta k^2}{(k^2+\beta^2)^2} \\ \frac{\tanh(\beta d/2)}{\tanh(\alpha d/2)} &= \frac{\left(k^2+\beta^2\right)^2}{4\alpha\beta k^2} \end{aligned} \tag{4.2}$$

The first equation is for symmetric modes and the second one is for asymmetric modes. Here,

$$\begin{aligned} \alpha^2 &= k^2 - \frac{\omega^2}{c_l^2} \\ \beta^2 &= k^2 - \frac{\omega^2}{c_t^2} \end{aligned} \tag{4.3}$$

c_l and c_t are the longitudinal wave and shear wave velocities. As it is revealed from the solution, Lamb wave modes are made of the symmetric extensional mode (S_0), the asymmetric flexural mode (A_0), and other higher order modes by mixing these two.

In MEMS researches, optical vibrometry has been widely used as a method of characterizing MEMS resonance in real time. Laser Doppler Vibrometer [71], photoelasticity effect[72] and ultrafast laser imagining [73] have been applied to MEMS devices, to capture the surface motion when the acoustic wave is propagating. However, such techniques have limitation that they can mostly image the surface vibration, but not inside the resonator bulk cavity.

In this way, they can be only used in surface acoustic wave or very thin devices. Interests remain for probing the strain distribution inside an acoustic resonator, for optimizing parameters including the quality factor and power handling capabilities.

Silicon carbide (SiC) lamb wave resonators have shown great potential with high quality factor, high piezoelectric coupling coefficient [74, 54]. Previously, our group has made high Q SiC lateral overtone bulk acoustic wave resonator (LOBAR) based on Aluminum Nitride (AlN) on 4H Semi-insulating Silicon Carbide [75]. In such platform, we demonstrated an extensional mode resonator with a Q of over 3000 at 300 MHz.

Naturally, our interest is also on the A_0 mode, since it may have higher piezoelectric coupling coefficient (K_t^2) and Q when the LOBAR is thicker[76]. In such case, more energy would be transferred from the piezoelectric transducer into the SiC resonant cavity. Thus the strain-spin coupling effect would be stronger and easier to observe. By measuring the strain-spin coupling across the whole resonator region, we can effectively map the strain intensity distribution across the cavity. Given that the spins distributes both on the surface and deep inside the SiC, we could achieve a 3D probing of the flexural mode in LOBAR.

4.2 Design

In Figure 4.1, COMSOL simulation gives the mode shape of A_0 and S_0 mode in a LOBAR resonator, with the same dimension as the one used in [75]. The resonator is made of a 10um thick SiC rectangle plate, with 1600um length and 300um width. In the center the AlN transducer is sandwiched by Molybdenum electrodes.

I use COMSOL to simulate flexural modes that can be used for the spin-strain coupling experiment. I identify 2 modes of interest at 87.5 MHz and 114.5 MHz. The strain distribution of these modes are plotted in Figure 4.2

4.3 Fabrication

The fabrication process flow is identical to Figure 3.6. The detailed description can be referred to Section 3.3. Compared with the fabrication in the last chapter, we have optimized the dry etching recipe for the SiC, thus the surface quality has been improved.

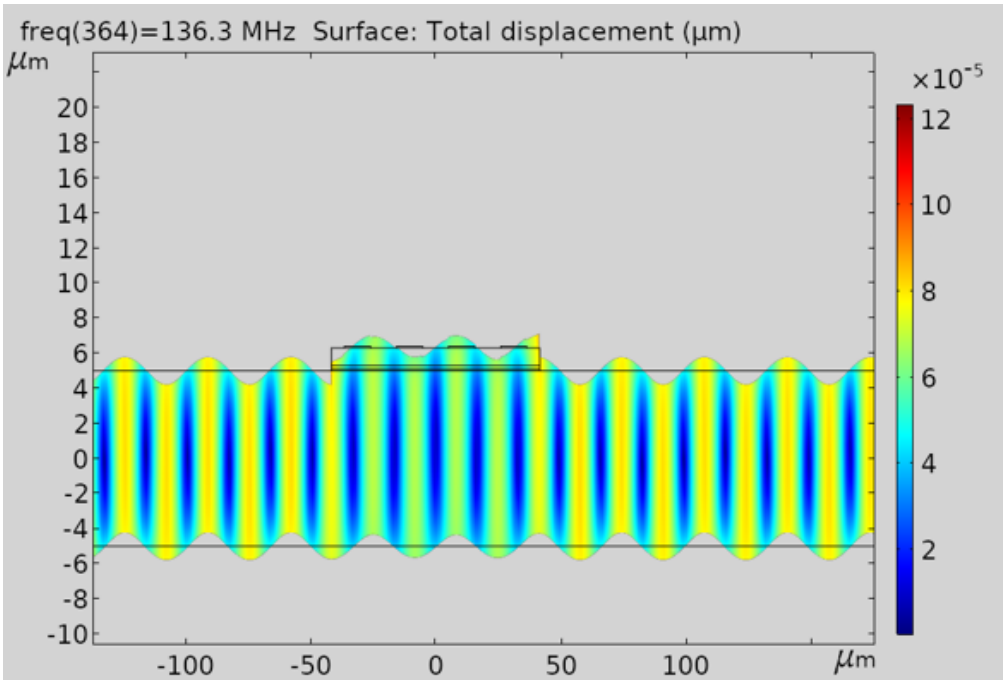

(a)

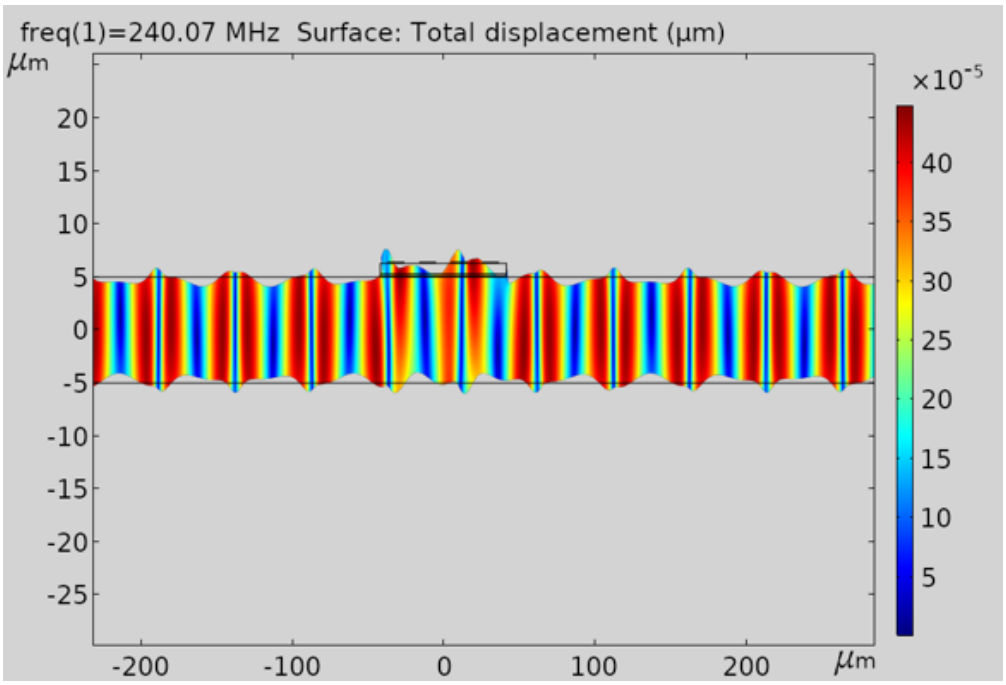

(b)

Figure 4.1. Displacement of the LOBAR around the center of (a) A_0 and (b) S_0 mode.

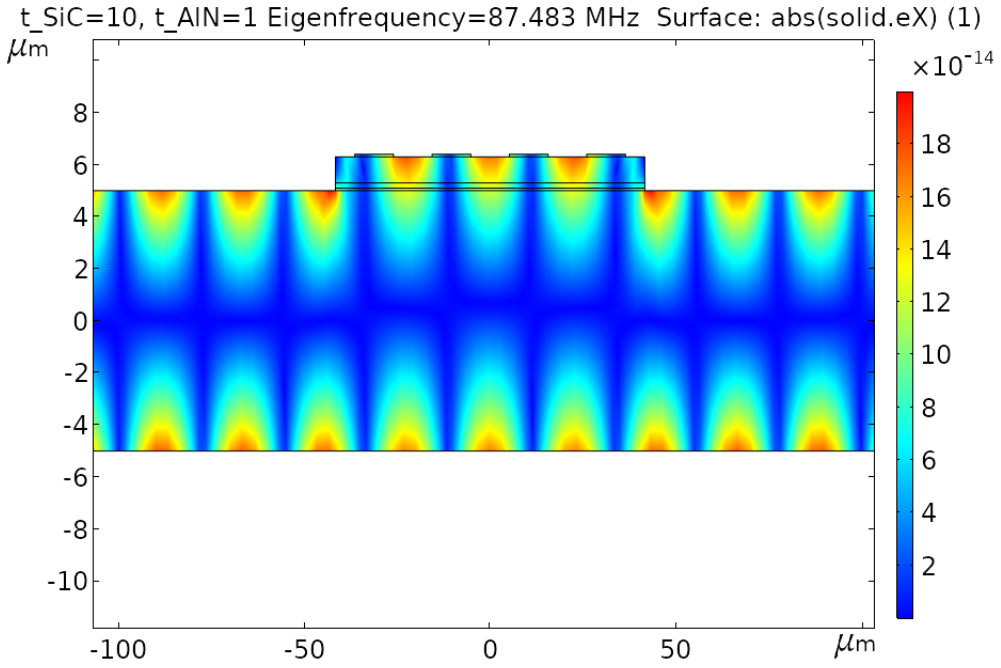

(a)

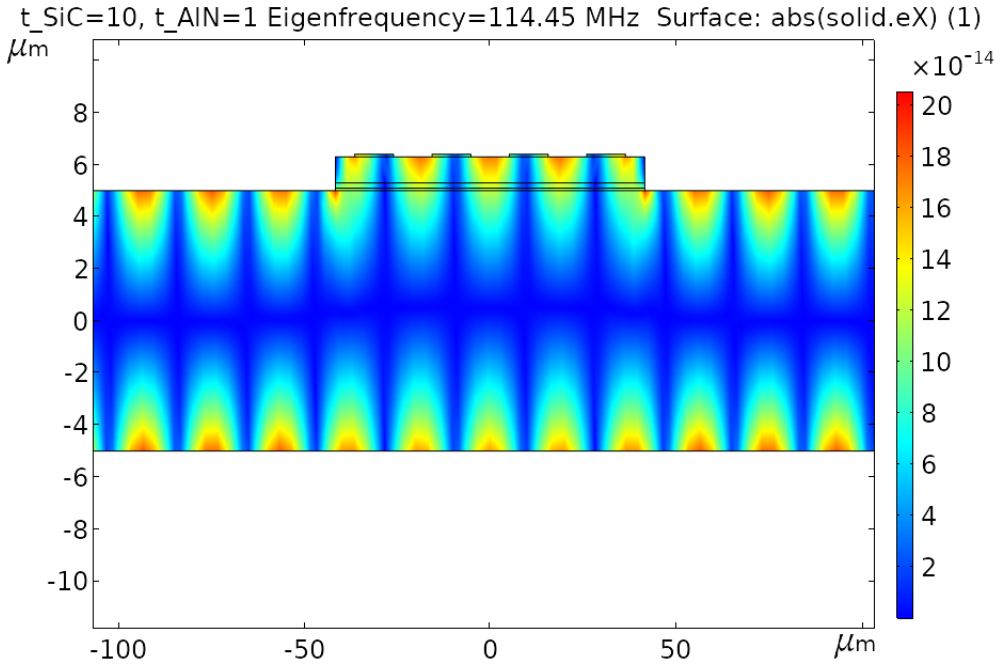

(b)

Figure 4.2. COMSOL simulation: strain distribution of the flexural mode around the LOBAR's center region at (a) 87.5 MHz and (b) 114.5 MHz.

The SEM images of the fabricated devices are shown in Figure 4.3. Compared with previous devices, the surface roughness and dimples have been greatly reduced. This allows the device to operate with lower acoustic loss, and reduces the optical scattering for the spin measurement.

4.4 Characterization

The 2 port electrical measurement is done on a Cascade Microtech 11971B Probe Station with a Keysight N5230A PNA-L Network Analyzer connected with 2 Cascade Microtech ACP40 GSG probes. The S21 measurement of one device is shown in Figure 4.4

To extract the Q of the modes, I use a Lorentzian peak fitting on the S_{21} data. A Q of 3371 is achieved in one of the overtones, which is consistent with previous work [75].

To use the LOBAR on the strain-spin coupling experiment, another chip with LOBAR from the same design is selected and sent to Evelyn Hu Group at Harvard University for the spin-coupling measurement. We wire bond the electrode and fit the device chip to a customized PCB board for measurement. Once the chip is wired-bonded, we select two modes from the measurement range in Figure 4.4 and re-measure the S_{21}. The result is shown in Figure 4.5.

The wire-bonded chip is then put on a confocal microscope optical setup for the spin measurement under room temperature and atmosphere. We drive the electrodes differentially, alternating the signal phase by 180° between neighboring Molybdenum strips, shown in Figure 4.6.

4.5 Strain-Spin Coupling Measurement

4.5.1 Silicon Vacancy in SiC

In previous works, we introduced NV centers in diamond and divacancies in SiC. In this chapter, we use Silicon Vacancy or SiV^- in 4H-SiC as the spin system for acoustic coupling. SiV^- is formed by a vacancy and a nearby Silicon atom in SiC lattice [77]. When it is negatively charged, it serves as a spin $S = 3/2$ system. The zero field splitting between

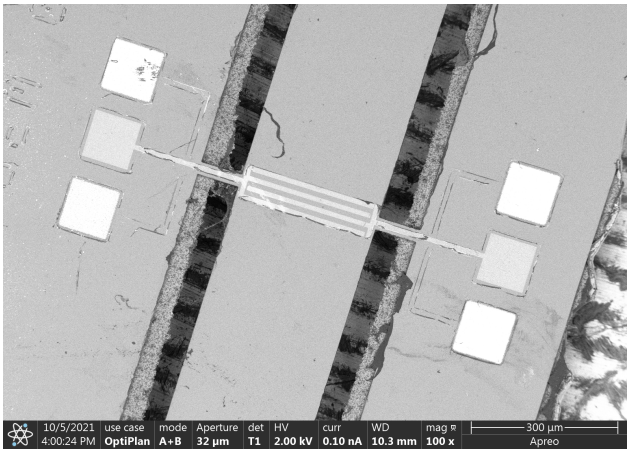

(a)

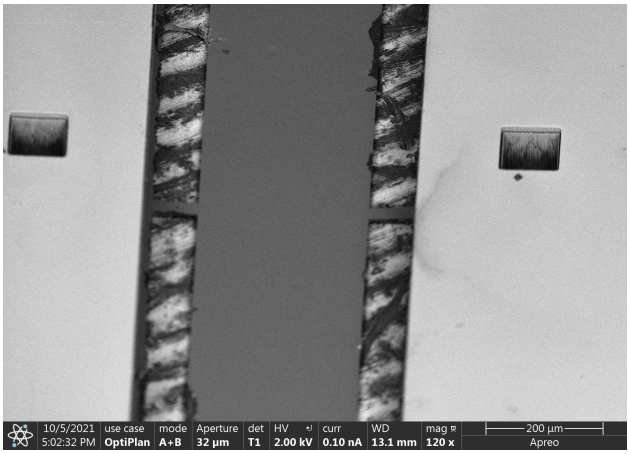

(b)

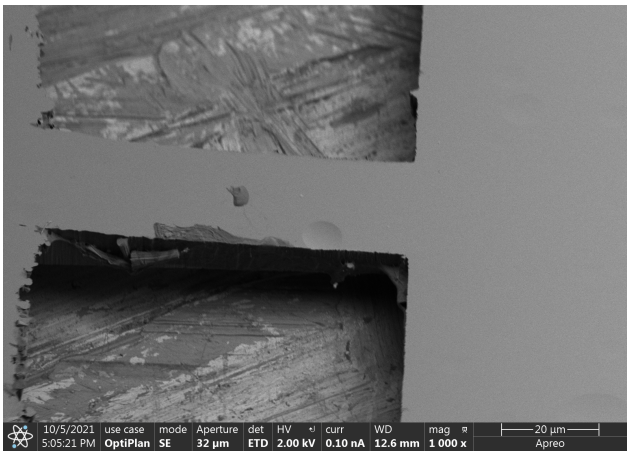

(c)

Figure 4.3. SEM images of the LOBAR device. (a) Frontside (b) Backside (c)Zoom-in image of the tether on the backside.

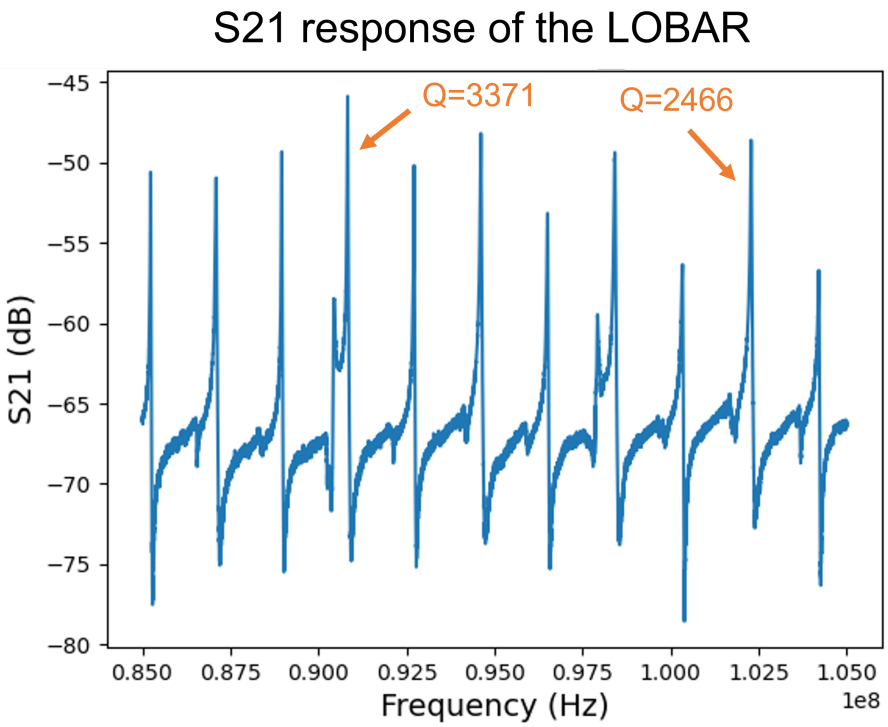

Figure 4.4. S_{21} transmission measurement of a LOBAR device A_0 mode and overtones around.

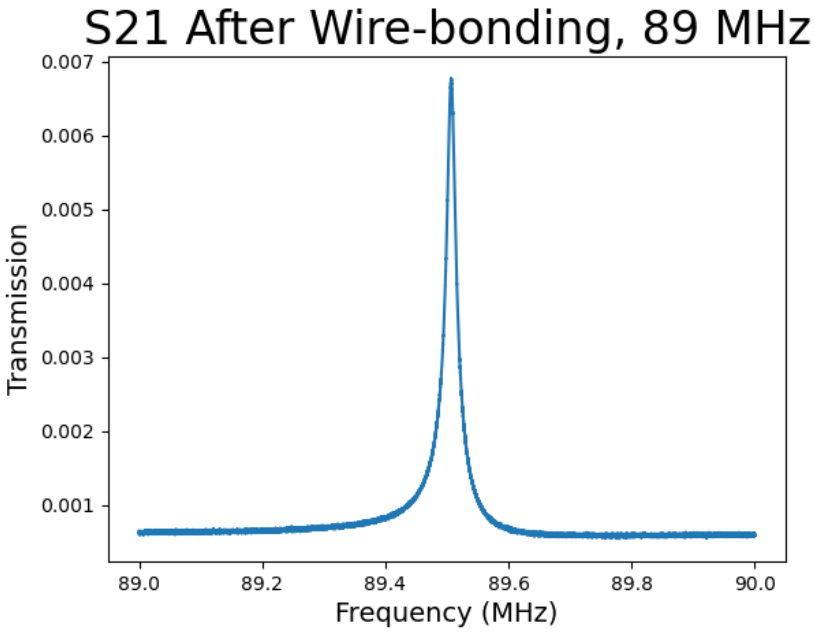

(a)

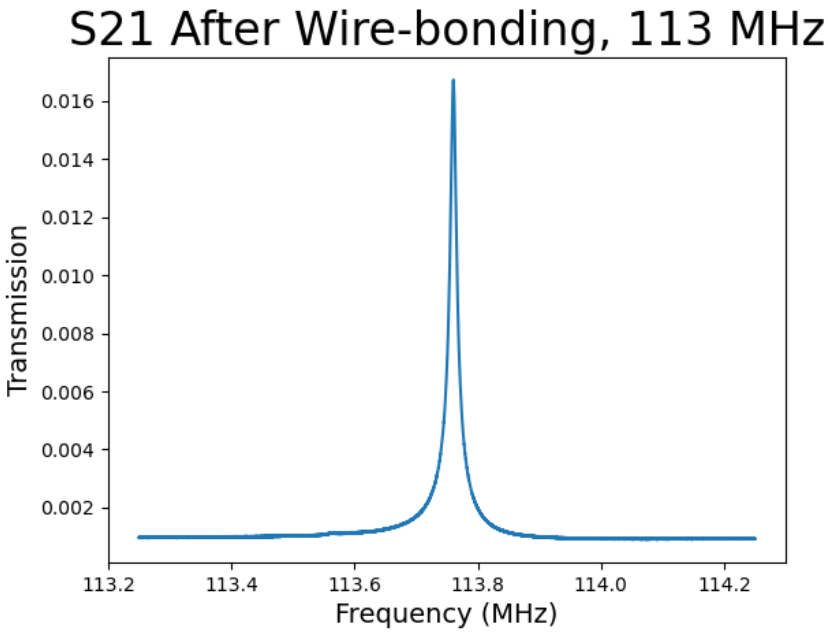

(b)

Figure 4.5. S_{21} transmission measurement of a LOBAR device after wire bonding. Q are (a) 3648 and (b) 6324 accordingly.

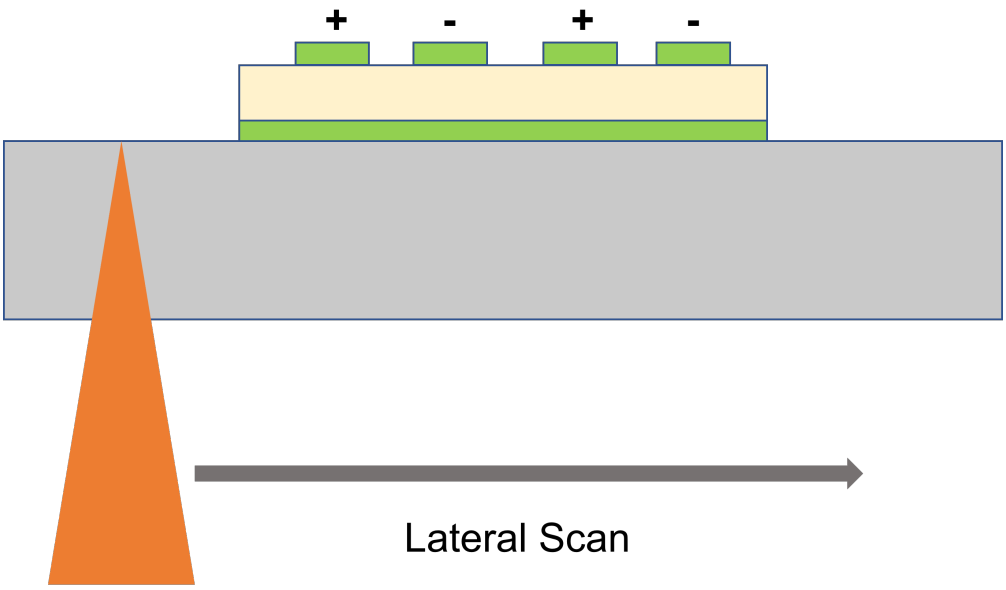

Figure 4.6. A scanning confocal microscope setup is used to measure the spin photoluminescence of the LOBAR. The scanning laser is put below the LOBAR bottom surface, so it will not be blocked in the top AlN transducer region. The electrodes are differentially driven for maximal coupling strength.

$m_s = \pm 3/2$ and $m_s = \pm 1/2$ states is $2D \approx 70MHz$[78]. The energy states are shown in Figure 4.7

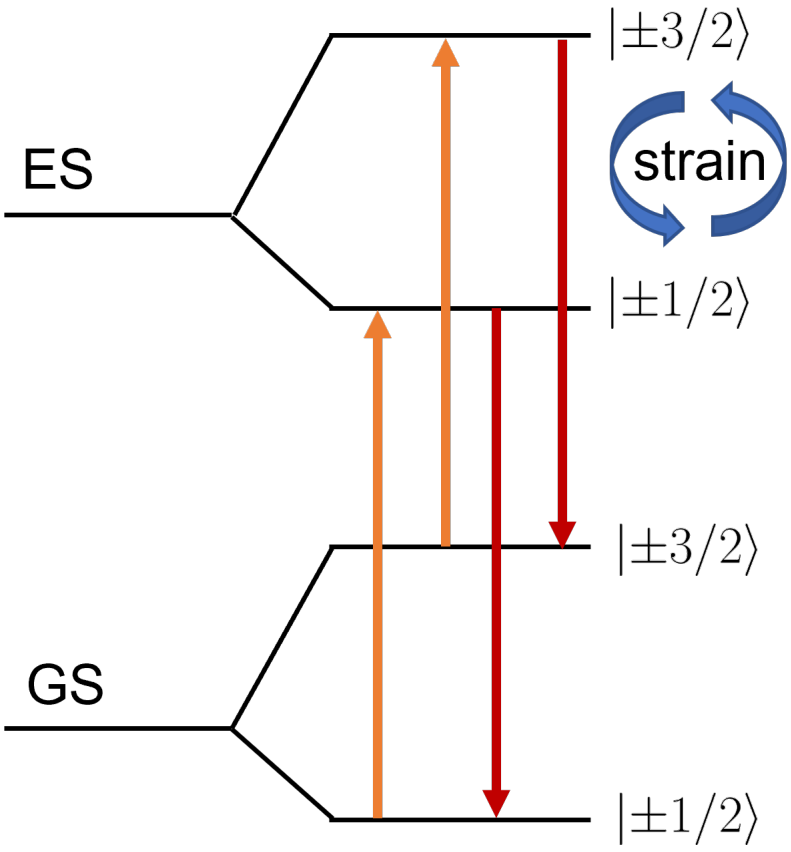

Figure 4.7. Energy state of SiV^- in 4H SiC.

SiV^- has been used in both $\Delta m_s = 2$ and $\Delta m_s = 1$ acoustically driven transitions [79]. For the simplicity of the experiment, in this work, we use the $\Delta m_s = 1$ transition as the method for strain mapping in the SiC by default.

4.5.2 Strain-spin Coupling Measurement

To measure the strain-spin coupling, we use so-called ODSAR (optically detected spin-acoustic resonance). We initialize the state at $|+1/2\rangle$ with laser. A permanent magnet is placed to create Zeeman splitting, and the LOBAR is driven to generate the state transition between $|+3/2\rangle$ and $|+1/2\rangle$ states. Then the population is read out optically through a single photon counter.

First, we fix the laser on a single point in the wing of the LOBAR, and shift the acoustic driving frequency to do a frequency scan. In Figure 4.8, the previously measured S_{21} is plotted with the spin's PL intensity. The PL data is smoothened with a Savitzky–Golay filter. The PL is linear with the local strain intensity that activates the state transition. The electrical transmission fits well with the PL peak, suggesting we are utilizing the mechanical resonance to enhance our driving coupling strength. Furthermore, this can be used as a way to characterize mechanical resonance including the Q under experimental condition without a network analyzer, or the need for electrical calibration.

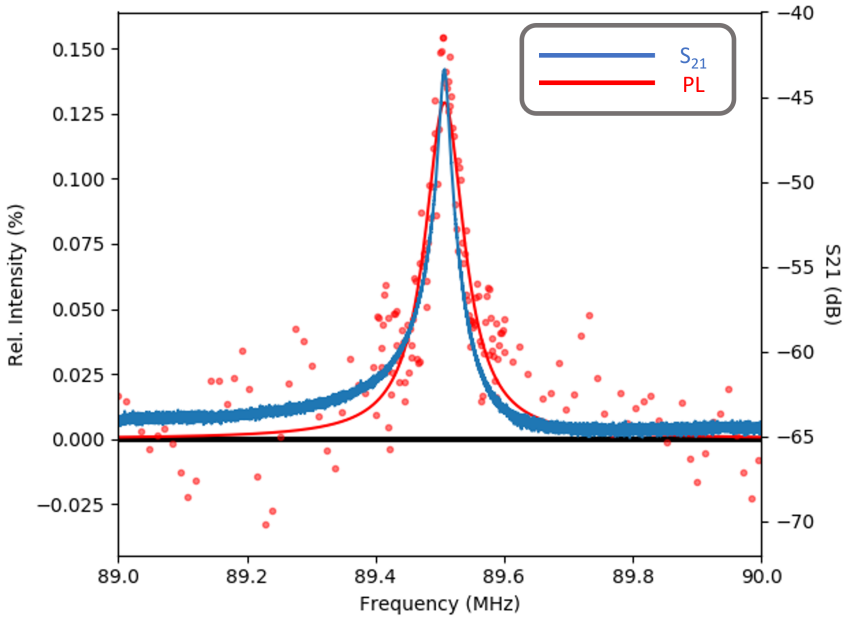

Figure 4.8. Frequency scan of ODSAR of SiV^- in the LOBAR wings plotted together with the previously measured S21 transmission with PNA.

To map out the strain distribution along the entire device, we then fix the driving frequency at the peak frequency in Figure 4.8 and scan the LOBAR in length direction in the center, as Figure 4.6 illustrates. The scan is done at 2 overtone frequencies for comparison. The result is shown in Figure 4.11. Due to the standing wave nature of the flexural mode, the PL intensity follows a sinusoidal distribution along the x axis, which matches the strain mode shape given by COMSOL in Figure 4.2.

To further compare the measured PL scanning data with simulation, I integrate the strain vertically at each x coordinate in the simulation mesh, as it is indicated in Figure 4.9. This is to simulate the PL collection process, where the pinhole is large enough that PL emission from the whole thickness of SiC is collected. The related code can be referred to Appendix B. The integrated data is then sorted by x axis and plotted together with PL data in Figure 4.10.

From the comparison, the peak distributions fit well in the simulation and the PL measurement. This indicates that the resonance mode we excited is in fact the Lamb wave flexural mode at the given frequency. The change of peak distance in the two plots characterizes the overtone nature of the modes, which can help identify the mode numbers, and find the maximal strain points. The AlN transducer stays around -40 to +40 um in the x axis. This affects the optical collection efficiency and causes the lowering of PL in this region. The spike at ±40 um is also from the boundary condition change from the reflective Molybdenum electrode to pure SiC surface. The minor position shift in the figure is due to the 2D COMSOL simulate unable to capture the real world boundary condition of the LOBAR. The difference in the height of the peaks is due to measurement error, mainly caused by the surface roughness and the arbitrary SiV^- distribution under natural condition.

Moving from 1D axis scan to 2D, we collect the PL intensity across the whole LOBAR near the center, plotted in Figure 4.12. The wave-like pattern of the flexural mode can be clearly seen from the figure. This has confirmed our ability to map to the strain distribution of an acoustic resonance in SiC, giving us an edge over conventional methods like LDV.

To further demonstrate our ability to utilize the strain-spin coupling, we measure the Rabi oscillation with the acoustic driving and traditional magnetic driving in Figure 4.13. The pulse sequence used for the measurement is shown in Figure 4.13a. We compared magnetic driven Rabi oscillation with mechanical driven ones on or off resonance frequency. The figure shows that the acoustic driving can be as strong as the magnetic one, while enables future application like mechanical quantum gate[**?**].

The acoustic driven Rabi is at 2 W power. We tuned the driving frequency slightly off the resonance frequency, plotted in the middle. The oscillation is only observable in the SiC right under the transducer, while the signal is indistinguishable in the wings. For the acoustic

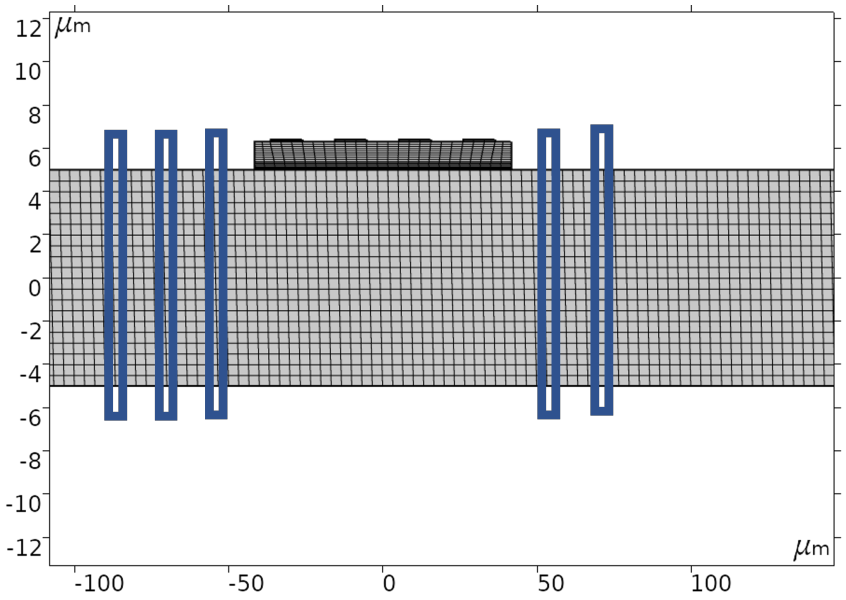

Figure 4.9. Integration of the COMSOL simulated strain distribution vertically. Each blue box contains a linear of mesh points at the corresponding x coordinate. The strain at each box is added together.

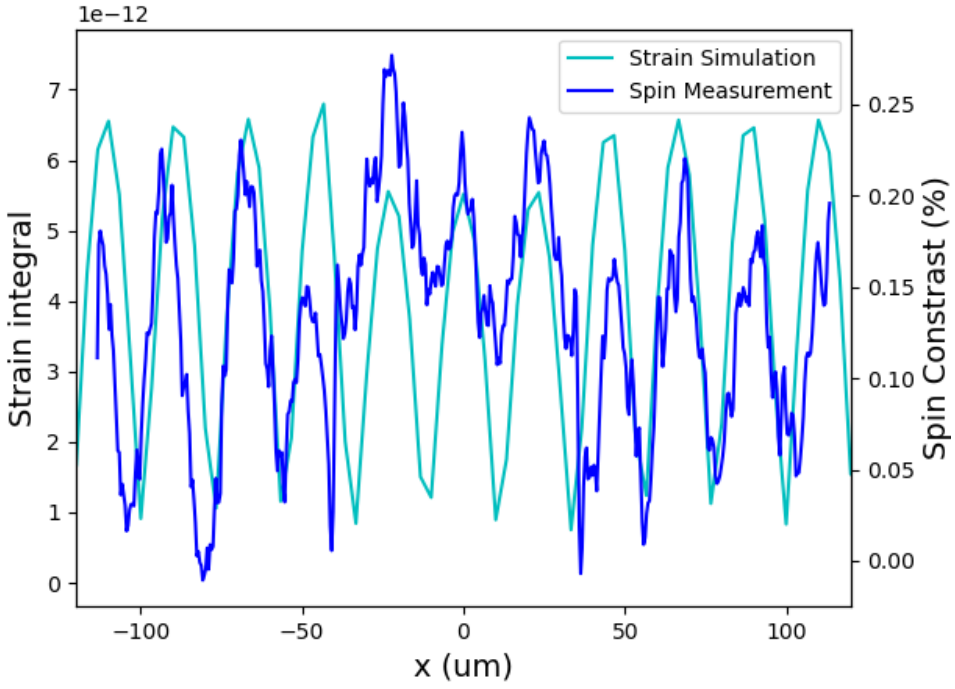

(a)

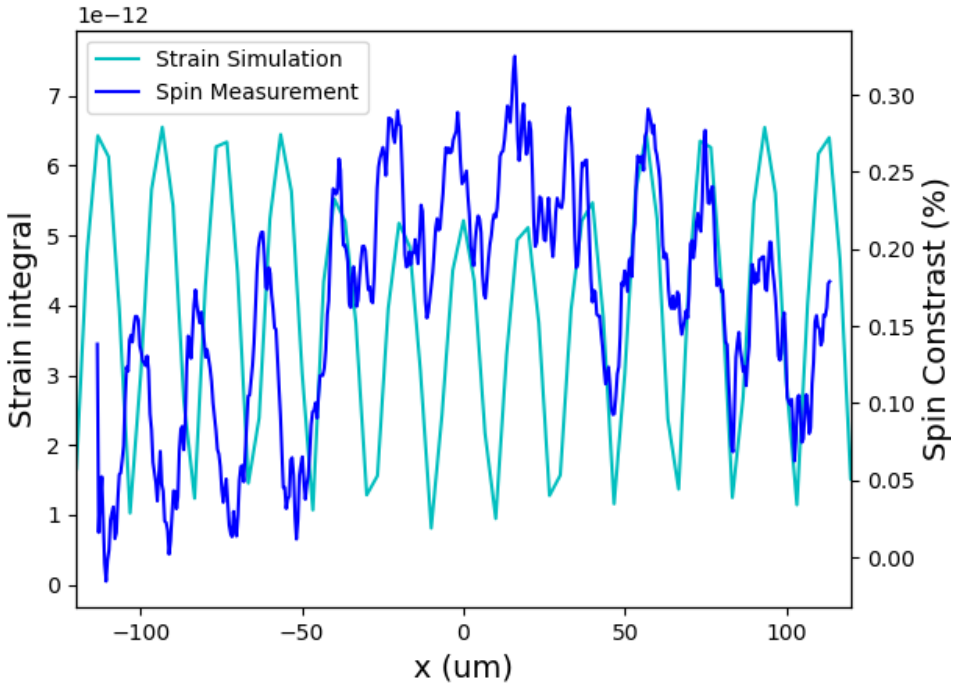

(b)

Figure 4.10. X-scan of PL shown together with the integrated COMSOL x axis strain data. The strain is in arbitrary unit. The PL is smoothened with a Savitzky–Golay filter. The transducer covered region is from -40 to 40 um in the x axis.

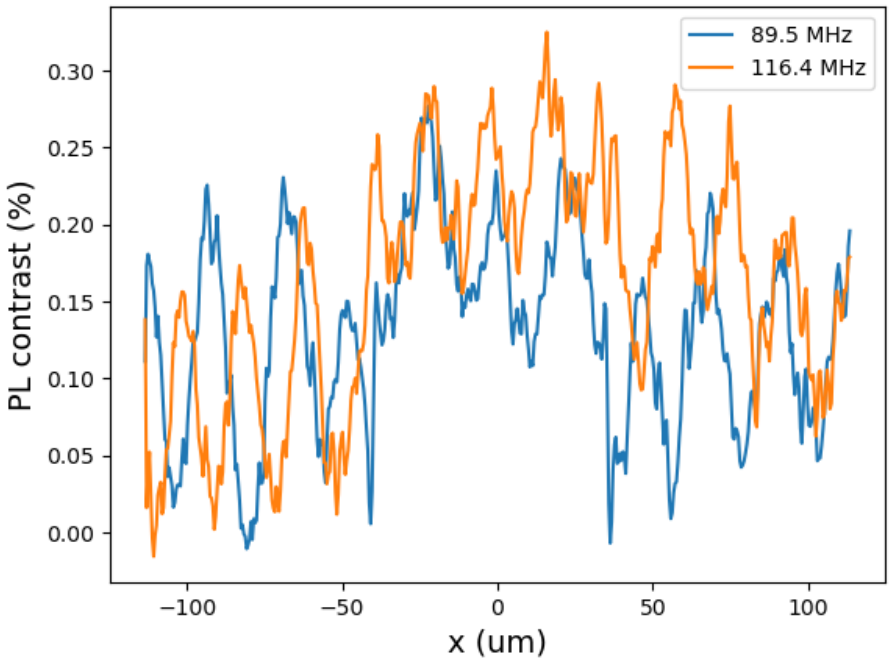

Figure 4.11. X-scan of the PL intensity for acoustic driving at 89 MHz and 113 MHz resonances.

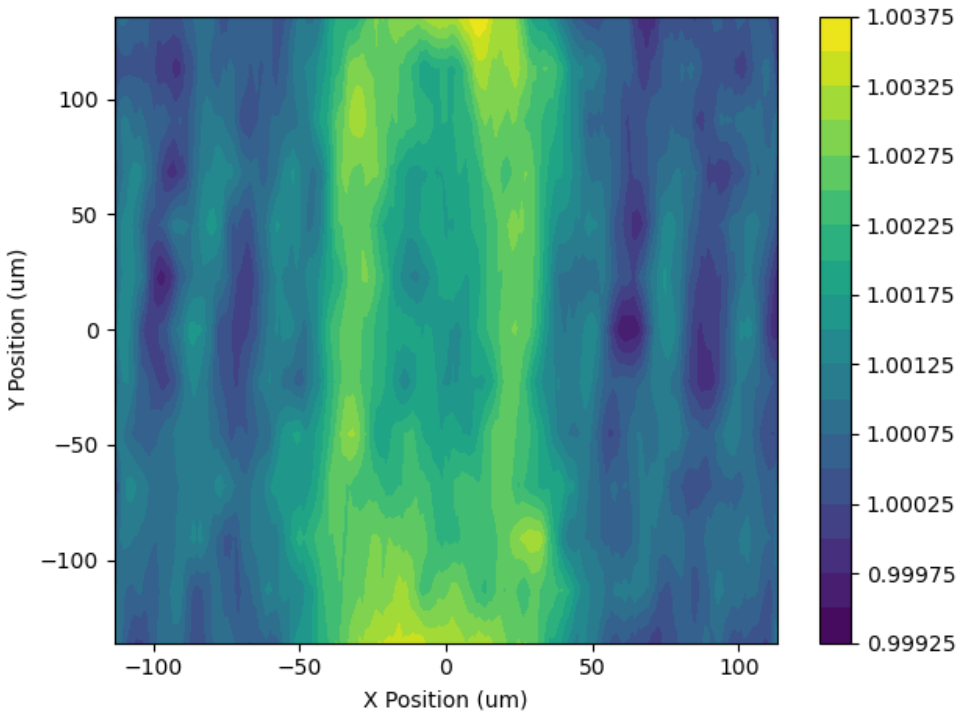

Figure 4.12. 2D scan of the PL intensity near the transducer region at 89 MHz mechanical resonance.

on-resonance driving, we measured the PL in the wing region. This demonstrate that the wing part of the LOBAR is only activated at resonance frequencies. This has enabled the potential for LOBAR to be used as a filter in quantum networks [80, 81].

In conclusion, we have demonstrated 2D strain mapping with SiV^- ODSAR in 4H-SiC, and measured Rabi oscillation with the acoustic resonance. Further work will be focused on 3D mapping of the mode, by using smaller pinhole and scan vertically. Also, the mechanical control of single spin in SiC will be of great interest with the use of LOBAR.

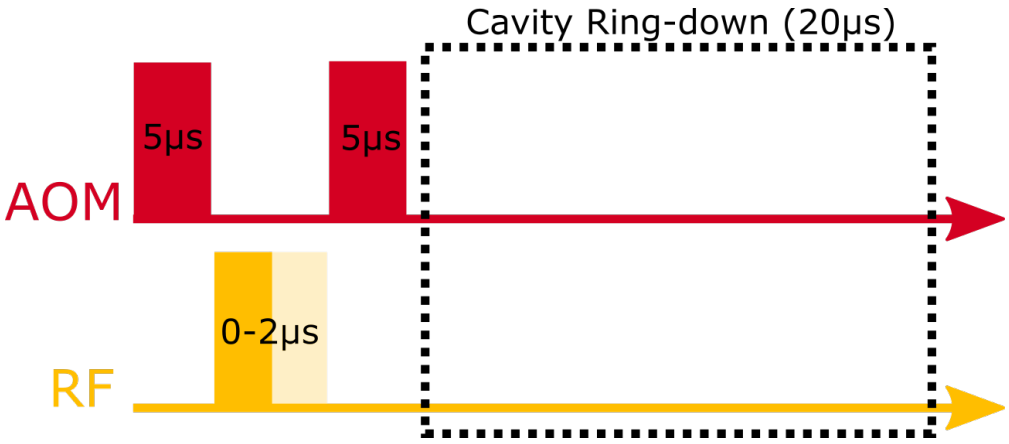

(a)

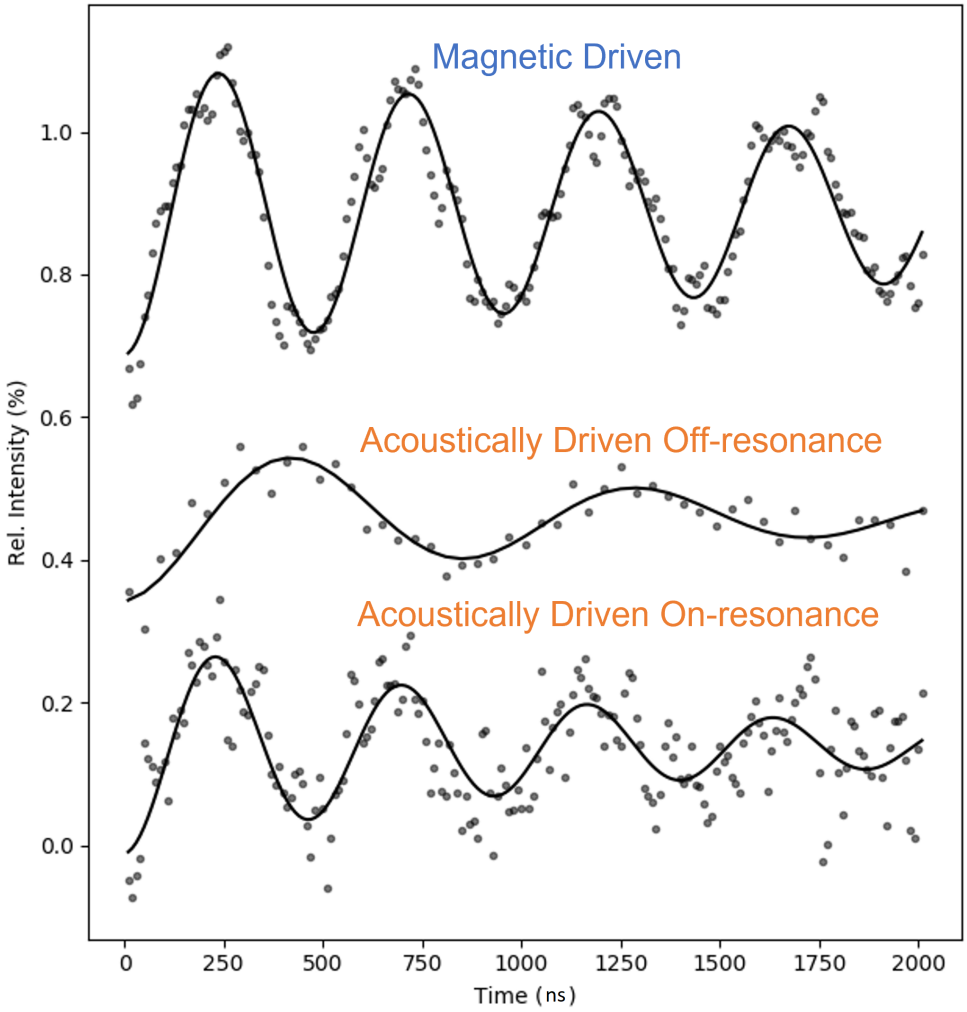

(b)

Figure 4.13. (a) Pulse sequence used in the acoustic Rabi oscillation measurement. (b) Magnetic driven, acoustic driven on and off resonance Rabi oscillations in comparison.

5. ACOUSTIC FRESNEL ZONE PLATE FOR ADDRESSING NEAR SURFACE SPIN

5.1 Introduction

Acoustic driving of the solid state spin centers with piezoelectric material like AlN and ZnO has been demonstrated by our group and others [53, 82]. In particular, the acoustic decoupling of NV center has been demostrated using a mechanical resonance [22], which greatly enhanced the T2* of a single NV qubit. Consequently, the sensitivity of a spin center can be enhanced by isolating it from the surrounding noise.

In prior examples, an acoustic wave has been introduced by a mechanical resonator, such as a SAW or BAW resonator. As discussed in Chapter 1, however, a resonator is not the only way to introduce a mechanical wave. A MEMS actuator without resonance behavior can also deliver acoustic energy into a system. One major drawback of a resonator is that the strain distribution inside the device must follow the mode shape. For example, in Fig. 5.1 (a), in a diamond HBAR resonator, the strain maximum points are at the nodes of the overtone mode shape. In those locations, as in NV2 in the figure, the spin can be addressed efficiently. However, for spins at other locations, only a proportion of the maximal strain can be used, whereas at the antinodes (maximum displacement points), the strain is near 0. Thus, spins such as NV1 and NV3 in the figure cannot be mechanically coupled efficiently.

However, the spins in the off-maximum locations can be highly important. When using NV as sensors for miniature scale sensing, an NV within several nanometers from the surface is desired, because proximity to the object increases the sensitivity for extremely small signals [83, 84]. However, these NVs experience greater noise from the electric and magnetic fields from surface spins and charges [85, 86]. The noise contributes to the coherence of the NV, thus compromising sensor capability. To counter this effect, researchers have applied surface treatment of the diamond [87] and used RF driving to suppress the surface noise spins [88]. The latter is shown in Fig. 5.1 (c).

In this chapter, I introduce a mechanical Fresnel zone plate (ZP) device (Fig. 5.1 (b)), that can focus the mechanical energy onto a small volume near the surface, to address the near-surface spins.

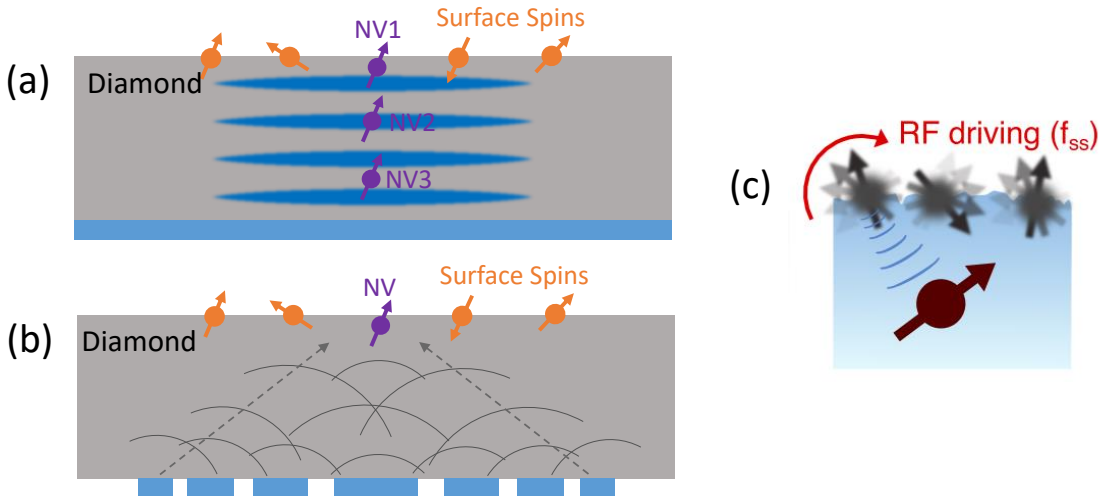

Figure 5.1. (a) Diamond NV in an HBAR. The blue mode shape shows the strain of the 2nd overtone mode. The NVs can be at different locations in the device, and those near the surface can be decoupled by interacting with surface spins. (b) Diamond Fresnel zone plate actuator. The acoustic energy (grey) is directed to the central near-surface NV. (c) RF addressing the surface spin the suppress the surface decoupling effect, from [88].

5.2 Principle

A Fresnel zone plate is a device with multiple concentric rings. Shown in Fig. 5.2 (a), the rings are either transparent (white) or opaque (black). An incoming wave hitting the black rings will diffract. By carefully designing the radius of each rings, the waves will interfere on the other side of the ZP and form a maximal strength point, which is the focus, similar to that of a convex lens. Each ring's radius, shown in (b), can be expressed as:

$$r_n = \sqrt{n\lambda f + \frac{1}{4}n^2\lambda^2} \tag{5.1}$$

here λ is the wavelength, f is the focal distance and n is the ring number.

ZPs, although originally invented for optics, have been widely used in other fields, including water waves (Fig. 5.2 (d)), X-ray [89], and microwave [90]. In Fig. 5.2 (c), a ZP with patterned top electrodes on one side the bulk silicon can excite a focused acoustic wave on a point on the other end, when the gap and width of each ring is properly chosen.

5.3 Design

The basic shape of the diamond ZP device is similar to that of an FBAR, except that the top AlN transducer is alternatively etched to the rings, instead of a one-piece film. As shown in Fig. 5.3 (b), a circular membrane is suspended in a bulk diamond chip, whereas the piezoelectric transducer rings are electrically connected by a normal strip line along the tether. An important observation is that, as shown in (c), owing to the symmetry of ZP, the ring sequence is arbitrary: the center of the pattern can be either be transparent or opaque, and the focusing effect remains the same. This aspect provides a large benefit over conventional bulk acoustic wave resonators in diamond, as shown in (a): If the central circle is rendered transparent by etching away the piezoelectric material on top, we can direct the excitation laser onto it, because it is now on the same side as the piezoelectric transducers. Because the wavelength of the laser light (532 nm) and bulk mechanical wave (several micrometers) are substantially different, the ZP shows little diffraction on the laser beam. In this setup, when NV is used for sensing applications, the other side of the device

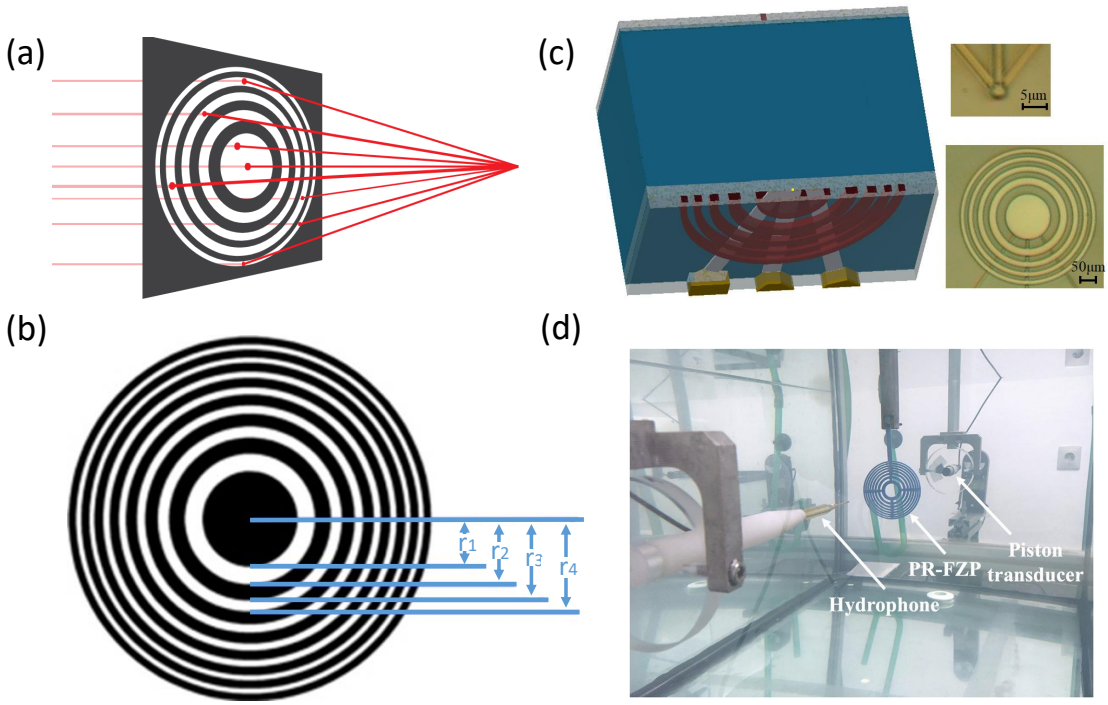

Figure 5.2. (a) A Fresnel zone plate acts like a convex lens, which can focus incoming waves to a focus point on the other side. (b) The radius of each ring in a ZP can be calculated. (c) ZP has been used in BAW for microfluid applications, figure from [91]. (d) ZP can be used to focused acoustic wave in fluids, figure from [92].

can be placed closer to the objects, given the absence of RF transmission structures. The potential of near-surface NV can now be exploited.

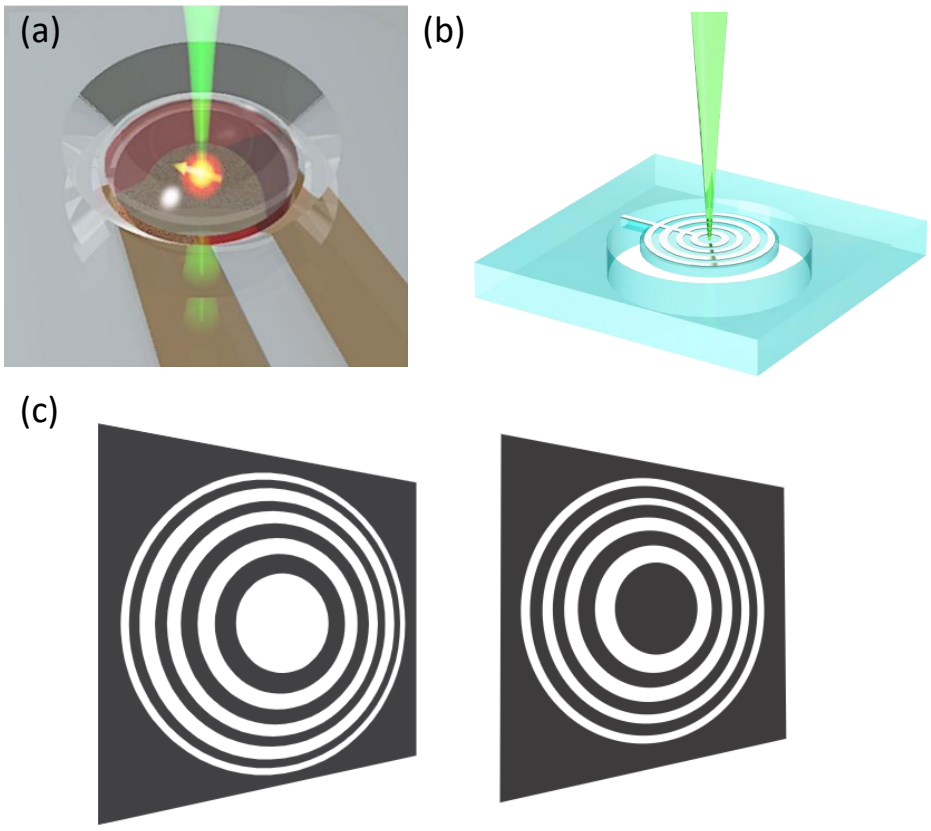

Figure 5.3. (a) A diamond SCHBAR device from [53]. The acoustic transducer has to be fabricated on the other side of the slab in order to allow the laser beam. (b) The proposed diamond ZP device can be excited by green laser on the same side as the acoustic transducers. (c) The sequence of the rings is arbitrary. The center can be either transparent or opaque with the same focusing ability.

The proposed fabrication flow is shown in Fig. 5.4. We first define the AlN transducer shape, then create a diamond thin membrane through backside DRIE, with a sapphire shadow mask. A SiO2 hardmask is then sputtered and defined, with which we can release the circular membrane through frontside DRIE. Finally, the oxide mask can be removed with a buffered oxide etch.

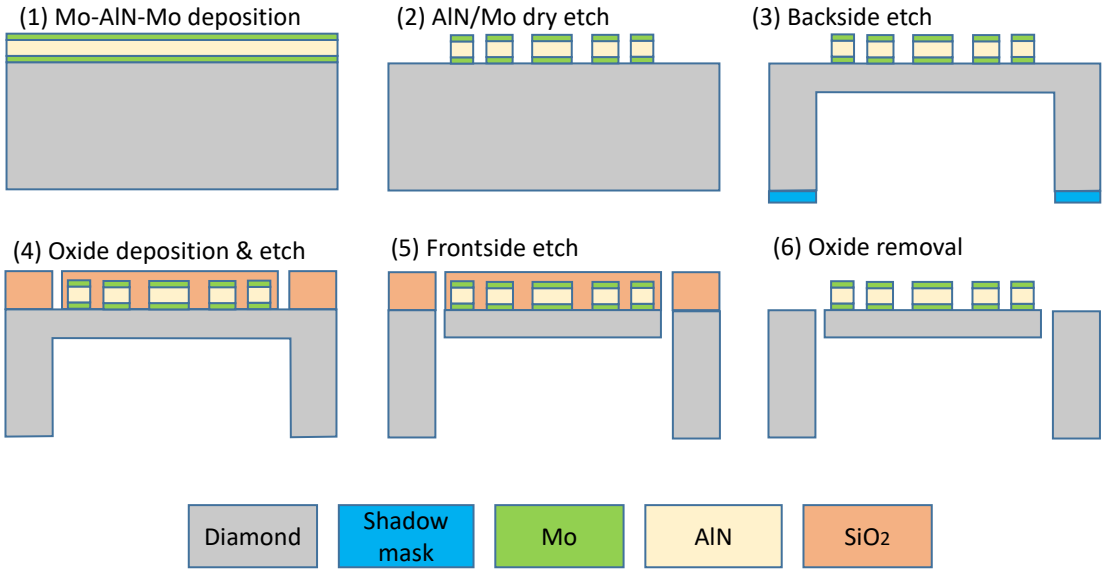

Figure 5.4. Proposed fabrication flow for the diamond ZP device.

5.4 Simulation

To understand the efficiency of the ZP design, a COMSOL model is built under 2D rotational symmetry condition. The diamond is 10 um thick, while the AlN is 1um thick under it. To compare it with an FBAR, we set the frequency for ZP at 3.6 GHz, which is the 2nd harmonic mode of the FBAR. 10 rings are used in the simulation, while the focal length is the thickness of the diamond. We also build an FBAR model with the same radius for an accurate comparison. The ZP mode shape is shown in Fig. 5.5 (a). It can be seen that the ZP transducer induces a strain strong point on the focus, which is the center of the top surface. At 1V electric input, the stress there is about 4 GPa, or 3.8×10^{-3} in strain. Fig. 5.5 (b) shows the maximum stress generated by a ZP and an FBAR. We can see that the stress generated by ZP is comparable to that from the FBAR, yet the latter cannot be reached at the surface focus point. Also, the stress of the FBAR quickly declines once the frequency moves away from the resonance, while the ZP can provide a broad-band enhancement even off-resonance.

Another interesting observation comes from the admittance plot of the transducers in Fig. 5.6. The plot for the FBAR shows a ordinary behavior, with a sharp peak at the resonance frequency. However, the curve for the ZP admittance is much flatter, which indicates that the Q of ZP maximum stress points are much lower than that of the FBAR. As it is discussed in Chapter 1 of the thesis, the Q factor indicates the amount of mechanical energy preserved in the system versus the loss. This can be explained by Termo-Elastic Dissipation (TED) loss from the system. The relation between mechanical and thermal (temperature) field in a solid can be expressed as [93]:

$$\begin{aligned} \rho \frac{\partial^2 u}{\partial t^2} &= E \frac{\partial^2 u}{\partial x^2} + \frac{\alpha E}{(1-2\nu)} \frac{\partial T}{\partial x} \\ C\rho \frac{\partial T}{\partial t} &= \kappa \frac{\partial^2 T}{\partial x^2} - \frac{\alpha E T_o}{(1-2\nu)} \frac{\partial^2 u}{\partial x \partial t} \end{aligned} \tag{5.2}$$

here u is the displacement field, T is the temperature field, E is the Young's modulus, κ is the thermal conductivity, α is the linear thermal expansion coefficient, T_0 is the average temperature of the system, C is the thermal capacity, ν is the Poisson's ratio, while ρ is the material density.

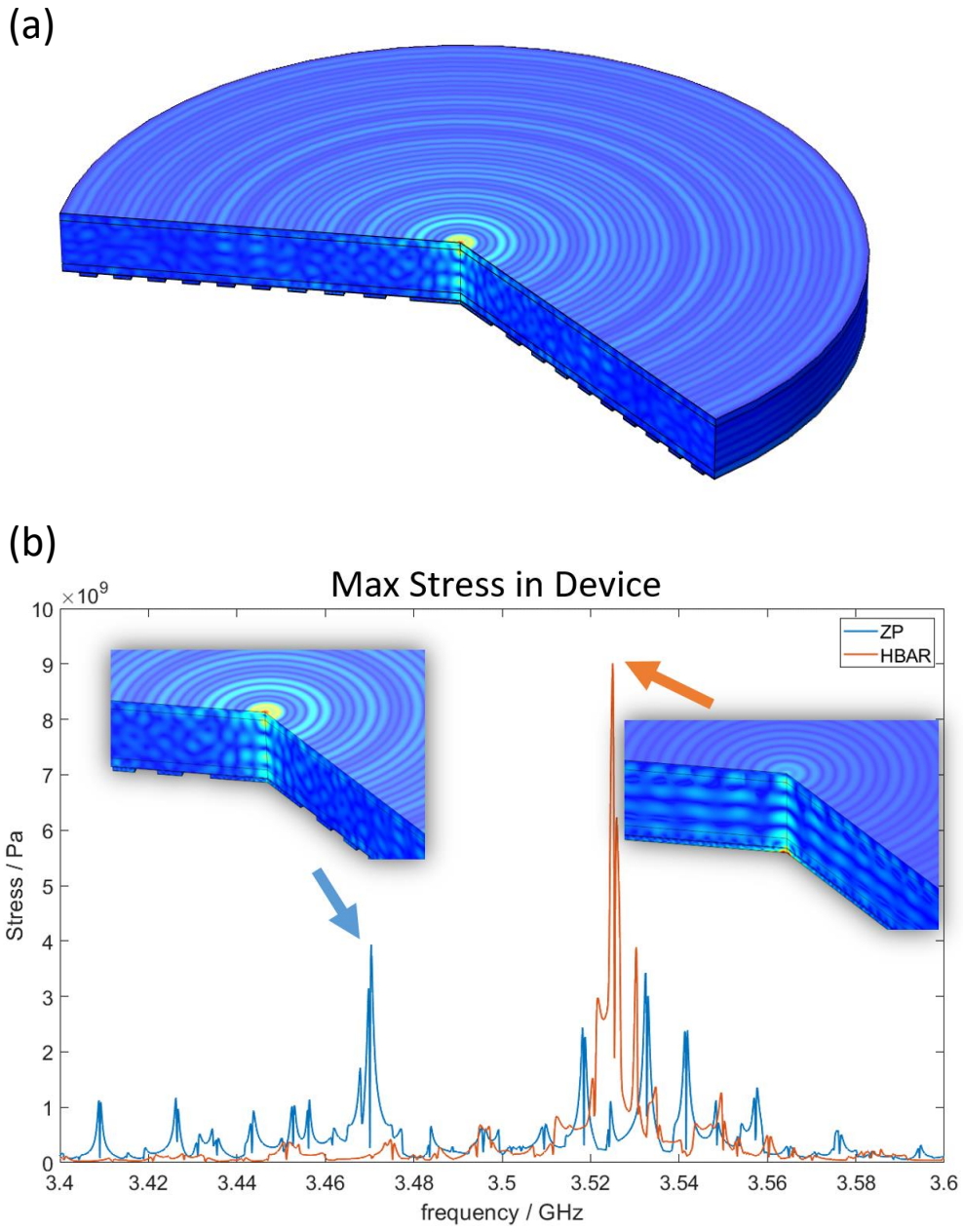

Figure 5.5. (a) Stress mode shape of the ZP at the optimal frequency. (b) Comparison between the maximum stress generated by ZP and an FBAR. The stress distribution is marked for each plot at its peak.

This equation set indicates that when a system is compressed or stretched mechanically, it will have a temperature increase or decrease. The uneven distribution of the temperature field will further cause heat flows in the system, which cause the mechanical energy to be dissipated as heat, thus lower the Q of the resonator. Since the ZP focuses the mechanical field onto a particular point, it generates a much steeper gradient than an FBAR, which causes a greater TED loss and a lower Q.

Since the purpose of the device is to introduce strain to an atom-scale spin, we realize that the traditional figure of merits for MEMS like Q no longer apply. In fact, a lower Q here is a side proof that the ZP device is working as intended by polarizing the strain distribution. This finding opens a new door to the spin-related MEMS design, as we are no longer limited to traditional MEMS resonators.

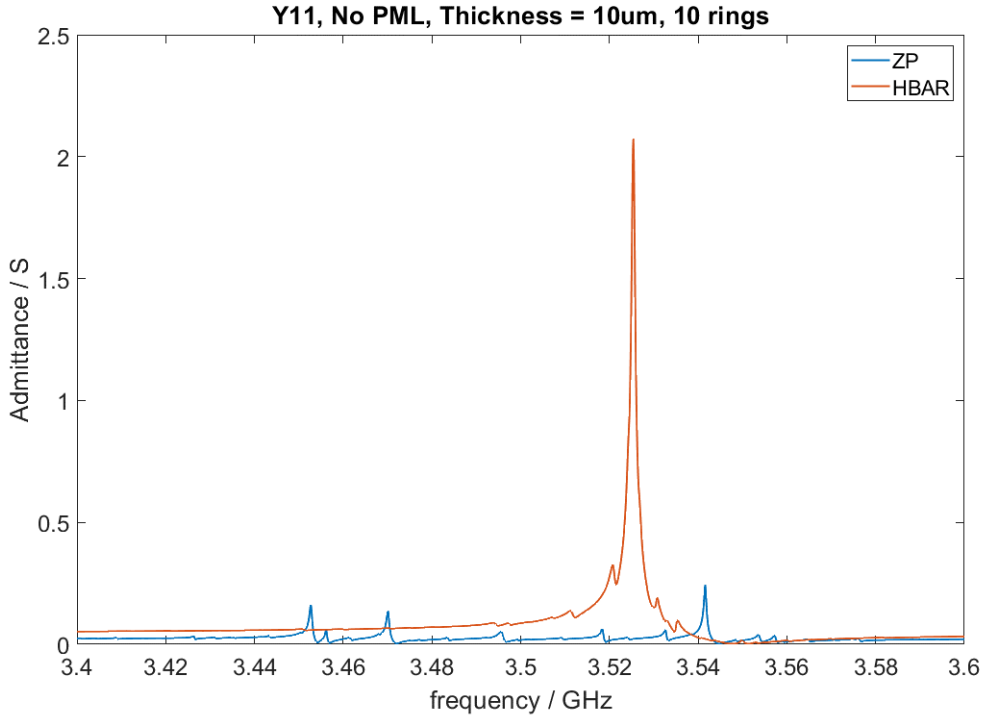

Figure 5.6. Admittance plot of the ZP and the FBAR.

5.5 Fabrication

Due to measurement setup availability, we first make ZP devices on Silicon Carbide platform, which we used for A_0 mode strain-spin coupling experiment. The process flow is identical to Section 3.3.

A microscopic picture of the ZP is shown in Figure 5.7. The top electrode is clearly defined with Mo dry etching.

SEM images of the ZP are shown in Figure 5.8. The frontside AlN etching left some residue micropillars on the exposed SiC surface. This will have to be improved in the future for a frontside optical access. The backside surface is mostly flat with a small amount of dimples.

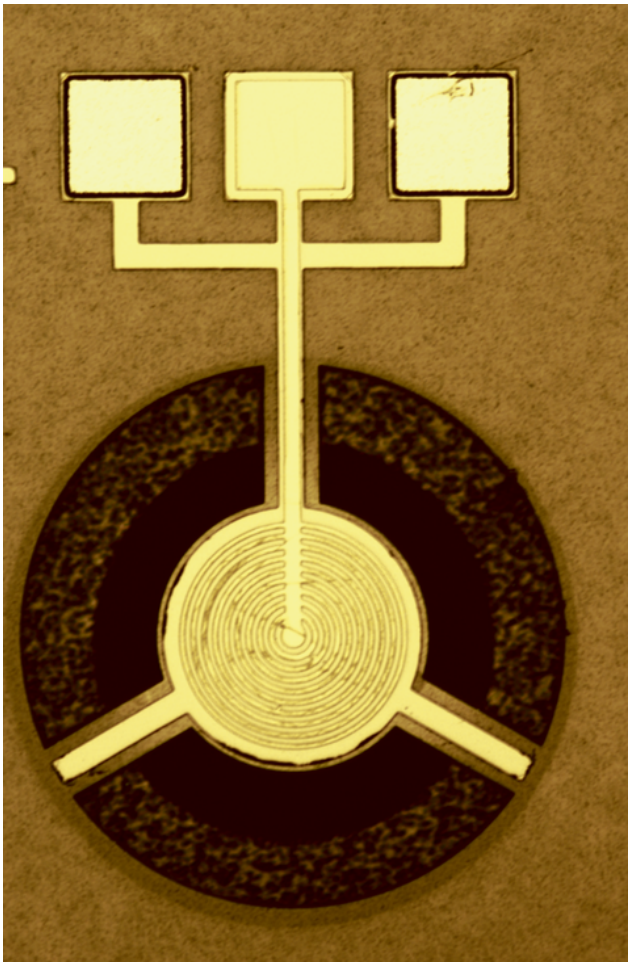

Figure 5.7. Microscopic picture of a ZP device.

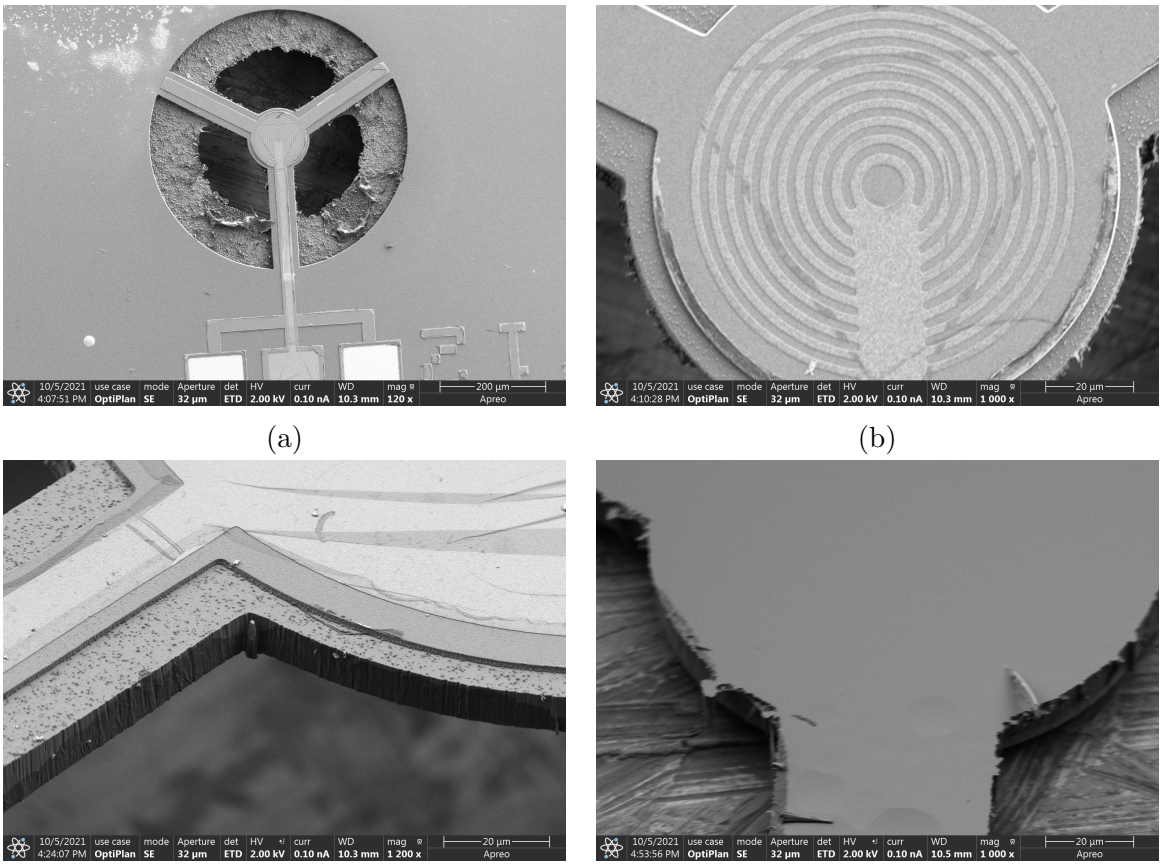

(a) (b)

(c) (d)

Figure 5.8. SEM images. (a) a ZP's frontside. (b) Zoom in picture of the top electrodes on a ZP device. (c) Tether of a ZP device. There are micropillars on the SiC surface, from the etching residue of AlN and Mo. (d) Backside of the ZP device.

5.6 Outlook

The best way to demonstrate that a ZP device is working is to compare it with an HBAR device with the same dimensions. As suggested in Fig. 5.5 (b), when excited out of resonance, the ZP generates more stress than the HBAR, which will be measured through the NV coupling strength.

To achieve even higher strain in the ZP system, geometric gain can be introduced in the system. As shown in Fig. 5.9 (a), owing to wave interference, the more rings present in a ZP, the stronger the focusing effect. The maximum radius that can be fabricated in the future will be explored to finalize the design.

In the future, we should be able to fabricate an array of ZPs in the same diamond chip, each with an NV center on the focus. The sensor array could then be used for large scale sensing applications, such as fingerprint sensing [94] and microfluidics [95]. The chip could be attached to objects as a whole, as shown in Fig. 5.9 (b), to allow proximate sensing.

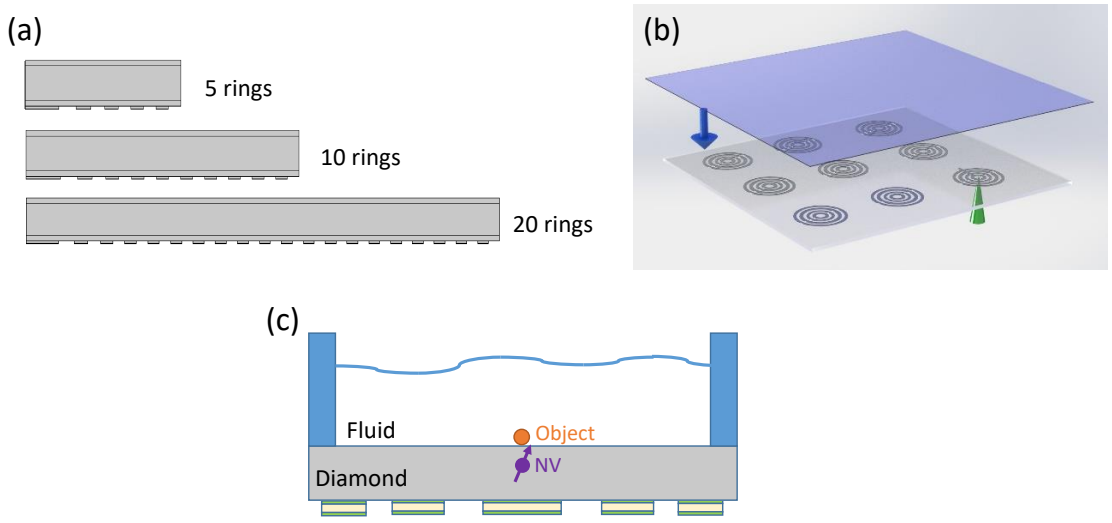

Figure 5.9. (a) The ring number of a ZP can be increased to enhance the focusing capability. (b) A ZP array can be made on the same diamond chip, at various working frequencies. (c) A possible application for the ZP in sample localization.

The design could be extended even further in acoustic tweezer applications. When NV is used for biological sensing, it is important to trap and fix the target particle, such as a protein

or a cell, near the diamond surface [96], in a process called localization. The conventional method involves building a microfluid channel on top and flowing the particle through it [97]. However, if a fluid environment, such as a water droplet containing a biological sample, is placed on an unreleased diamond ZP, as shown in Fig. 5.9 (c), the ZP will also create an acoustic field in the fluid. Because of the acoustic radiation force, the particle will be attracted to the maximal stress point, which is the focus of the ZP on the diamond surface. In this way, the particle can be trapped without excessive equipment.

REFERENCES

[1] G. M. Rebeiz, *RF MEMS: theory, design, and technology.* John Wiley & Sons, 2004.

[2] M. Tilli, M. Paulasto-Kröckel, M. Petzold, H. Theuss, T. Motooka, and V. Lindroos, *Handbook of silicon based MEMS materials and technologies.* Elsevier, 2010.

[3] G. Schiavone, M. P. Desmulliez, and A. J. Walton, "Integrated magnetic MEMS relays: Status of the technology," *Micromachines*, vol. 5, no. 3, pp. 622–653, 2014.

[4] H. Chandrahalim, S. A. Bhave, and S. Member, "PZT Transduction of High-Overtone Contour-," vol. 57, no. 9, pp. 2035–2041, 2010.

[5] J. A. Walraven, M. S. Baker, T. J. Headley, and R. A. Plass, "compliant thermo-mechanical MEMS actuators, LDRD# 52553." Sandia National Laboratories, Tech. Rep., 2004.

[6] Z. Qiu and W. Piyawattanametha, "MEMS actuators for optical microendoscopy," *Micromachines*, vol. 10, no. 2, 2019.

[7] D. Alsteens, H. E. Gaub, R. Newton, M. Pfreundschuh, C. Gerber, and D. J. Müller, "Atomic force microscopy-based characterization and design of biointerfaces," *Nature Reviews Materials*, vol. 2, no. 5, pp. 1–16, 2017. [Online]. Available: http://dx.doi.org/10.1038/natrevmats.2017.8

[8] H. Jin, J. Zhou, X. He, W. Wang, H. Guo, S. Dong, D. Wang, Y. Xu, J. Geng, J. K. Luo, and others, "Flexible surface acoustic wave resonators built on disposable plastic film for electronics and lab-on-a-chip applications," *Scientific reports*, vol. 3, p. 2140, 2013.

[9] M. Ziaei-Moayyed, S. D. Habermehl, D. W. Branch, P. J. Clews, and R. H. Olsson, "Silicon carbide lateral overtone bulk acoustic resonator with ultrahigh quality factor," *Proceedings of the IEEE International Conference on Micro Electro Mechanical Systems (MEMS)*, pp. 788–792, 2011.

[10] R. Abdolvand, B. Bahreyni, J. E. Lee, and F. Nabki, "Micromachined resonators: A review," *Micromachines*, vol. 7, no. 9, 2016.

[11] B. Bahreyni, *Fabrication & design of resonant microdevices*. William Andrew, 2008.

[12] V. Kaajakari, *Practical MEMS*. Small Gear Pub., 2009. [Online]. Available: https://books.google.com/books?id=PVGqngEACAAJ

[13] S. Mahon, "The 5G Effect on RF Filter Technologies," *IEEE Transactions on Semiconductor Manufacturing*, vol. 30, no. 4, pp. 494–499, 11 2017.

[14] G. L. Harris and I. I. service), *Properties of Silicon Carbide*, ser. EMIS datareviews series. INSPEC, Institution of Electrical Engineers, 1995. [Online]. Available: https://books.google.com/books?id=Yy_B8GzxNlgC

[15] A. L. Falk, P. V. Klimov, B. B. Buckley, V. Ivády, I. A. Abrikosov, G. Calusine, W. F. Koehl, Gali, and D. D. Awschalom, "Electrically and mechanically tunable electron spins in silicon carbide color centers," *Physical Review Letters*, vol. 112, no. 18, pp. 1–6, 2014.

[16] S. J. Whiteley, "SPIN-PHONON INTERACTIONS WITH DEFECTS IN SILICON CARBIDE A DISSERTATION SUBMITTED TO THE FACULTY OF THE DIVISION OF THE PHYSICAL SCIENCES IN CANDIDACY FOR THE DEGREE OF DOCTOR OF PHILOSOPHY DEPARTMENT OF PHYSICS BY SAMUEL JAMES WHITELEY CHICAGO , ILLINOIS," Ph.D. dissertation, University of Chicago, 2019.

[17] A. L. Falk, P. V. Klimov, B. B. Buckley, V. Ivády, I. A. Abrikosov, G. Calusine, W. F. Koehl, Gali, and D. D. Awschalom, "Electrically and mechanically tunable electron spins in silicon carbide color centers," *Physical review letters*, vol. 112, no. 18, p. 187601, 2014.

[18] E. R. Macquarrie, T. A. Gosavi, N. R. Jungwirth, S. A. Bhave, and G. D. Fuchs, "Mechanical spin control of nitrogen-vacancy centers in diamond," *Physical Review Letters*, vol. 111, no. 22, pp. 1–5, 2013.

[19] A. Hernández-M\'\inguez, A. V. Poshakinskiy, M. Hollenbach, P. V. Santos, and G. V. Astakhov, "Anisotropic Spin-Acoustic Resonance in Silicon Carbide at Room Temperature," *Phys. Rev. Lett.*, vol. 125, no. 10, p. 107702, 9 2020. [Online]. Available: https://link.aps.org/doi/10.1103/PhysRevLett.125.107702

[20] P. Kehayias, M. J. Turner, R. Trubko, J. M. Schloss, C. A. Hart, M. Wesson, D. R. Glenn, and R. L. Walsworth, "Imaging crystal stress in diamond using ensembles of nitrogen-vacancy centers," *Phys. Rev. B*, vol. 100, no. 17, p. 174103, 11 2019. [Online]. Available: https://link.aps.org/doi/10.1103/PhysRevB.100.174103

[21] S. J. Whiteley, G. Wolfowicz, C. P. Anderson, A. Bourassa, H. Ma, M. Ye, G. Koolstra, K. J. Satzinger, M. V. Holt, F. J. Heremans, A. N. Cleland, D. I. Schuster, G. Galli, and D. D. Awschalom, "Probing spin-phonon interactions in silicon carbide with Gaussian acoustics," 2018. [Online]. Available: http://arxiv.org/abs/1804.10996

[22] E. R. Macquarrie, T. A. Gosavi, S. A. Bhave, and G. D. Fuchs, "Continuous dynamical decoupling of a single diamond nitrogen-vacancy center spin with a mechanical resonator," *Physical Review B - Condensed Matter and Materials Physics*, vol. 92, no. 22, pp. 1–13, 2015.

[23] S. Ghaffari, S. A. Chandorkar, S. Wang, E. J. Ng, C. H. Ahn, V. Hong, Y. Yang, and T. W. Kenny, "Quantum limit of quality factor in silicon micro and nano mechanical resonators," *Scientific Reports*, vol. 3, pp. 1–7, 2013.

[24] R. Maboudian, C. Carraro, D. G. Senesky, and C. S. Roper, "Advances in silicon carbide science and technology at the micro-and nanoscales," *Journal of Vacuum Science & Technology A: Vacuum, Surfaces, and Films*, vol. 31, no. 5, p. 50805, 2013.

[25] L. x. Chen, H. Liu, S. Liu, C. m. Li, Y. c. Wang, K. An, C. y. Hua, J. l. Liu, J. j. Wei, L. f. Hei, and F. x. Lv, "Growth of high quality AlN films on CVD diamond by RF reactive magnetron sputtering," *Applied Surface Science*, vol. 431, pp. 152–159, 2018. [Online]. Available: https://doi.org/10.1016/j.apsusc.2017.09.036

[26] Q. Yu, T. Ai, L. Jiang, Y. Zhang, C. Li, and X. Yuan, "Efficient energy transfer in Eu-doped ZnO on diamond film," *RSC Advances*, vol. 4, no. 96, pp. 53 946–53 949, 2014.

[27] K. Jensen, P. Kehayias, and D. Budker, "Magnetometry with nitrogen-vacancy centers in diamond," *Smart Sensors, Measurement and Instrumentation*, vol. 19, no. September, pp. 553–576, 2017.

[28] Wikipedia contributors, "Bloch sphere — {Wikipedia}{,} The Free Encyclopedia," 2020. [Online]. Available: https://en.wikipedia.org/w/index.php?title=Bloch_sphere&oldid=987502807

[29] H. Y. Chen, S. A. Bhave, and G. D. Fuchs, "Acoustically Driving the Single-Quantum Spin Transition of Diamond Nitrogen-Vacancy Centers," *Physical Review Applied*, vol. 13, no. 5, p. 1, 2020. [Online]. Available: https://doi.org/10.1103/PhysRevApplied.13.054068

[30] G. Mariani, S. Nomoto, S. Kashiwaya, and S. Nomura, "System for the remote control and imaging of MW fields for spin manipulation in NV centers in diamond," *Scientific Reports*, vol. 10, no. 1, p. 4813, 2020. [Online]. Available: https://doi.org/10.1038/s41598-020-61669-w

[31] S. Maity, L. Shao, S. Bogdanović, S. Meesala, Y. I. Sohn, N. Sinclair, B. Pingault, M. Chalupnik, C. Chia, L. Zheng, K. Lai, and M. Lončar, "Coherent acoustic control of a single silicon vacancy spin in diamond," *Nature Communications*, vol. 11, no. 1, pp. 1–6, 2020.

[32] B. Pingault, D.-D. Jarausch, C. Hepp, L. Klintberg, J. N. Becker, M. Markham, C. Becher, and M. Atatüre, "Coherent control of the silicon-vacancy spin in diamond," *Nature Communications*, vol. 8, no. 1, p. 15579, 2017. [Online]. Available: https://doi.org/10.1038/ncomms15579

[33] S. Maity, B. Pingault, G. Joe, M. Chalupnik, D. Assump\ifmmode \mbox\cc\else ç\fião, E. Cornell, L. Shao, and M. Lon\ifmmode \checkc\else č\fiar,

"Mechanical Control of a Single Nuclear Spin," *Phys. Rev. X*, vol. 12, no. 1, p. 11056, 3 2022. [Online]. Available: https://link.aps.org/doi/10.1103/PhysRevX.12.011056

[34] M. H. Metsch, K. Senkalla, B. Tratzmiller, J. Scheuer, M. Kern, J. Achard, A. Tallaire, M. B. Plenio, P. Siyushev, and F. Jelezko, "Initialization and Readout of Nuclear Spins via a Negatively Charged Silicon-Vacancy Center in Diamond," *Phys. Rev. Lett.*, vol. 122, no. 19, p. 190503, 5 2019. [Online]. Available: https://link.aps.org/doi/10.1103/PhysRevLett.122.190503

[35] E. R. MacQuarrie, T. A. Gosavi, A. M. Moehle, N. R. Jungwirth, S. A. Bhave, and G. D. Fuchs, "Coherent control of a nitrogen-vacancy center spin ensemble with a diamond mechanical resonator," *Optica*, vol. 2, no. 3, pp. 233–238, 3 2015. [Online]. Available: http://www.osapublishing.org/optica/abstract.cfm?URI=optica-2-3-233

[36] W. Jiang, R. Zhang, B. Jiang, and W. Cao, "Characterization of piezoelectric materials with large piezoelectric and electromechanical coupling coefficients," *Ultrasonics*, vol. 41, no. 2, pp. 55–63, 2003.

[37] H. Bardaweel, O. Al Hattamleh, R. Richards, D. Bahr, and C. Richards, "A Comparison of piezoelectric materials for MEMS power generation," in *The sixth International Workshop on Micro and Nanotechnology for power generation and energy conversion applications*, 2006, pp. 207–210.

[38] R. Tabrizian, M. Rais-Zadeh, and F. Ayazi, "Effect of phonon interactions on limiting the f.Q product of micromechanical resonators," *TRANSDUCERS 2009 - 15th International Conference on Solid-State Sensors, Actuators and Microsystems*, no. 3, pp. 2131–2134, 2009.

[39] T. A. Gosavi, E. R. MacQuarrie, G. D. Fuchs, and S. A. Bhave, "HBAR as a high frequency high stress generator," *2015 IEEE International Ultrasonics Symposium (IUS)*, pp. 1–4, 2015. [Online]. Available: http://ieeexplore.ieee.org/document/7329069/

[40] T. Ohshima, A. Gali, T. Umeda, E. Janzén, M. Bockstedte, J. ul Hassan, N. Morishita, N. T. Son, J. Isoya, H. Itoh, and P. Carlsson, "Divacancy in 4H-SiC," *Physical Review Letters*, vol. 96, no. 5, pp. 8–11, 2006.

[41] S. J. Whiteley, G. Wolfowicz, C. P. Anderson, A. Bourassa, H. Ma, M. Ye, G. Koolstra, K. J. Satzinger, M. V. Holt, F. J. Heremans, A. N. Cleland, D. I. Schuster, G. Galli, and D. D. Awschalom, "Spin–phonon interactions in silicon carbide addressed by Gaussian acoustics," *Nature Physics*, vol. 15, no. 5, pp. 490–495, 2019.

[42] P.-l. Yu, N. Opondo, S. Dai, B. Jiang, D. T. Morisette, and S. A. Bhave, "Single Crystalline 4H-SiC Membrane Resonators," in *2018 IEEE International Frequency Control Symposium (IFCS)*, 2018, pp. 1–5.

[43] S. D. Ko, B. Hamelin, J. Yang, and F. Ayazi, "High-Q monocrystalline silicon carbide disk resonators fabricated using drie of thick SiC-on-insulator substrates," *Proceedings of the IEEE International Conference on Micro Electro Mechanical Systems (MEMS)*, vol. 2018-Janua, no. January, pp. 996–999, 2018.

[44] B. Hamelin, J. Yang, A. Daruwalla, H. Wen, and F. Ayazi, "Monocrystalline Silicon Carbide Disk Resonators on Phononic Crystals with Ultra-Low Dissipation Bulk Acoustic Wave Modes," *Scientific Reports*, vol. 9, no. 1, pp. 1–8, 2019. [Online]. Available: http://dx.doi.org/10.1038/s41598-019-54278-9

[45] H. Fujita, J.-P. Gouy, A. Tixier, M. Mita, and Y. Mita, "Embedded-mask-methods for mm-scale multi-layer vertical/slanted Si structures," in *Proceedings IEEE Thirteenth Annual International Conference on Micro Electro Mechanical Systems*, 2000, pp. 300–305.

[46] V. Milanović, M. Last, and K. S. J. Pister, "Torsional Micromirrors with Lateral Actuators," *Transducers '01 Eurosensors XV*, pp. 1270–1273, 2013.

[47] K. M. Dowling, A. J. Suria, A. Shankar, C. A. Chapin, and D. G. Senesky, "Multilayer etch masks for 3-dimensional fabrication of robust silicon carbide microstructures,"

Proceedings of the IEEE International Conference on Micro Electro Mechanical Systems (MEMS), vol. 2015-Febru, no. February, pp. 284–287, 2015.

[48] L. E. Luna, K. D. Hobart, M. J. Tadjer, R. L. Myers-Ward, T. J. Anderson, and F. J. Kub, "{SiC} Wafer Bonding and Deep Reactive Ion Etching Towards High-Aspect Ratio {SiC} {MEMS} Fabrication," *{ECS} Transactions*, vol. 86, no. 5, pp. 105–110, 7 2018. [Online]. Available: https://doi.org/10.1149%2F08605.0105ecst

[49] G. Wolfowicz, C. P. Anderson, A. L. Yeats, S. J. Whiteley, J. Niklas, O. G. Poluektov, F. J. Heremans, and D. D. Awschalom, "Optical charge state control of spin defects in 4H-SiC," *Nature Communications*, vol. 8, no. 1, p. 1876, 2017. [Online]. Available: https://doi.org/10.1038/s41467-017-01993-4

[50] S. A. Bhave, Di Gao, R. Maboudian, and R. T. Howe, "Fully-differential poly-SiC Lame mode resonator and checkerboard filter," in *18th IEEE International Conference on Micro Electro Mechanical Systems, 2005. MEMS 2005.*, 1 2005, pp. 223–226.

[51] T. Funaki, J. C. Balda, J. Junghans, A. S. Kashyap, H. A. Mantooth, F. Barlow, T. Kimoto, and T. Hikihara, "Power Conversion With SiC Devices at Extremely High Ambient Temperatures," *IEEE Transactions on Power Electronics*, vol. 22, no. 4, pp. 1321–1329, 7 2007.

[52] B. Jiang, N. Opondo, G. Wolfowicz, P.-l. Yu, D. D. Awschalom, and S. A. Bhave, "SiC CANTILEVERS FOR GENERATING UNIAXIAL STRESS OxideMEMS Lab , Purdue University , West Lafayette , IN , USA and Institute of Molecular Engineering , University of Chicago , Chicago , IL , USA," *2019 20th International Conference on Solid-State Sensors, Actuators and Microsystems & Eurosensors XXXIII (TRANSDUCERS & EUROSENSORS XXXIII)*, no. June, pp. 1655–1658, 2019.

[53] H. Chen, N. F. Opondo, B. Jiang, E. R. Macquarrie, R. S. Daveau, S. A. Bhave, and G. D. Fuchs, "Engineering Electron-Phonon Coupling of Quantum Defects to a Semiconfocal Acoustic Resonator," *Nano Letters*, vol. 19, no. 10, pp. 7021–7027, 2019.

[54] N.-K. K. Songbin Gong and G. Piazza, "GHz High-Q Lateral Overmoded Bulk Acoustic-Wave Resonators Using Epitaxial SiC Thin Film," *Journal of Microelectromechanical Systems*, vol. 21, no. 2, pp. 253–255, 2012.

[55] C. A. Zorman, W. F. Koehl, D. D. Awschalom, P. X.-L. Feng, G. Calusine, A. Politi, A. L. Falk, V. V. Dobrovitski, and B. B. Buckley, "Polytype control of spin qubits in silicon carbide," *Nature Communications*, vol. 4, no. 1, pp. 1–7, 2013. [Online]. Available: http://dx.doi.org/10.1038/ncomms2854

[56] Y. Li, P. Liu, and Z. Zhang, "Near-Zero Dielectric Loss Millimeter-Wave Leaky-Wave Antenna Using Silicon MEMS Process," in *2018 International Symposium on Antennas and Propagation (ISAP)*, 10 2018, pp. 1–2.

[57] M. J. Ahamed, D. Senkal, and A. M. Shkel, "Effect of annealing on mechanical quality factor of fused quartz hemispherical resonator," in *2014 International Symposium on Inertial Sensors and Systems (ISISS)*, 2 2014, pp. 1–4.

[58] H. Zhu and J. E. Lee, "Design of phononic crystal tethers for frequency-selective quality factor enhancement in AlN piezoelectric-on-silicon resonators," *Procedia Engineering*, vol. 120, pp. 516–519, 2015. [Online]. Available: http://dx.doi.org/10.1016/j.proeng.2015.08.689

[59] M. Pandey, R. B. Reichenbach, A. T. Zehnder, A. Lal, and H. G. Craighead, "Reducing anchor loss in MEMS resonators using mesa isolation," *Journal of Microelectromechanical Systems*, vol. 18, no. 4, pp. 836–844, 2009.

[60] S. Gong, N. Kuo, and G. Piazza, "Geometry optimization for quality factor enhancement in SiC-based lateral overmoded bulk acoustic resonators," in *2012 IEEE 25th International Conference on Micro Electro Mechanical Systems (MEMS)*, 1 2012, pp. 692–695.

[61] R. Truell, C. Elbaum, and B. B. Chick, *Ultrasonic methods in solid state physics*. Academic press, 2013.

[62] D. Smoczyński, K. Czuba, E. Papis-Polakowska, P. Kozłowski, J. Ratajczak, I. Sankowska, and A. Jasik, "The impact of mesa etching method on IR photodetector current-voltage characteristics," *Materials Science in Semiconductor Processing*, vol. 118, 2020.

[63] H. Mansoorzare, S. Moradian, S. Shahraini, R. Abdolvand, and J. Gonzales, "Achieving the Intrinsic Limit of Quality Factor in VHF Extensional-Mode Block Resonators," *IFCS 2018 - IEEE International Frequency Control Symposium*, pp. 1–4, 2018.

[64] C. M. Lin, V. Yantchev, J. Zou, Y. Y. Chen, and A. P. Pisano, "Micromachined one-port aluminum nitride lamb wave resonators utilizing the lowest-order symmetric mode," *Journal of Microelectromechanical Systems*, vol. 23, no. 1, pp. 78–91, 2014.

[65] S. I. Jung, C. Ryu, G. Piazza, and H. J. Kim, "A study on the effects of bottom electrode designs on aluminum nitride contour-mode resonators," *Micromachines*, vol. 10, no. 11, pp. 1–11, 2019.

[66] S. Gong, N. K. Kuo, and G. Piazza, "A 1.75 GHz piezoelectrically-transduced SiC lateral overmoded bulk acoustic-wave resonator," *2011 16th International Solid-State Sensors, Actuators and Microsystems Conference, TRANSDUCERS'11*, pp. 922–925, 2011.

[67] M. P. Robinson and J. Clegg, "Improved determination of Q-factor and resonant frequency by a quadratic curve-fitting method," *IEEE Transactions on Electromagnetic Compatibility*, vol. 47, no. 2, pp. 399–402, 5 2005.

[68] A. Kourani, R. Lu, and S. Gong, "A Wideband Oscillator Exploiting Multiple Resonances in Lithium Niobate MEMS Resonator," *IEEE Transactions on Ultrasonics, Ferroelectrics, and Frequency Control*, vol. 67, no. 9, pp. 1854–1866, 2020.

[69] S. Zhang, R. Lu, H. Zhou, S. Link, Y. Yang, Z. Li, K. Huang, X. Ou, and S. Gong, "Surface Acoustic Wave Devices Using Lithium Niobate on Silicon Carbide," *IEEE Transactions on Microwave Theory and Techniques*, vol. 68, no. 9, pp. 3653–3666, 2020.

[70] I. Lekavicius, T. Oo, and H. Wang, "Diamond Lamb wave spin-mechanical resonators with optically coherent nitrogen vacancy centers," *Journal of Applied Physics*, vol. 126, no. 21, 2019.

[71] A. B. STANBRIDGE and D. J. EWINS, "MODAL TESTING USING A SCANNING LASER DOPPLER VIBROMETER," *Mechanical Systems and Signal Processing*, vol. 13, no. 2, pp. 255–270, 1999. [Online]. Available: https://www.sciencedirect.com/science/article/pii/S0888327098912092

[72] T. Saito, O. Matsuda, M. Tomoda, and O. B. Wright, "Imaging gigahertz surface acoustic waves through the photoelastic effect," *J. Opt. Soc. Am. B*, vol. 27, no. 12, pp. 2632–2638, 12 2010. [Online]. Available: http://opg.optica.org/josab/abstract.cfm?URI=josab-27-12-2632

[73] X.-Q. Zheng, J. Lee, and P. X.-L. Feng, "Hexagonal boron nitride nanomechanical resonators with spatially visualized motion," *Microsystems & Nanoengineering*, vol. 3, no. 1, p. 17038, 2017. [Online]. Available: https://doi.org/10.1038/micronano.2017.38

[74] C.-M. Lin, Y.-Y. Chen, V. V. Felmetsger, D. G. Senesky, and A. P. Pisano, "Acoustic characteristics of the third-order quasi-symmetric Lamb wave mode in an AlN/3C-SiC plate," in *2013 IEEE International Ultrasonics Symposium (IUS)*, 2013, pp. 1093–1096.

[75] B. Jiang, N. P. Opondo, and S. A. Bhave, "Semi-insulating 4h-sic lateral bulk acoustic wave resonators," *Applied Physics Letters*, vol. 118, p. 114002, Mar 2021.

[76] N.-K. Kuo, S. Gong, J. Hartman, J. Kelliher, W. Miller, J. Parke, S. V. Krishaswamy, J. D. Adam, and G. Piazza, "Micromachined sapphire GHz lateral overtone bulk acoustic resonators transduced by aluminum nitride," in *2012 IEEE 25th International Conference on Micro Electro Mechanical Systems (MEMS)*, 2012, pp. 27–30.

[77] O. Soykal and T. L. Reinecke, "Quantum metrology with a single spin- 32 defect in silicon carbide," *Physical Review B*, vol. 95, no. 8, pp. 1–5, 2017.

[78] S. G. Carter, O. Soykal, P. Dev, S. E. Economou, and E. R. Glaser, "Spin coherence and echo modulation of the silicon vacancy in $4H\ensuremath{-}\mathrm{SiC}$

at room temperature," *Phys. Rev. B*, vol. 92, no. 16, p. 161202, 10 2015. [Online]. Available: https://link.aps.org/doi/10.1103/PhysRevB.92.161202

[79] A. Hernández-Mínguez, A. V. Poshakinskiy, M. Hollenbach, P. V. Santos, and G. V. Astakhov, "Anisotropic Spin-Acoustic Resonance in Silicon Carbide at Room Temperature," vol. 1, no. d, 2020. [Online]. Available: http://arxiv.org/abs/2005.00787

[80] R. N. Lanning, M. A. Harris, D. W. Oesch, M. D. Oliker, and M. T. Gruneisen, "Quantum Communication over Atmospheric Channels: A Framework for Optimizing Wavelength and Filtering," *Phys. Rev. Applied*, vol. 16, no. 4, p. 44027, 10 2021. [Online]. Available: https://link.aps.org/doi/10.1103/PhysRevApplied.16.044027

[81] N. B. Lingaraju, H.-H. Lu, S. Seshadri, D. E. Leaird, A. M. Weiner, and J. M. Lukens, "Adaptive bandwidth management for entanglement distribution in quantum networks," *Optica*, vol. 8, no. 3, pp. 329–332, 3 2021. [Online]. Available: http://opg.optica.org/optica/abstract.cfm?URI=optica-8-3-329

[82] S. Maity, L. Shao, S. Bogdanović, S. Meesala, Y.-I. Sohn, N. Sinclair, B. Pingault, M. Chalupnik, C. Chia, L. Zheng, K. Lai, and M. Lončar, "Coherent Acoustic Control of a Single Silicon Vacancy Spin in Diamond," pp. 2–7, 2019. [Online]. Available: http://arxiv.org/abs/1910.09710

[83] H. J. Mamin, M. Kim, M. H. Sherwood, C. T. Rettner, K. Ohno, D. D. Awschalom, and D. Rugar, "Nanoscale Nuclear Magnetic Resonance with a Nitrogen-Vacancy Spin Sensor," *Science*, vol. 339, no. 6119, pp. 557–560, 2013. [Online]. Available: https://science.sciencemag.org/content/339/6119/557

[84] Y. Romach, C. Müller, T. Unden, L. J. Rogers, T. Isoda, K. M. Itoh, M. Markham, A. Stacey, J. Meijer, S. Pezzagna, B. Naydenov, L. P. McGuinness, N. Bar-Gill, and F. Jelezko, "Spectroscopy of Surface-Induced Noise Using Shallow Spins in Diamond," *Phys. Rev. Lett.*, vol. 114, no. 1, p. 17601, 1 2015. [Online]. Available: https://link.aps.org/doi/10.1103/PhysRevLett.114.017601

[85] M. Kim, H. J. Mamin, M. H. Sherwood, K. Ohno, D. D. Awschalom, and D. Rugar, "Decoherence of Near-Surface Nitrogen-Vacancy Centers Due to Electric Field Noise," *Phys. Rev. Lett.*, vol. 115, no. 8, p. 87602, 8 2015. [Online]. Available: https://link.aps.org/doi/10.1103/PhysRevLett.115.087602

[86] B. A. Myers, A. Das, M. C. Dartiailh, K. Ohno, D. D. Awschalom, and A. C. Bleszynski Jayich, "Probing Surface Noise with Depth-Calibrated Spins in Diamond," *Phys. Rev. Lett.*, vol. 113, no. 2, p. 27602, 7 2014. [Online]. Available: https://link.aps.org/doi/10.1103/PhysRevLett.113.027602

[87] S. Kawai, H. Yamano, T. Sonoda, K. Kato, J. J. Buendia, T. Kageura, R. Fukuda, T. Okada, T. Tanii, T. Higuchi, M. Haruyama, K. Yamada, S. Onoda, T. Ohshima, W. Kada, O. Hanaizumi, A. Stacey, T. Teraji, S. Kono, J. Isoya, and H. Kawarada, "Nitrogen-Terminated Diamond Surface for Nanoscale NMR by Shallow Nitrogen-Vacancy Centers," *The Journal of Physical Chemistry C*, vol. 123, no. 6, pp. 3594–3604, 2 2019. [Online]. Available: https://doi.org/10.1021/acs.jpcc.8b11274

[88] D. Bluvstein, Z. Zhang, C. A. McLellan, N. R. Williams, and A. C. Jayich, "Extending the Quantum Coherence of a Near-Surface Qubit by Coherently Driving the Paramagnetic Surface Environment," *Physical Review Letters*, vol. 123, no. 14, 2019.

[89] I. Mohacsi, I. Vartiainen, B. Rösner, M. Guizar-Sicairos, V. A. Guzenko, I. McNulty, R. Winarski, M. V. Holt, and C. David, "Interlaced zone plate optics for hard X-ray imaging in the 10 nm range," *Scientific Reports*, vol. 7, no. 1, p. 43624, 2017. [Online]. Available: https://doi.org/10.1038/srep43624

[90] J. C. Wiltse and J. E. Garrett, "The Fresnel zone plate antenna," *Microwave journal*, vol. 34, no. 1, pp. 101–110, 1991.

[91] A. Ravi, J. Kuo, and A. Lal, "CMOS compatible GHz ultrasonic Fresnel microfluidic actuator," *2018 Solid-State Sensors, Actuators and Microsystems Workshop, Hilton Head 2018*, pp. 310–313, 2018.

[92] D. Tarrazó-Serrano, S. Pérez-López, P. Candelas, A. Uris, and C. Rubio, "Acoustic Focusing Enhancement In Fresnel Zone Plate Lenses," *Scientific Reports*, vol. 9, no. 1, p. 7067, 2019. [Online]. Available: https://doi.org/10.1038/s41598-019-43495-x

[93] J. Rodriguez, S. A. Chandorkar, C. A. Watson, G. M. Glaze, C. H. Ahn, E. J. Ng, Y. Yang, and T. W. Kenny, "Direct Detection of Akhiezer Damping in a Silicon MEMS Resonator," *Scientific Reports*, vol. 9, no. 1, pp. 1–10, 2019. [Online]. Available: http://dx.doi.org/10.1038/s41598-019-38847-6

[94] B. W. An, S. Heo, S. Ji, F. Bien, and J.-U. Park, "Transparent and flexible fingerprint sensor array with multiplexed detection of tactile pressure and skin temperature," *Nature communications*, vol. 9, no. 1, pp. 1–10, 2018.

[95] P. H. Dykstra, V. Roy, C. Byrd, W. E. Bentley, and R. Ghodssi, "Microfluidic electrochemical sensor array for characterizing protein interactions with various functionalized surfaces," *Analytical chemistry*, vol. 83, no. 15, pp. 5920–5927, 2011.

[96] M. Radtke, E. Bernardi, A. Slablab, R. Nelz, and E. Neu, "Nanoscale sensing based on nitrogen vacancy centers in single crystal diamond and nanodiamonds: achievements and challenges," *Nano Futures*, vol. 3, no. 4, p. 42004, 12 2019. [Online]. Available: https://doi.org/10.1088%2F2399-1984%2Fab5f9b

[97] P. Wang, S. Chen, M. Guo, S. Peng, M. Wang, M. Chen, W. Ma, R. Zhang, J. Su, X. Rong, F. Shi, T. Xu, and J. Du, "Nanoscale magnetic imaging of ferritins in a single cell," *Science Advances*, vol. 5, no. 4, 2019. [Online]. Available: https://advances.sciencemag.org/content/5/4/eaau8038

[98] P.-L. Yu, N. Opondo, S. Dai, B. Jiang, D. T. Morisette, and S. A. Bhave, "Single crystalline 4h-sic membrane resonators," in *2018 IEEE International Frequency Control Symposium (IFCS)*, 2018, pp. 1–5.

[99] B. Jiang, N. Opondo, G. Wolfowicz, P. Yu, D. D. Awschalom, and S. A. Bhave, "SiC Cantilevers for Generating Uniaxial Stress," in *2019 20th International Conference on*

Solid-State Sensors, Actuators and Microsystems Eurosensors XXXIII (TRANSDUCERS EUROSENSORS XXXIII), Jun 2019, pp. 1655–1658.

[100] H. Chen, N. F. Opondo, B. Jiang, E. R. MacQuarrie, R. S. Daveau, S. A. Bhave, and G. D. Fuchs, "Engineering electron–phonon coupling of quantum defects to a semiconfocal acoustic resonator," *Nano Letters*, vol. 19, no. 10, pp. 7021–7027, 2019.

A. STANDARD FABRICATION PROCESS FOR ALN-SIC LOBAR DEVICES

This appendix documents the detailed fabrication process of AlN-SiC LOBAR devices. Each major step is written in a section.

The fabrication starts after retrieving the 200 um SiC wafer deposited with Mo-AlN-Mo stack. Before any fabrication steps, the wafer thickness should be measured with a micrometer. Because of the error in the thinning process, the wafer might have a thickness difference up to 30 um from the designed 200 um, and might have thickness variation across it. To know how deep the backside etching should be, it is cruicial to get the starting thickness of the wafer.

Note the lithography recipes below are just for reference. The cleanroom condition is subject to constant change, and the recipe should be tested and modified if necessary.

The SiC wafer and chips are bonded to carrier wafer with crystalbond, which can be cleaned with hot water bath at 70 ℃.

A.1 Backside Nickel Hardmask

1. Wafer solvent cleaning
   (a) Toluene soak, 5 min
   (b) Acetone soak, 5 min
   (c) Isopropyl alcohol soak, 5 min
2. Electroplating seeding layer deposition
   (a) Equipment: Any evaporator
   (b) Metal: 10 nm Ti and 50 nm Cr
3. Lithography
   (a) Photoresist: AZ 9260
   (b) Spinning: 4000 rpm for 30 seconds

(c) Softbaking: 110 ℃for 3 minutes

(d) Exposure: Heidelberg Maskless Aligner with 415 mJ/cm^2 dose

(e) Development: Microposit developer undiluted for 2 minutes or until clear

(f) Hardbake: 90 ℃for 15 minutes or longer

(g) Ashing: Ar at 200 sccm with 100 W power for 1 minutes

4. Nickel plating

(a) Prepare nickel sulfamate solution and set bath at 40 ℃. The solution has to be clean, or the deposition quality will be negatively affected.

(b) Use Keithley 6221 AC/DC source set at 10 mA/cm^2

(c) Time: since the nickel sulfamate solution is variable over time, the electroplating time should refer to the log book kept with the deposition setup. At the time of this thesis being written, 50 minutes of deposition yield for about 4 um of Ni.

(d) Soak the wafer in Acetone overnight to remove the AZ9260. Note PRS2000 should not be used since it will etch metals including Mo.

A.2 Frontside Transducer Definition

1. Top Mo layer etching

(a) Photoresist: SPR 4.5 3000 rpm for 30 seconds

(b) Softbaking: 115℃for 90 seconds

(c) Exposure Heidelberg 200 mJ/cm^2 dose

(d) Development Microposit : water = 1:1 2 minutes

(e) Dry Etch: Plasma-Therm APEX SLR, with recipe name "Alex-Mo" for 1 minute, or until the Mo layer is fully removed, when the purple colored AlN layer can be seen.

(f) Strip the resist with Acetone

2. AlN Etching

(a) Photoresist: AZ 9260, the lithography is identical to Ni hardmask section, without using the hardbaking

(b) Dry Etch AlN: Plasma-Therm APEX SLR, with recipe name "Alex-AlN" for 10 minutes, or until the AlN layer is fully removed, when the silver colored bottom Mo layer can be seen. The Mo layer can also be determined by using a multimeter's diode test mode on the surface, as Mo is highly conductive while AlN is resistive. Note that the etch rate is highly variable due to AlN quality changes and chamber condition, so it is suggested to try smaller time intervals at this step and monitor the surface closely.

(c) Dry Etch bottom Mo: Plasma-Therm APEX SLR, with recipe name "Alex-Mo" for 1 minute, or until end surface is no longer conductive when tested with the multimeter.

(d) Strip the resist with Acetone.

3. Bottom Electrode Exposure with Wet Etch

(a) Photoresist: AZ 1518

(b) Spinning: 4000 rpm for 30 seconds

(c) Softbaking: 110 ℃for 1 minutes

(d) Exposure: Heidelberg Maskless Aligner with 315 mJ/cm^2 dose

(e) Development: Microposit : water = 1 : 1 for 2 minutes or until clear

(f) Hardbake: 145 ℃for 5 minutes or longer

(g) Wet etch: H_3PO_4 provided in the cleanroom, undiluted. Pre-heat the solution to 130 ℃. Dip the wafer in the acid in 10 second intervals and observe. Etch until the shinning bottom Mo is exposed in the bottom electrode region.

(h) Strip the resist with Acetone.

A.3 Frontside Hardmask and SiC Etching

1. Top ITO hardmask

(a) Deposition: Lesker Evaporator

(b) Metal: 10 nm Ti and 600 nm ITO

(c) Photoresist: SPR 7.0, 4000 rpm spinning for 30 seconds

(d) Exposure Heidelberg 580 mJ/cm^2 dose

(e) Development Microposit : water = 1:1 2 minutes or until clear

(f) Dry Etch: Plasma-Therm APEX SLR, with recipe name "Alex-ITO" for 5 minute, or until the ITO is fully removed. It is ok to over-etch in this step, as the SiC underneath will be removed later.

(g) Strip the resist with Acetone

2. Frontside SiC Etching

(a) **Warning** Due to unstable equipment conditions, the etch rate of SiC and etch quality should be tested everytime before the real sample going under etch.

(b) Etcher: STS AOE or Panasonic

(c) Dry Etch: Use the Alex-SiC recipe in STS AOE. the etch rate is roughly 20-30 um per hour. Etch for at least 10 um. It is recommended to etch till 15 um for a cleaner release. The ITO should be closely monitored to avoid depletion.

3. Backside SiC Etching

(a) Etcher: Plasma-therm or Panasonic

(b) Dry Etch: Use the Cr etching recipe in Plasma-therm or Panasonic to remove the Cr seeding layer for electroplating. The etch time should be tested, but at around 5 minutes.

(c) Etcher: STS AOE

(d) Dry Etch: Use the Alex-SiC recipe in STS AOE. the etch rate is roughly 20-30 um per hour. Etch for about 120 um. At this point the wafer can be broken into smaller square chips for easier handling. Due to the etch rate difference in the center and the edge of the wafer, it is needed to release the chips separately.

(e) Based on the wafer thickness, further etch the chips to release the device. Measure the device thickness with optical profilometer or contact profilometer to make sure the end thickness is correct.

4. ITO removal: quickly dip the chip into HCl_3:H_2O = 1:5 solution until the ITO is clear, followed by a dipping into Buffered Oxide Etch undiluted to remove the Ti

B. CODING FOR LAYOUT GENERATION AND DATA ANALYSIS

B.1 Layout Generation

```
# -*- coding: utf-8 -*-
"""
Created on Wed Apr 29 18:35:17 2020

This is the code for generating individual LOBARs and a final layout using
    ↪ GDSPY

@author: jiang561
"""
import gdspy as gp
import numpy as np
import string



def update_xy(x=5000, y=3500, y_max=0):
    r=50000
    while y>y_max:
        x=x+3000
        if x>46500:
            break
        y_max = np.sqrt(r**2-x**2)-3500
        y=3500
    return x, y, y_max

#fuction to create single LOBAR instance. Width is the multiple of
    ↪ wavelength,
```

```
#hbar determines whether to add an etch to remove HBAR mode
#shallow_ref: add full depth reflector or not
#ground: grounded or floating bottom electrode
#c_ref: center of the reflector
#r_ref: radius of reflector by wl multiple, r=0 means no reflector
#layers: 0 - top electrode; 1- AlN; 2-bottom electrode ; 3 - backside;4 -
    ↪ frontside; 5 - quarter frame
def lobar(lib=None,r_ref = 0, width = 2, hbar = True,shallow_ref = False,
    ↪ ground = True, c_ref = 240):
    gp.current_library = gp.GdsLibrary()
    wl = 40 #wavelength
    a_pad = 100 #electrode pad size
    d_pad = 150 #electrode distance
    w = 1980 #width of backside window
    h = 480 #height of backside window
    h_lobar = 300 #height of LOBAR
    w_tether = 25 #width of tether
    h_tether = (h-h_lobar)/2 #height of lobar

    cellname = "L%d_W%d_R%.2f" %(width*wl, h_lobar, r_ref)#cell name should
        ↪ be variable depending on the parameters

    #determine the cellname
    if hbar:
        cellname += "_NoHBAR"
    else:
        cellname += "_HBAR"
    if ground:
        cellname += "_Ground"
    else:
```

```
    cellname += "_Float"
if shallow_ref:
    cellname += "_Shallow"

# p = gp.Cell(cellname) #create the cell to be returned
p = lib.new_cell(cellname, overwrite_duplicate=True)
# p = gp.Cell()

#--------------------layer 0 top electrodes----------------
if r_ref ==0:
    sp1 = gp.FlexPath([(0, 385), (0, 142)], 10, layer =0)
    sp2 = gp.FlexPath([(0, -385), (0, -142)], 10, layer =0)
    e1 = gp.Rectangle((-50,382.5), (50,482.5), layer=0)
    e2 = gp.Rectangle((50,-382.5), (-50,-482.5), layer=0)
else:
    sp1 = gp.FlexPath([(0,145), (0,249.5),(370,249.5),(370,365)], 10,
       ↪ layer=0)
    sp2 = gp.FlexPath([(0,-145), (0,-249.5),(370,-249.5),(370,-365)], 10,
       ↪  layer=0)
    e1 = gp.Rectangle((320,365), (420,465), layer=0)
    e2 = gp.Rectangle((320,-465), (420,-365), layer=0)
mid1 = gp.Rectangle((-36,135),(36,145), layer=0)
mid2 = gp.Rectangle((-36,-145),(36,-135), layer=0)
mid3 = gp.Rectangle((5,138),(15,-132), layer=0)
mid4 = gp.Rectangle((-15,-136.25), (-5,132),layer=0)
mid5 = gp.Rectangle((-35,-132),(-25,138.75), layer=0)
mid6 = gp.Rectangle((25,-136.25),(35,132),layer=0)

p.add([sp1,sp2,e1,e2,mid1,mid2,mid3,mid4,mid5,mid6])
```

```
#----------------layer 1 AlN---------------
mid = gp.Rectangle((-38,-147.5),(38,147.5), layer=1)
if r_ref==0:
    pad_up1=gp.Rectangle((-210,372.5),(-90,492.5), layer=1)
    pad_up2=gp.copy(pad_up1,150,0)
    pad_up3=gp.copy(pad_up2,150,0)
    pad_down1 = gp.Rectangle((-210,-492.5),(-90,-372.5), layer=1)
    pad_down2=gp.copy(pad_down1,150,0)
    pad_down3=gp.copy(pad_down2,150,0)
    up_trace_mid = gp.FlexPath([(0,380),(0,140)],15, layer=1)
    down_trace_mid = gp.FlexPath([(0,-380),(0,-140)],15, layer=1)
    if ground:
        up_trace_side = gp.FlexPath([(-150,380),(-150,270),(150,270)
            ↪ ,(150,380)],15,layer=1)
        down_trace_side = gp.FlexPath([(-150,-380),(-150,-270),(150,-270)
            ↪ ,(150,-380)],15,layer=1)
        p.add([up_trace_side, down_trace_side])
else:
    pad_up1=gp.Rectangle((160,355),(280,475), layer=1)
    pad_up2=gp.copy(pad_up1,150,0)
    pad_up3=gp.copy(pad_up2,150,0)
    pad_down1 = gp.Rectangle((160,-355),(280,-475), layer=1)
    pad_down2=gp.copy(pad_down1,150,0)
    pad_down3=gp.copy(pad_down2,150,0)
    up_trace_mid = gp.FlexPath([(370,360),(370,250),(0,250),(0,140)],15,
        ↪ layer=1)
    down_trace_mid = gp.FlexPath([(370,-360),(370,-250),(0,-250),(0,-140)
        ↪ ],15, layer=1)
    if ground:
```

```
        up_trace_side = gp.FlexPath([(520,360),(520,250),(220,250)
            ↪ ,(220,360)],15,layer=1)
        down_trace_side = gp.FlexPath([(520,-360),(520,-250),(220,-250)
            ↪ ,(220,-360)],15,layer=1)
        p.add([up_trace_side, down_trace_side])

textname = "L%d W%d R%.2f" %(width*wl, h_lobar, r_ref)#cell name should
    ↪ be variable depending on the parameters

#determine the cellname
if hbar:
    textname += "\nNoHBAR"
else:
    textname += "\nHBAR"
if ground:
    textname += " Ground"
else:
    textname += " Float"
if shallow_ref:
    textname += " Shallow"
textlab = gp.Text(textname, 100,(-600,-700),layer=1)
p.add([mid,pad_up1,pad_up2,pad_up3,pad_down1,pad_down2,pad_down3,
    ↪ up_trace_mid, down_trace_mid, textlab])


#------------------layer 2 bottom electrode------------
if r_ref==0:
    up1=gp.Rectangle((-200,382.5),(-100,482.5), layer=2)
    up2 = gp.copy(up1,300,0)
    down1=gp.Rectangle((-200,-382.5),(-100,-482.5), layer=2)
```

```
    down2 = gp.copy(down1,300,0)
else:
    up1 = gp.Rectangle((170,365),(270,465),layer=2)
    up2 = gp.copy(up1,300)
    down1 = gp.Rectangle((170,-365),(270,-465), layer=2)
    down2 = gp.copy(down1,300,0)
p.add([up1,up2,down1,down2])

#------------------layer 3 backside------------------
mid = gp.Rectangle((-990,-240),(990,240), layer=3)
if hbar:
    if r_ref !=0:
        hbar_up = gp.Rectangle((320,365),(420,465), layer=3)
        hbar_down = gp.Rectangle((320,-365),(420,-465), layer=3)
    else:
        hbar_up = gp.Rectangle((-50,382.5),(50,482.5), layer=3)
        hbar_down = gp.Rectangle((-50,-482.5),(50,-382.5), layer=3)
    p.add([hbar_up,hbar_down])

if (r_ref != 0) and (not shallow_ref):
    if r_ref < 3.5:
        ref_up = gp.Round((0,240), r_ref*wl+50, inner_radius=r_ref*wl,
            ↪ initial_angle=20*np.pi/180, final_angle=160*np.pi/180,
            ↪ layer=3)
        ref_down = gp.copy(ref_up).mirror((-1,0),(1,0))
    else:
        ref_up = gp.Round((0,150), r_ref*wl+50, inner_radius=r_ref*wl,
            ↪ initial_angle=40*np.pi/180, final_angle=140*np.pi/180,
            ↪ layer=3)
        ref_down = gp.copy(ref_up).mirror((-1,0),(1,0))
```

```
        p.add([ref_up,ref_down])
    p.add(mid)



    #---------------------layer 4 front side------------
    box = gp.Rectangle((-990,-240),(990,240), layer=4)
    a=width/2*wl
    mid = gp.Rectangle((a,150), (-a,-150), layer=4)
    up_te = gp.FlexPath([(0,240),(0,150)],25, layer=4)
    down_te = gp.FlexPath([(0,-240),(0,-150)],25, layer=4)
    rel = gp.boolean(box, mid, 'not', layer=4)
    rel = gp.boolean(rel, up_te, 'not', layer=4)
    rel = gp.boolean(rel, down_te, 'not', layer=4)
    p.add(rel)
    if r_ref != 0:
        if r_ref < 3.5:
            ref_up = gp.Round((0,240), r_ref*wl+50, inner_radius=r_ref*wl,
                ↪ initial_angle=20*np.pi/180, final_angle=160*np.pi/180,
                ↪ layer=4)
            ref_down = gp.copy(ref_up).mirror((-1,0),(1,0))
        else:
            ref_up = gp.Round((0,150), r_ref*wl+50, inner_radius=r_ref*wl,
                ↪ initial_angle=40*np.pi/180, final_angle=140*np.pi/180,
                ↪ layer=4)
            ref_down = gp.copy(ref_up).mirror((-1,0),(1,0))
        p.add([ref_up,ref_down])

    return p, lib

def quarter_lay(r=50000):
```

```
gp.current_library = gp.GdsLibrary()
lib = gp.GdsLibrary(name = 'LOBAR_V21')
#LOBAR variables
width = np.array([2, 40])
r_inner = np.arange(4.5, 5.25, 0.25)
r_outer = np.arange(1.5,2.75,0.25)
c_inner = 150
c_outer = 240
hbar = [True, False]
shallow_ref = [True, False]
ground = [True, False]

#quarter wafer parameters
r=50000;
x=5000;
y_max = np.sqrt(r**2-x**2)-3500;
y=3500;
#max_ins = 336 #pre-calculated max number of instances
num_ins = 0
quarter = lib.new_cell("quarter_layout",overwrite_duplicate=True)
quarter_shape = gp.Round((0,0), 50000, initial_angle=0, final_angle=np.
   ↪ pi/2, layer=5)
quarter.add(quarter_shape)

str_char = string.ascii_uppercase

for i in range(0,100):
    #HBAR craete the reference list
    for w in width:
        for h in hbar:
```

```
        x, y, y_max = update_xy(x, y, y_max)
        if x>46500:

            return lib
        p, lib = lobar(lib,0,w,h)
        ref = gp.CellReference(p, (x,y))
        x_co = (x-5000)//3000
        y_co = (y-3500)//1500
        coordinate_label = str_char[x_co] + "%d" % (y_co+1)
        textlab = gp.Text(coordinate_label, 150,(x-1000,y-750),layer
            ↪ =1)
        quarter.add(textlab)
        quarter.add(ref)

        y+=1500
        num_ins += 1
#shallow reflector
for w in width:
    for s in shallow_ref:
        x, y, y_max = update_xy(x, y, y_max)
        if x>46500:

            return lib
        p, lib = lobar(lib,4.5, w, True, s, True, c_inner)
        ref = gp.CellReference(p, (x,y))
        x_co = (x-5000)//3000
        y_co = (y-3500)//1500
        coordinate_label = str_char[x_co] + "%d" % (y_co+1)
        textlab = gp.Text(coordinate_label, 150,(x-1000,y-750),layer
            ↪ =1)
```

```
        quarter.add(textlab)
        # ref = gp.CellReference(lobar(4.5, w, True, s, True,
            ↪ c_inner), (x,y))
        quarter.add(ref)

        y+=1500
        num_ins += 1
        #inner vs outer reflector
        x, y, y_max = update_xy(x, y, y_max)
        if x>46500:

            return lib
        p, lib = lobar(lib, 1.5, w, True, s, True, c_outer)
        ref = gp.CellReference(p, (x,y))
        x_co = (x-5000)//3000
        y_co = (y-3500)//1500
        coordinate_label = str_char[x_co] + "%d" % (y_co+1)
        textlab = gp.Text(coordinate_label, 150,(x-1000,y-750),layer
            ↪ =1)
        quarter.add(textlab)
        # ref = gp.CellReference(lobar(1.5, w, True, s, True,
            ↪ c_outer), (x,y))
        quarter.add(ref)

        y+=1500
        num_ins += 1
#grounded bottom
for w in width:
    for g in ground:
        x, y, y_max = update_xy(x, y, y_max)
```

```
        if x>46500:

            return lib
        p, lib = lobar(lib, 0, w, True, False, g)
        ref = gp.CellReference(p, (x,y))
        x_co = (x-5000)//3000
        y_co = (y-3500)//1500
        coordinate_label = str_char[x_co] + "%d" % (y_co+1)
        textlab = gp.Text(coordinate_label, 150,(x-1000,y-750),layer
            ↪ =1)
        quarter.add(textlab)
        # ref = gp.CellReference(lobar(0, w, True, False, g), (x,y))
        quarter.add(ref)

        y+=1500
        num_ins += 1
#distance of reflector
for w in width:
    for r_in in r_inner:
        x, y, y_max = update_xy(x, y, y_max)
        if x>46500:

            return lib
        p, lib = lobar(lib, r_in, w, True, False, True, c_inner)
        ref = gp.CellReference(p, (x,y))
        x_co = (x-5000)//3000
        y_co = (y-3500)//1500
        coordinate_label = str_char[x_co] + "%d" % (y_co+1)
        textlab = gp.Text(coordinate_label, 150,(x-1000,y-750),layer
            ↪ =1)
```

```
            quarter.add(textlab)
            # ref = gp.CellReference(lobar(r_in, w, True, False, True,
                ↪ c_inner), (x,y))
            quarter.add(ref)

            y+=1500
            num_ins += 1
        for r_out in r_outer:
            x, y, y_max = update_xy(x, y, y_max)
            if x>46500:

                return lib
            p, lib = lobar(lib, r_out, w, True, False, True, c_outer)
            ref = gp.CellReference(p, (x,y))
            x_co = (x-5000)//3000
            y_co = (y-3500)//1500
            coordinate_label = str_char[x_co] + "%d" % (y_co+1)
            textlab = gp.Text(coordinate_label, 150,(x-1000,y-750),layer
                ↪ =1)
            quarter.add(textlab)
            # ref = gp.CellReference(lobar(r_out, w, True, False, True,
                ↪ c_outer), (x,y))
            quarter.add(ref)

            y+=1500
            num_ins += 1

    return lib

if __name__ == "__main__":
```

```
    # gp.current_library = gp.GdsLibrary()
    lib = quarter_lay()

    # quarter = quarter_lay()
    #
    lib.write_gds('first.gds')
```

B.2 Transmission Measurement Plotting

```
import cvxpy as cp
import numpy as np
import skrf as rf
import scipy as sp
import matplotlib.pyplot as plt
import math
import string
import os.path



def Y_in(Y11, Y12, Y21, Y22, YL = 1/50): #calculate the input admittance
    ↪ based on a 2 port network
    return (Y11 - (Y12*Y21)/(Y22+YL))


A = string.ascii_uppercase
A_list = list(A)
A_list = A_list[0:14]
A_mat = np.array(A_list, dtype = object)
B_mat = np.zeros([24],dtype = object)
for i in range(1,25):
    B_mat[i-1] = str(i)
```

```
name_list = []
for x in A_mat:
    for y in B_mat:
        n = x+y
        name_list.append(n)


# i=0
for n in name_list:
    s2p_name = '20200930 2nd batch SiC LOBAR/' + n + '.s2p'
    if os.path.exists(s2p_name):
        device = rf.Network(s2p_name)
        # S = device.s_db
        S = device.s
        # Y_input = Y_in(Y[:,0,0], Y[:,0,1], Y[:,1,0], Y[:,1,1])
        freq = device.f
        fig1 = plt.figure()
        ax = fig1.add_subplot(1,1,1)
        ax.set_xlabel('Frequency (Hz)',fontsize=14)
        ax.set_ylabel('S21',fontsize=14)
        ax.set_title(n, fontsize=24)
        ax.plot(freq, abs(S[:,1,0]), linewidth =1.5)
        # plt.plot(freq, abs(S[:,0,0]))
        # plt.yscale('log')
        # ax.set_yscale('log')
        fig_name = 'S21_plot/' + n + '.png'
        fig1.savefig(fig_name)
        plt.close(fig1)
        i+=1
for n in name_list:
    s2p_name = '20200930 2nd batch SiC LOBAR/' + n + '.s2p'
```

```
    if os.path.exists(s2p_name):
        device = rf.Network(s2p_name)
        savename = 'csv_data/'+ n +'.csv'
        rf.io.general.network_2_spreadsheet(device, savename, 'csv', 'ma')
for n in name_list:
    s2p_name = '20200930 2nd batch SiC LOBAR/' + n + '.s2p'
    if os.path.exists(s2p_name):
        device = rf.Network(s2p_name)
        S = device.s_db
        # S = device.s
        # Y_input = Y_in(Y[:,0,0], Y[:,0,1], Y[:,1,0], Y[:,1,1])
        freq = device.f
        fig1 = plt.figure()
        ax = fig1.add_subplot(1,1,1)
        ax.set_xlabel('Frequency (Hz)',fontsize=14)
        ax.set_ylabel('S21 (dB)',fontsize=14)
        ax.set_title(n, fontsize=24)
        ax.plot(freq, S[:,1,0], linewidth =1.5)
        # plt.plot(freq, abs(S[:,0,0]))
        # plt.yscale('log')
        # ax.set_yscale('log')
        fig_name = 'S21_plot/' + n + '_dB.png'
        fig1.savefig(fig_name)
        plt.close(fig1)


#csv input impedance
for n in name_list:
    s2p_name = '20200930 2nd batch SiC LOBAR/' + n + '.s2p'
    if os.path.exists(s2p_name):
        device = rf.Network(s2p_name)
```

```
        Y = device.y
        freq = device.f
        Y_input = Y_in(Y[:,0,0], Y[:,0,1], Y[:,1,0], Y[:,1,1])
        data = np.stack((freq, Y_input), axis=1)
        savename = 'input_admittance/'+n+'.csv'
        np.savetxt(savename, data, delimiter=',', header='frequency(Hz),
            ↪ input admittance(S)')
```

B.3 Integration of COMSOL data for ODSAR X-scan

```
# -*- coding: utf-8 -*-
"""
Created on Fri Mar 25 21:51:23 2022

@author: jiang561
"""

import numpy as np
import matplotlib.pyplot as plt
from scipy.signal import savgol_filter

def cal_linear_integral(data, mesh_density):
    gap = max(data1[:,0]) *2 / mesh_density
    start = min(data[:,0]) - gap/2
    integ = np.zeros([mesh_density+1,2])
    j=0
    for i in np.arange(start, -start, gap):
        use_data = data[np.where((data[:,0]<i+gap) & (data[:,0]>=i))]
        integ[j,0] = i+gap/2
        integ[j,1] = sum(use_data[:,2])
```

```
        j+=1
    return integ

if __name__ == "__main__":
    plt.close('all')
    data1 = np.loadtxt('strain_85o7.csv', skiprows=8, delimiter=',')
    data2 = np.loadtxt('strain_112o45.csv', skiprows=8, delimiter=',')
    mesh = 500



    thickness = 10 # SiC thickness, used to filter y data

    #only keep data in the SiC region
    w1 = np.where(data1[:,1]<=thickness/2)
    w2 = np.where(data2[:,1]<=thickness/2)
    d1 = data1[w1]
    d2 = data2[w2]

    line1 = cal_linear_integral(d1, mesh)
    line2 = cal_linear_integral(d2, mesh)
    np.savetxt('COMSOL_integral_x_89o5MHz.csv', line1, header='x (um)
        ↪ strain integral')
    np.savetxt('COMSOL_integral_x_112o45MHz.csv', line1, header='x (um)
        ↪ strain integral')

    fig1 = plt.figure()
    ax = fig1.add_subplot(1,1,1)
    ax.set_xlabel('x (um)',fontsize=14)
    ax.set_ylabel('Strain integral',fontsize=14)
    ax.set_title("Axial Strain Integral From COMSOL", fontsize=24)
```

```
ax.plot(line1[:,0], line1[:,1], linewidth =1.5, label = '89.5 MHz')
ax.plot(line2[:,0], line2[:,1], linewidth =1.5, label = '116.4 MHz')
ax.legend()
# ax.plot(line2, linewidth =1.5)



dat_spin_1 = np.loadtxt('89p5MHzXSCAN.txt', skiprows=1, delimiter=' ')
# shift = 11.7
# dat_spin_1[:,0]+=shift
# dat_spin_1[:,1] = -dat_spin_1[:,1] # revert the y direction, to fit
   ↪ the simulation.
m = np.mean(dat_spin_1[:,1])
dat_spin_1[:,1] = 2*m-dat_spin_1[:,1]
dat_spin_1[:,1] = savgol_filter(dat_spin_1[:,1],9,5)


fig2 = plt.figure()
ax = fig2.add_subplot(1,1,1)
ax2 = ax.twinx()
ax.set_xlabel('x (um)',fontsize=14)
ax.set_ylabel('Strain integral',fontsize=14)
# ax.set_title("Axial Strain Integral From COMSOL vs spin, 89MHz",
   ↪ fontsize=24)
ax.plot(line1[:,0], line1[:,1], linewidth =1.5, label = 'Strain
   ↪ Simulation', color = 'c')
ax.set_xlim([-120,120])
# ax2.set_xlabel('x (um)',fontsize=14)
ax2.set_ylabel('Spin Constrast (%)',fontsize=14)
ax2.plot(dat_spin_1[:,0], dat_spin_1[:,1], linewidth =1.5, label = 'Spin
   ↪  Measurement', color = 'b')
lines, labels = ax.get_legend_handles_labels()
```

```
lines2, labels2 = ax2.get_legend_handles_labels()
ax2.legend(lines + lines2, labels + labels2, loc=0)




dat_spin_2 = np.loadtxt('113p75MHzXSCAN.txt', skiprows=1, delimiter=' ')
# shift = 11.7
# dat_spin_1[:,0]+=shift
# dat_spin_2[:,1] = -dat_spin_2[:,1] # revert the y direction, to fit
   ↪ the simulation.
m = np.mean(dat_spin_2[:,1])
dat_spin_2[:,1] = 2*m-dat_spin_2[:,1]
dat_spin_2[:,1] = savgol_filter(dat_spin_2[:,1],9,5)

fig3 = plt.figure()
ax = fig3.add_subplot(1,1,1)
ax2 = ax.twinx()
ax.set_xlabel('x (um)',fontsize=14)
ax.set_ylabel('Strain integral',fontsize=14)
# ax.set_title("Axial Strain Integral From COMSOL vs spin, 113MHz",
   ↪ fontsize=24)
ax.plot(line2[:,0], line2[:,1], linewidth =1.5, label = 'Strain
   ↪ Simulation', color = 'c')
ax.set_xlim([-120,120])
# ax2.set_xlabel('x (um)',fontsize=14)
ax2.set_ylabel('Spin Constrast (%)',fontsize=14)
ax2.plot(dat_spin_2[:,0], dat_spin_2[:,1], linewidth =1.5, label = 'Spin
   ↪  Measurement', color = 'b')
lines, labels = ax.get_legend_handles_labels()
```

```
lines2, labels2 = ax2.get_legend_handles_labels()
ax2.legend(lines + lines2, labels + labels2, loc=0)



fig4 = plt.figure()
ax = fig4.add_subplot(1,1,1)
ax.set_xlabel('x (um)',fontsize=14)
ax.set_ylabel('PL contrast (%)',fontsize=14)
# ax.set_title("Axial Strain Integral From COMSOL", fontsize=24)
ax.plot(dat_spin_1[:,0], dat_spin_1[:,1], linewidth =1.5, label = '89.5
    ↪ MHz')
ax.plot(dat_spin_2[:,0], dat_spin_2[:,1], linewidth =1.5, label = '116.4
    ↪  MHz')
ax.legend()
```

VITA

Boyang Jiang was born in Hefei, Anhui Province, China on April 16, 1998. He attended Hefei Shiyan Elementary School, Hefei No.45 Junior High School, and graduated from Hefei No.6 Senior High School in 2013. The following August, he entered University of Science and Technology of China (USTC) and received the Bachelor of Science degree in May 2017 in Physics. Since August 2017, He moved to West Lafayette, Indiana, USA to pursue a Ph.D. degree in the School of Electrical and Computer Engineering at Purdue University. He is expected to graduate in May 2022.

PUBLICATIONS

- P.-L. Yu, N. Opondo, S. Dai, B. Jiang, D. T. Morisette, and S. A. Bhave, "Single crystalline 4h-sic membrane resonators," in *2018 IEEE International Frequency Control Symposium (IFCS)*, 2018, pp. 1–5

- B. Jiang, N. Opondo, G. Wolfowicz, P. Yu, D. D. Awschalom, and S. A. Bhave, "SiC Cantilevers for Generating Uniaxial Stress," in *2019 20th International Conference on Solid-State Sensors, Actuators and Microsystems Eurosensors XXXIII (TRANSDUCERS EUROSENSORS XXXIII)*, Jun 2019, pp. 1655–1658

- H. Chen, N. F. Opondo, B. Jiang, E. R. MacQuarrie, R. S. Daveau, S. A. Bhave, and G. D. Fuchs, "Engineering electron–phonon coupling of quantum defects to a semiconfocal acoustic resonator," *Nano Letters*, vol. 19, no. 10, pp. 7021–7027, 2019

- B. Jiang, N. P. Opondo, and S. A. Bhave, "Semi-insulating 4h-sic lateral bulk acoustic wave resonators," *Applied Physics Letters*, vol. 118, p. 114002, Mar 2021